A&A 476, 807–828 (2007)
DOI: 10.1051/0004-6361:20077225

Astronomy & Astrophysics

A spectral line survey of Orion KL in the bands 486-492 and 541-577 GHz with the Odin⋆ satellite⋆⋆

II. Data analysis

C. M. Persson[1], A. O. H. Olofsson[1,2], N. Koning[3], P. Bergman[1,4], P. Bernath[5,6,7], J. H. Black[1], U. Frisk[8], W. Geppert[9], T. I. Hasegawa[3,10], Å. Hjalmarson[1], S. Kwok[3,11], B. Larsson[12], A. Lecacheux[13], A. Nummelin[14], M. Olberg[1], Aa. Sandqvist[12], and E. S. Wirström[1]

[1] Onsala Space Observatory (OSO), Chalmers University of Technology, 43992 Onsala, Sweden
e-mail: carina@oso.chalmers.se
[2] LERMA, Observatoire de Paris, 61 Av. de l'Observatoire, 75014 Paris, France
[3] Department of Physics and Astronomy, University of Calgary, Calgary, AB T2N 1N4, Canada
[4] European Southern Observatory, Alonso de Cordova 3107, Vitacura, Casilla 19001, Santiago, Chile
[5] Department of Chemistry, University of Waterloo, Waterloo, ON N2L 3G1, Canada
[6] Department of Chemistry, University of Arizona, Tucson, AZ 85721, USA
[7] Department of Chemistry, University of York, Heslington, York YO10 5DD, UK
[8] Swedish Space Corporation, PO Box 4207, 17104 Solna, Sweden
[9] Molecular Physics Division, Department of Physics, Stockholm University AlbaNova, 10691 Stockholm, Sweden
[10] Institute of Astronomy and Astrophysics, Academia Sinica, PO Box 23-141, Taipei 106, Taiwan, R.O.C.
[11] Department of Physics, University of Hong Kong, Hong Kong, PR China
[12] Stockholm Observatory, AlbaNova University Center, 10691 Stockholm, Sweden
[13] LESIA, Observatoire de Paris, Section de Meudon, 5 place Jules Janssen, 92195 Meudon Cedex, France
[14] Computer science and engineering, Chalmers University of Technology, 41296 Göteborg, Sweden

Received 2 February 2007 / Accepted 17 September 2007

ABSTRACT

Aims. We investigate the physical and chemical conditions in a typical star forming region, including an unbiased search for new molecules in a spectral region previously unobserved.
Methods. Due to its proximity, the Orion KL region offers a unique laboratory of molecular astrophysics in a chemically rich, massive star forming region. Several ground-based spectral line surveys have been made, but due to the absorption by water and oxygen, the terrestrial atmosphere is completely opaque at frequencies around 487 and 557 GHz. To cover these frequencies we used the Odin satellite to perform a spectral line survey in the frequency ranges 486−492 GHz and 541−577 GHz, filling the gaps between previous spectral scans. Odin's high main beam efficiency, $\eta_{\rm mb} = 0.9$, and observations performed outside the atmosphere make our intensity scale very well determined.
Results. We observed 280 spectral lines from 38 molecules including isotopologues, and, in addition, 64 unidentified lines. A few U-lines have interesting frequency coincidences such as ND and the anion SH^-. The beam-averaged emission is dominated by CO, H_2O, SO_2, SO, ^{13}CO and CH_3OH. Species with the largest number of lines are CH_3OH, $(CH_3)_2O$, SO_2, $^{13}CH_3OH$, CH_3CN and NO. Six water lines are detected including the ground state rotational transition $1_{1,0}$–$1_{0,1}$ of o-H_2O, its isotopologues o-$H_2^{18}O$ and o-$H_2^{17}O$, the Hot Core tracing p-H_2O transition $6_{2,4}$–$7_{1,7}$, and the $2_{0,2}$–$1_{1,1}$ transition of HDO. Other lines of special interest are the 1_0–0_0 transition of NH_3 and its isotopologue $^{15}NH_3$. Isotopologue abundance ratios of D/H, $^{12}C/^{13}C$, $^{32}S/^{34}S$, $^{34}S/^{33}S$, and $^{18}O/^{17}O$ are estimated. The temperatures, column densities and abundances in the various subregions are estimated, and we find very high gas-phase abundances of H_2O, NH_3, SO_2, SO, NO, and CH_3OH. A comparison with the ice inventory of ISO sheds new light on the origin of the abundant gas-phase molecules.

Key words. ISM: abundances – ISM: individual objects: Orion KL – ISM: molecules – line: formation – line: identification – submillimeter

1. Introduction

To study the important ground-state rotational transition of water (including isotopologues), which traces shocks and heated star forming regions, is one of the main astronomy goals of the Odin satellite (Nordh et al. 2003, and subsequent papers in the A&A "Special Letters Edition: First Science with the Odin satellite") and hence also of this spectral line survey towards the Orion KL region. The first observations of this water line were performed by SWAS in 1998 (NASA's Submillimeter Wave Astronomy

⋆ Odin is a Swedish-led satellite project funded jointly by the Swedish National Space Board (SNSB), the Canadian Space Agency (CSA), the National Technology Agency of Finland (Tekes) and Centre National d'Etudes Spatiales (CNES). The Swedish Space Corporation was the prime contractor and also is responsible for the satellite operation.

⋆⋆ Section 10, Figs. 25–47 and Tables 5–35 are only available in electronic form at http://www.aanda.org

Satellite; Melnick et al. 2000 and subsequent ApJ papers in that issue). The Odin satellite provides a smaller beam than SWAS (2.1′ vs. 3.3′ × 4.5′), and our tunable SSB receivers enable a full line survey in this spectral window, including the water isotopologues ($H_2^{16}O$, $H_2^{17}O$, $H_2^{18}O$ and HDO), and a high energy p-H_2O transition.

A spectral scan offers an unbiased search for new molecules. It also creates opportunities to observe multiple transitions of the same species as a uniformly calibrated data set, and this can be used to calculate rotation temperatures, column densities, abundances, source sizes, optical depths, and isotopic elemental abundance ratios of the observed gases. The latter are important constraints for models of the Galactic chemical evolution. These models predict the elemental abundance evolution as a function of star formation history, stellar nucleosynthesis, and the degree of mixing of the gas in the ISM (Wilson & Rood 1994).

The Orion Molecular Cloud (OMC-1) is a well known massive star forming region (see Genzel & Stutzki 1989, for a review), and an ideal target for spectral line surveys at millimetre and submillimetre wavelengths due to its chemical richness and proximity (∼450 pc). The Kleinmann-Low nebula (Orion KL) is the brightest infrared region in the OMC-1 and is situated about 1′ NW of the Trapezium cluster. This region enables studies of the interaction between young massive stars and their parental molecular cloud. Powerful outflows, shocks and turbulence cause a very complex and chemically structured source, consisting of several distinct subsources.

There are five different components of radial velocity (e.g. Olofsson et al. 1981; Olofsson et al. 1982; Johansson et al. 1984; Friberg 1984; Genzel & Stutzki 1989; Wright et al. 1996; Schilke et al. 2001; Beuther et al. 2005; Olofsson et al. 2007, hereafter Paper I) within the ∼126″ Odin beam:

- *The ambient medium/Extended Ridge* (ER) with $\upsilon_{\rm LSR}$ ∼ 8 km s^{-1} in the south and an abrupt velocity shift across the KL region to $\upsilon_{\rm LSR}$ ∼ 10 km s^{-1} in the north. This extended emission is larger than our beam with quiescent, cool gas of narrow line widths of $\Delta\upsilon$ ∼ 3−5 km s^{-1}, a temperature of ∼20−60 K, and densities of 10^4−10^6 cm^{-3}.
- *The Plateau*: the out-flowing gas, centred close to IRc2 contains two outflows (Greenhill et al. 1998). The bipolar *High Velocity Flow* (HVF) in the SE-NW direction at $\upsilon_{\rm LSR}$ ∼ 10 km s^{-1} reaches velocities of 150 km s^{-1} and covers 40−70″. The second is a *Low Velocity Flow* (LVF) in the SW-NE direction at $\upsilon_{\rm LSR}$ ∼ 5 km s^{-1}, widths of ∼18 km s^{-1} ("the 18 km s^{-1} flow", Genzel et al. 1981), and a size of 15−30″. The temperature and density are 100−150 K and ∼10^5 cm^{-3}, respectively.
- *The Compact Ridge* (CR): a compact warm clump in the northern tip of the southern ER was first discovered by Johansson et al. (1984), approximately 10−15″ southwest of IRc2 with $\upsilon_{\rm LSR}$ ∼ 8 km s^{-1}, and line widths of $\Delta\upsilon$ ∼ 3 km s^{-1}. It may be the result of an interaction between the LVF and the ER that compressed the gas to higher densities ∼10^6 cm^{-3}, temperatures of 100−150 K, and to a small size of 6−15″.
- *The Hot Core* (HC): a warm star forming region which is heated internally, probably by one (or more) young massive protostars. The total size is ∼5−10″ (Hermsen et al. 1988a; Wilson et al. 2000) with smaller, very dense (n ∼ 10^7 cm^{-3}) clumps (Beuther et al. 2005). It is centred only 2″ from IRc2, at a projected distance of 10″ from the CR. The velocity is centred on $\upsilon_{\rm LSR}$ ∼ 3−6 km s^{-1} with line widths of $\Delta\upsilon$ ∼ 5−15 km s^{-1}. The range of temperatures obtained from inversion transitions of NH_3 is 165−400 K (Wilson et al. 2000).
- *Photo Dissociation Region* (PDR): the extended interface region between the molecular cloud and the foreground M42 HII region (Rodríguez-Franco et al. 1998, 2001; Wirström et al. 2006, and references therein) at velocities 8−10 km s^{-1}.

The various cloud components have been displayed in Fig. 6 of Genzel & Stutzki (1989), and Fig. 7 of Irvine et al. (1987). Figure 1 of Greenhill et al. (1998) shows a model of the bipolar High Velocity Flow and the Low Velocity Flow.

The Odin satellite has a large beam and covers high frequencies. This gives our survey the opportunity to simultaneously observe both the small, hot and dense regions, and the extended, cooler regions. Because of the complex source structure encompassed by our large antenna beam, we will compare our data with interferometric images for each species (see Paper I for an extensive list of spectral line survey references). In this way the origin and source sizes of our detected species can be checked.

The complete submm spectrum observed by Odin together with the proposed identification of each line can be found in Paper I. In the present paper we give a short description of our data in Sect. 2, and of the different analysis methods in Sect. 3. In Sect. 4 we present the results in tables and rotation diagrams together with spectra of typical or particularly important transitions. Tables of observed transitions can be found as electronic Tables in the online material (Tables 9 to 33). Tables 34 and 35 list our unidentified and tentatively identified lines. Section 4 also includes a short analysis for each molecule. The important water and CO lines are analysed in Sects. 5 and 6. An attempt to obtain molecular abundances in the different subregions of Orion KL and comparison with abundances in ice mantles of dust grains is found in Sect. 7. We end this paper with a discussion of source sizes and source structure in Sect. 8, followed by a short summary.

2. The line survey data

The observational method is presented in Paper I, and the data is analysed in this paper. These data were obtained with the Odin satellite from spring 2004 to autumn 2005 during four different runs. The spectral scan covers frequencies between 486–492 and 541–577 GHz and includes 280 spectral features from 38 species including isotopologues. The lines were identified using the Lovas SLAIMØ3 molecular line catalogue[1] (Lovas 2003), the Cologne Database for Molecular Spectroscopy[2] (CDMS, Müller et al. 2001) and the Jet Propulsion Laboratory[3] database (JPL, Pickett et al. 1998). Identifications are based not only on frequency coincidence, but also expected abundance, line strength, width and velocity, upper state energy, and the presence of other expected transitions of the molecule.

Most lines in our survey (205 out of 280 identified lines) are due to CH_3OH, $^{13}CH_3OH$, $(CH_3)_2O$, SO_2, and CH_3CN (Table 5, online material). A total of 64 lines (19% of all lines) could not be uniquely identified, although from frequency coincidences we have suggestions for a few identifications such as ND, the interstellar anion SH^-, SO^+, HNCO and CH_3OCHO (see Sect. 4 and Paper I). The spectroscopy still is sparse at higher frequencies

[1] Not available online, but some of its content is maintained under http://physics.nist.gov/PhysRefData/

[2] http://www.cdms.de

[3] http://spec.jpl.nasa.gov/

and a number of U-lines are likely to be poorly known transitions of the identified molecules and their isotopologues, including their vibrationally or torsionally excited states.

At 557 GHz the Odin 1.1 m mirror has a circular beam with FWHM of 2.′1. The main beam efficiency is $\eta_{\rm mb} = 0.9$. This in addition to being outside the atmosphere makes our intensity calibration very accurate. The intensity scale is expressed in terms of antenna temperature $T_{\rm A}^{*}$. In all calculations of the column densities the main beam efficiency is properly taken into account. The reconstructed pointing uncertainty is <15″ during most of the time. The coordinates of Orion KL in our survey are RA $05^{\rm h}35^{\rm m}14.^{\rm s}36$, Dec $-05°22'29.''6$ (J2000), and the frequency scale is set in relation to a source LSR velocity of +8 km s^{-1}. The spectral resolution is 1 MHz, and the typical rms reached is ∼25 mK per 1 MHz channel.

3. Data analysis methods – a simplified approach

The observed line emission is not restricted to one single subregion in Orion KL, but may be a complicated blend from several subregions with a complex line profile. Thus, when we attempt to derive column densities and abundances, we have to separate the emission into its constituent parts. The most simple approach whenever several emission features are clearly present, is to use least-square fits of Gaussians to the line profiles to separate their relative contributions. This can give a first order input to modelling attempts including current and future knowledge of the source structure. The resulting parameters are found in the online tables and in fitted spectra (Sect. 4). This is based on the assumptions that either all emissions are optically thin or that the emission subregions do not overlap each other spatially, and also that the velocity distributions are Gaussian.

The formal errors obtained from the rotation diagram method and forward model are given in each subsection. The formal errors obtained from the single line analysis and from the Gaussian decomposition of the lines are mostly below 20%, with weak lines having higher formal errors. We estimate the accuracy of our column densities results to be within a factor of 2−3. The uncertainties in the derived abundances can be higher because the adopted H_2 column density is also uncertain (see also Sect. 7). Details, definitions and additional uncertainties of the methods not discussed below are found in the online Sect. 10.

3.1. Single line analysis

With the assumption of optically thin emission, neglecting the background radiation, and assuming that the source fills the antenna main beam, the *beam averaged upper state* column density can be calculated as

$$N_{\rm u}^{\rm thin} = \frac{8\pi k \nu_{{\rm u}l}^2}{hc^3}\frac{1}{A_{{\rm u}l}}\int T_{\rm mb}\,{\rm d}\upsilon, \tag{1}$$

where k is the Boltzmann constant, $\nu_{{\rm u}l}$ is the frequency of the transition, h is the Planck constant, c is the speed of light, $A_{{\rm u}l}$ is the Einstein A-coefficient for the transition, and $T_{\rm mb}$ is the main beam brightness temperature. As customary the frequency ν has been converted to a Doppler velocity υ.

For a Boltzmann distribution, and with corrections for opacity and beam-filling, the true *total source-averaged* column density can be calculated as

$$N_{\rm LTE} = \frac{C_\tau}{\eta_{\rm bf}}\frac{8\pi k \nu_{{\rm u}l}^2}{hc^3}\frac{1}{A_{{\rm u}l}}\frac{Q(T)}{g_{\rm u}}{\rm e}^{E_{\rm u}/kT_{\rm ex}}\int T_{\rm mb}\,{\rm d}\upsilon, \tag{2}$$

where C_τ and $\eta_{\rm bf}$ are the opacity and beam-filling correction factors, $Q(T)$ is the partition function, g_u and E_u are the statistical weight and energy of the upper state, respectively, and $T_{\rm ex}$ is the excitation temperature for the transition.

For molecules where one or few transitions are observed, the column density is calculated using Eq. (2). If no information about optical depth or source-size is available these corrections are not taken into account, thus producing a *beam-averaged* and *not opacity corrected* column density.

3.2. Multiple line analysis

3.2.1. The rotation diagram method

When we have observed a number of lines with a wide range of upper-state energies, the rotation diagram method can be used according to

$$\ln\frac{N_{\rm u}^{\rm thin}}{g_{\rm u}} = \ln\frac{N_{\rm tot}}{Q(T)} - \frac{E_{\rm u}}{kT_{\rm ex}}. \tag{3}$$

To create a rotation diagram we plot $\ln(N_{\rm u}^{\rm thin}/g_{\rm u})$ as a function of the upper state energy $E_{\rm u}$ in a semi-log plot. A least squares fit to the data will then produce a straight line with slope $-1/T_{\rm ROT}$. If we extrapolate the line to $E_{\rm u} = 0$ K, we obtain the total column density from the intersection of the y-axis, y_0, and derive the total column density as

$$N_{\rm ROT} = Q(T)\,{\rm e}^{y_0}. \tag{4}$$

To correct for beam-filling, the right hand side of Eq. (4) is multiplied by $1/\eta_{\rm bf}$. Note that this constant does not change the rotation temperature. However, the optical depths can change the slope, and therefore the rotation temperature estimated from the rotation diagram.

The error bars shown in our rotation diagrams (Sect. 4) include 10% calibration error and the observed rms-noise.

3.2.2. The forward model (χ^2-method)

This model matches calculated opacity-corrected LTE integrated intensities and beam-filling in a χ^2 sense, to observed intensities vs. $E_{\rm u}$ (Nummelin et al. 1998; Nummelin et al. 2000; Lampton et al. 1976; Bevington 1969). Equation (3) in this case is modified to include optical depth and beam-filling corrections

$$\ln\frac{N_{\rm u}}{g_{\rm u}} + \ln C_\tau + \ln\frac{1}{\eta_{\rm bf}} = \ln\frac{N_{\rm tot}}{Q(T)} - \frac{E_{\rm u}}{kT_{\rm ex}}. \tag{5}$$

The intensity of each transition can be calculated using Eq. (12), with a specific set of free parameters $\eta_{\rm bf}$, $T_{\rm ROT}$ and $N_{\rm tot}$. The best fit to all the data, is obtained by finding the minimum of the reduced χ^2, which is defined as

$$\chi^2 = \frac{1}{n-p}\sum_{i=1}^{n}\left(\frac{I_i^{\rm obs} - I_i^{\rm calc}}{\sigma_i^{\rm obs}}\right)^2. \tag{6}$$

Here n is the number of data points, p is the number of free parameters, $\sigma_i^{\rm obs}$ is the 1σ uncertainty of the observed line intensity, $I_i^{\rm obs}$ and $I_i^{\rm calc}$ are the observed and calculated integrated intensities.

Note that the column density obtained with this method will be somewhat lower than that calculated from a simple rotation

diagram, since solutions producing $I_i^{\rm calc} < I_i^{\rm obs}$ are favoured compared to the opposite. This can be seen from the contribution to the χ^2-value from each transition giving χ_i^2.

$$\chi_i^2 = \left(\frac{I_i^{\rm obs} - I_i^{\rm calc}}{\sigma_i^{\rm obs}}\right)^2 \rightarrow \left(\frac{I_i^{\rm obs}}{\sigma_i^{\rm obs}}\right)^2 \quad (7)$$

when $I_i^{\rm calc} \rightarrow 0$. But if $I_i^{\rm calc} > I_i^{\rm obs}$, χ^2 will be unlimited, and this favours the lower model intensities (Nummelin et al. 1998).

4. Results

A summary of the observed features for all the species is presented in the online Table 5; the number of observed lines, the range in upper state energy, and the total integrated intensity.

A mean line-to-continuum ratio of 0.2 is reported in Paper I. The largest emission comes from CO with approximately 45% of the total spectral line emission. The second strongest emitter is H_2O (13%), followed by SO_2 (10%), SO (7%), ^{13}CO (7%) and CH_3OH (4%). The remaining species emit ∼14% of the total. However, these are *beam-average* values. Since the sizes of the SO_2, SO and CH_3OH emitting regions are much smaller than the extended CO emission, the relative amount of emission will change with a smaller beam, and will in addition not be the same for the different subregions.

The resulting column densities and rotation temperatures are shown in Tables 1 and 2, together with results from the ground-based submillimetre spectral scans by White et al. (2003, hereafter W03) from 455 to 507 GHz, Schilke et al. (2001, hereafter S01) from 607 to 725 GHZ, and Comito et al. (2005, hereafter C05) from 795 to 903 GHz. The number of lines used in our calculations are listed in parenthesis after the species in Table 1.

Differences may arise between the comparison surveys and ours due to the different beam-fillings. The comparison surveys W03 and S01 mostly use beam-averaged (with HPBW of 10″−12″) and not opacity-corrected column densities, while our results are corrected for beam-filling and optical depth, when possible. A second source of discrepancy is our effort to separate the emissions from different subregions, while the column densities in the comparison surveys are calculated from the total integrated intensity. Most of our column densities have therefore been calculated using the total integrated intensity and a source size of the main emitting component as a first approximation and comparison to S01 and W03. The column densities for the different subregions, are also calculated when possible, and have been corrected for opacity (if known) and beam-filling. In C05 beam-filling and optical depth correction are taken into account as well as separation into different subregions.

The listed source sizes are either calculated with Eq. (12), the χ^2-method, or taken from the literature. The size of the ER is assumed to be larger than our beam, although the East-West extent of the molecular ridge is rather limited (cf. Goldsmith et al. 1997). As excitation temperatures we use the population distribution temperatures $T_{\rm ROT}$ obtained from rotation diagrams. These temperatures are also used for species with similar excitation conditions. If no similar species exist, the temperatures are assumed to have the typical value for the emitting region: 100 K for the LVF, HVF and PDR, 60 K for the ER, 115 K for the CR, and 200 K for the HC. The rotation diagram technique as well as the forward model have been applied to all species that have a broad upper state energy range and four lines or more; SO_2, $^{34}SO_2$, SO, CH_3CN, CH_3OH, $^{13}CH_3OH$, H_2CS, and CH_3OCH_3; to calculate $N_{\rm ROT}$ and N_{χ^2}. Only in the methanol case, the forward model directly leads to a beam-filling and hence a source size. For the other species it was impossible to discriminate between solutions for different beam size/optical depth combinations.

In the online Table 6 our estimated isotopologue abundance ratios are listed, as well as comparisons with several other studies.

4.1. Outflow molecules

Sulphur-bearing species are considered to be tracers of massive *outflows* from a newly formed star. The high temperatures caused by the intense radiation from the driving source, or by shocks, can enhance the production of SO_2, SO and SiO. The line profile of the outflow shows a characteristic triangular line shape with broad wings as seen in examples of SO in Fig. 27, SiO in Fig. 28, SO_2 in Fig. 29, and in a comparison of SO_2 and SO in Fig. 41 (online material). The Orion outflows are also traced by other molecules like H_2O and CO: see Sects. 5 and 6, where also comparisons of $H_2^{18}O$, SO and SO_2 are shown.

4.1.1. Sulphur dioxide (SO_2/ $^{34}SO_2$)

We have observed 42 SO_2, and five $^{34}SO_2$ transitions. Typical line profiles are shown in Fig. 29 (online material) with different upper state energies. As proposed by Johansson et al. (1984) the complicated SO_2 and isotopologue line shapes suggest the presence of at least two velocity components, even though the emission primarily occurs in the outflow. Figure 1 shows a three-component Gaussian fit of a typical SO_2 line with line widths of ∼5 km s^{-1}, 18 km s^{-1} and 35 km s^{-1} from the CR, LVF and HVF, respectively. This is very similar to the Gaussian components of SO (Fig. 2), SiO (Fig. 3), and $H_2^{18}O$ (Fig. 36).

Figure 42 (online material) shows the size of the SO_2 emitting region vs. energy for each transition (Eq. (12)). The mean size is found to be 8″, which is consistent with the aperture synthesis mapping of Wright et al. (1996). This size is used for beam-filling corrections.

The high line density and the broadness of the SO_2 lines result in blends between the numerous transitions as well as with other species. There are 31 SO_2 transitions and four $^{34}SO_2$ transitions without blends, which are used in a rotation diagram shown in Fig. 43 (online material) producing $N_{\rm ROT} = (3.9 \pm 0.6) \times 10^{17}$ cm^{-2}, $T_{\rm ROT} = (132 \pm 8)$ K and $N_{\rm ROT} = (5.4 \pm 2.0) \times 10^{16}$ cm^{-2}, $T_{\rm ROT} = 125 \pm 30$ K for SO_2 and $^{34}SO_2$, respectively.

However, almost all of the SO_2 transitions are optically thick which lowers the SO_2 column density. The opacity is calculated using the same excitation temperature for all transitions and the column density obtained from the $^{34}SO_2$ rotation diagram (using an isotope ratio of 22.5, Table 6) and is found to be around 2–4 for most transitions. The opacity corrected rotation diagram is shown in Fig. 4 together with $^{34}SO_2$. The column density $N_{\rm ROT}^{\tau-{\rm corr}}$ increases to $(1.5 \pm 0.2) \times 10^{18}$ cm^{-2} and the temperature is lowered to 103 ± 3 K.

The isotopologue $^{34}SO_2$ is optically thin, hence no opacity correction is needed. But since the lines are weak and only four, the temperature from SO_2 is applied to the rotation diagram, which increases the $^{34}SO_2$ column slightly to 6.5×10^{16} cm^{-2}.

As a consistency check we also use Eq. (2) together with the single optically thin SO_2 line. This $16_{3,13}-16_{0,16}$ transition has an upper state energy of 148 K, and $\tau \sim 0.2$. The column density $N_{\rm LTE}$ obtained is 1.4×10^{18} cm^{-2}, in agreement with $N_{\rm ROT}^{\tau-{\rm corr}}$ and $N_{\rm ISO}$ from $^{34}SO_2$.

Table 1. Resulting column densities and rotation temperatures as well as comparison with W03, S01 and C05.

Species (No.)	Region	N [cm^{-2}]	T_{ex} [K]	Size[a] [″]	W03[b,c] N [cm^{-2}]	W03[b,c] T_{ex} [K]	S01[b,c] N [cm^{-2}]	S01[b,c] T_{ex} [K]	C05[d] N [cm^{-2}]	C05[d] T_{ex} [K]
SO_2 (31)	Total[c]	1.5×10^{18} [e]	103[e]	8[f]	1×10^{17}	136	6×10^{16}	187	9×10^{16}	130
	CR[g]	2.0×10^{17} [h]	(115)[i]	5[f]						
	LVF[g]	6.0×10^{17} [h]	103[j]	8[f]						
	HVF[g]	9.0×10^{17} [h]	103[j]	8[f]						
$^{34}SO_2$ (4)	Total[c] (outflow)	6.5×10^{16} [k]	103[j]	8[l]	8×10^{15}	156	8×10^{15}	192		
SO (5)	Total[c]	1.6×10^{17} [e]	132[e]	18[f]	3×10^{17}	(72)[i]	2×10^{17}	64	5×10^{16}	150
	CR[g]	1.7×10^{16} [h]	(115)[i]	6[f]						
	LVF[g]	9.3×10^{16} [h]	132[m]	11[n]						
	HVF[g]	8.5×10^{16} [h]	(100)[i]	18[n]						
^{33}SO (3)	Total[c] (outflow)	1.7×10^{15} [o]	132[m]	18[p]						
^{34}SO (2)	Total[c] (outflow)	8.4×10^{15} [o]	132[m]	18[p]	1×10^{16}	89				
SiO (1)	Total[c]	4.0×10^{15} [q]	(100)[i]	14[f]			5×10^{14}	110	1×10^{15}	(150)[i]
	LVF[g]	3.3×10^{15} [h]	(100)[i]	10[n]						
	HVF[g]	1.8×10^{15} [h]	(100)[i]	14[r]						
^{29}SiO (1)	Total[c] (outflow)	2.0×10^{14} [o]	(100)[i]	14[r]						
H_2S (1)	LVF[g]	4.5×10^{16} [o]	(100)[i]	(15)[i]			1×10^{16}	129	4×10^{16}	140
	HC[g]	2.7×10^{16} [o]	(200)[i]	(10)[i]						
CH_3CN (9)	Total[c] (HC)	5.0×10^{15} [k]	137[k]	(10)[i]	3×10^{15}	227			4×10^{15}	250
HC_3N (2)	Total[c] (HC)	1.8×10^{15} [o]	(200)[i]	(10)[i]	1×10^{15}	164				
OCS (3)	Total[c] (HC)	1.7×10^{16} [o]	(200)[i]	(10)[i]	9×10^{16}	106				
NO (1)	Total[c] (HC)	2.8×10^{17} [o]	(200)[i]	(10)[i]			1×10^{17}	90	2×10^{17}	150
NH_3 (1)	CR[g]	4.0×10^{16} [h]	(115)[i]	17[f]						
	HC[g]	1.6×10^{18} [q]	(200)[i]	8[f]						
$^{15}NH_3$ (1)	Total[c] (HC)	3.5×10^{15} [o]	(200)[i]	8[s]						
CH_3OH (50)	Total[c]	3.4×10^{18} [e]	116[e]	6[f,t]	9×10^{16}	599	5×10^{16}	303		
	HC[g]	7.9×10^{17} [u]	178[u]	6[n]					3×10^{16}	220
	CR[g]	2.4×10^{18} [u]	98[u]	6[f]					5×10^{16}	160
$^{13}CH_3OH$ (14)	Total[c] (CR)	5.9×10^{16} [k]	115[k]	6[v]			1×10^{16}	229		
$(CH_3)_2O$ (37)	Total[c] (CR)	1.3×10^{17} [k]	112[k]	6[v]	1×10^{16}	157	3×10^{16}	360	2×10^{16}	160
H_2CS (4)	Total[c] (CR)	1.3×10^{15} [k]	93[k]	14[x]						
H_2CO (3)	LVF[g]	4.3×10^{15} [o]	(100)[i]	(15)[i]	1×10^{16}	(166)[i]	3×10^{15}	190	2×10^{15}	155
	CR[g]	2.0×10^{16} [q]	(115)[i]	14[f]						
$H_2^{13}CO$ (1)	Total[c] (CR)	3.3×10^{14} [o]	(115)[i]	14[x]	1×10^{15}	(166)[i]				
HDCO (2)	Total[c](CR)	2.7×10^{14} [o]	(115)[i]	14[x]						
CS (1)	LVF[g]	3.6×10^{15} [o]	(100)[i]	(15)[i]			1×10^{15}	127	3×10^{15}	100
	HC[g]	2.9×10^{15} [o]	(200)[i]	(10)[i]					1×10^{16}	190
	N as CR[g]	8.0×10^{15} [q]	(115)[i]	20[f]						
	N as ER[g]	4.2×10^{14} [q]	(60)[i]	...						
^{13}CS (1)	Total[c] as CR	1.3×10^{14} [o]	(115)[i]	20[y]	2×10^{14}	(120)[i]				
	Total[c] as ER	7.1×10^{12} [o]	(60)[i]	...						
HNC (1)	LVF[g]	3.6×10^{14} [o]	(100)[i]	(15)[i]					5×10^{14}	(150)[i]
	HC[g]	4.4×10^{14} [o]	(200)[i]	(10)[i]						
	ER[g]	1.9×10^{12} [o]	(60)[i]	...						
CN (2)	PDR/ER[g]	4.9×10^{13} [o]	(100)[i]	...						
	HC[g]	7.9×10^{15} [o]	(200)[i]	(10)[i]						
N_2H^+ (1)	Total[c] (ER)	1.0×10^{12} [o]	(60)[i]	...						

[a] The column density is a source-average if a source size is given, else it is a beam-average. [b] HPBW is 10–12″ in comparison surveys, and the column densities are beam-averaged and not corrected for opacity. [c] From the total integrated intensity of the line(s). [d] Beam-filling and opacity corrected, as well as separation into components. [e] From an opacity-corrected rotation diagram. [f] From optically thick line(s). [g] From Gaussian decomposition. [h] N_{LTE}, opacity corrected. [i] Not calculated by the authors. [j] Temperature from SO_2 opacity-corrected rotation diagram. [k] From a non opacity-corrected rotation diagram. [l] Size from SO_2. [m] Temperature from a SO opacity-corrected rotation diagram. [n] Opacity corrected. [o] N_{LTE}. [p] Size from SO total integrated intensity. [q] N_{ISO}. [r] Size from SiO total integrated intensity. [s] Size from NH_3. [t] From the forward model. [u] From an opacity corrected two-component rotation diagram. [v] Size from CH_3OH. [x] Using H_2CO calculated source size. [y] Using size from CS.

Our column densities of both isotopologues are much larger than in the comparison surveys. This can partly be caused by our beam-filling correction with a rather small size, and the non-correction for opacity in W03 and S01. However, Johansson et al. (1984) and Serabyn & Weisstein (1995) obtain a column density of about 1×10^{18} cm^{-2} (corrected for our source size) in agreement with our value.

Column densities for each subregion are estimated from the Gaussian components shown in Fig. 1 (Table 1). The rarer isotopologues are too weak for a Gaussian decomposition so

Table 2. Column density results for water, C, CO and H_2.

Species	Region	T_{ex} [K]	N_{LTE} [cm^{-2}]	N_{ISO} [cm^{-2}]	N_{H_2} [cm^{-2}]	Size[a] [']	τ
C		100	5.6×10^{17}			...	
CO	PDR[b]	100	1.6×10^{17}	1.6×10^{18} [c]	2.0×10^{22}	...	
	LVF	100		2.5×10^{19} [c]	3.2×10^{23}	(30)[d]	
	HVF	100	1.2×10^{18}	3.1×10^{18} [e]	3.9×10^{22}	70[f]	
^{13}CO	PDR/ER[b]	100	5.7×10^{16}	5.4×10^{16} [c]		...	
	LVF	100	3.9×10^{17}	4.2×10^{17} [c]		30	
	HVF	100	5.2×10^{16}			70	
C^{17}O	PDR/ER[b]	100	2.5×10^{15}			...	0.07
	LVF	100	2.0×10^{16}			30	0.1
C^{18}O	PDR/ER[b]	100	8.9×10^{15}	9.8×10^{15} [c]		...	0.3
	LVF	100	6.7×10^{16}	7.7×10^{16} [c]		30	0.3
H_2O	Total[g]	72		1.7×10^{18} [h]		(15)[d]	~1100
	CR	115		5.6×10^{17} [h]		(6)[d]	~860
	LVF	72		8.7×10^{17} [h]		(15)[d]	~1900
	HVF	72	8.0×10^{17} [i]	8.8×10^{17} [h]		70[f]	~910
	HC	200	1.2×10^{19} [j]			10	0.3[k]
$H_2^{17}O$	Total[g]	72	1.3×10^{15} [l]			15	0.9
	CR	115	4.4×10^{14} [l]			6	0.7
	LVF	72	6.7×10^{14} [l]			15	1.5
	HVF	72	6.8×10^{14} [l]			15	0.7
$H_2^{18}O$	Total[g]	72	5.0×10^{15} [l]	5.0×10^{15} [h]		15	3.4
	CR	115	1.8×10^{15} [l]	1.7×10^{15} [h]		6	2.6
	LVF	72	2.7×10^{15} [l]	2.6×10^{15} [h]		15	5.9
	HVF	72	2.8×10^{15} [l]	2.7×10^{15} [h]		15	2.8
HDO	Total[g]	72	9.1×10^{15}			15	1.5[k]
	CR	115	1.8×10^{16}			6	3[k]
	LVF	72	4.5×10^{15}			15	0.3[k]
	HC	200	1.5×10^{16}			10	0.5[k]

[a] The column density is a source-average if a source size is given, else it is a beam-average. [b] The narrow component from CO isotopologues contains emission from both PDR and ER, the CO narrow component only from the PDR, hence the PDR column density for CO here is divided by two as motivated in Sect. 5. [c] Using C^{17}O together with [^{18}O/^{17}O] = 3.9, [^{16}O/^{18}O] = 330, and [^{12}CO/^{13}CO] = 60. [d] Indirect size estimated using isotopologues. The full size may be larger. [e] Using ^{13}CO together with [^{12}CO/^{13}CO] = 60. [f] Hjalmarson et al. (2005). [g] From the total integrated intensity of the line. [h] Using opacity and beam-filling corrected *o*-$H_2^{17}O$ together with [^{18}O/^{17}O] = 3.9 and [^{16}O/^{18}O] = 330. [i] From HVF Gaussian fit of *o*-H_2O, opacity and beam-filling corrected. [j] Using beam-filling corrected *p*-H_2O. [k] Calculated with Eq. (15). [l] Opacity and beam-filling corrected.

opacities cannot be calculated by comparison with isotopologues. Still, the components are likely to be optically thick and therefore the sizes of the emitting regions are calculated with T = 115 K for the CR, and T = 103 K for the LVF and HVF. The source sizes are found to be 5″ for the CR and 8″ for both the LVF and HVF. These sizes correspond to optical depths of about 2–3. The opacity-corrected column densities become 2×10^{17} cm^{-2}, 6×10^{17} cm^{-2}, and 9×10^{17} cm^{-2} for the CR, LVF and HVF, respectively.

The elemental isotopic ratio of [^{32}S/^{34}S] can be estimated from a comparison of the optically thin column densities. In this way we obtain an isotopic ratio of 23 ± 7, in agreement with most other comparison studies listed in Table 6.

As expected, no vibrationally excited lines were found. The $5_{5,1}-4_{4,0}$ v_2 bending mode transition has the lowest upper state energy (822 K) of all v_2 lines in our spectral range. The calculated expected peak temperature of this line is 34 mK, with an expected line width of 23 km s^{-1}. Such weak and broad lines are marginally below our detection limit.

4.1.2. Sulphur monoxide (SO/^{33}SO/^{34}SO)

Typical line profiles are shown in Fig. 27 (online material). The line profiles of the high energy transitions show an even broader outflow emission, and with more pronounced high velocity line wings than does SO_2 (comparison in Fig. 41 in the online material). As for SO_2, the emission is primarily from the Plateau, and Friberg (1984) has shown the bipolar nature of the HVF component. The ratios of SO_2 and SO emission lines vs. velocity, also show a high degree of similarity between the line profiles except in the high velocity regime between −30 to −5 km s^{-1}. At these velocities SO has stronger emission than SO_2.

Figure 2 shows the $13_{12}-12_{11}$ transition with a three-component Gaussian fit. The broad HVF component has a FWHM width of ~35 km s^{-1} at υ_{LSR} ~ 9 km s^{-1}. The LVF component has widths of 18 km s^{-1} at υ_{LSR} ~ 8 km s^{-1}. In addition to the LVF and HVF components a third from the CR appears with a width of 5 km s^{-1} at υ_{LSR} ~ 9–10 km s^{-1}.

The most likely source size is 18″, calculated using the three optically thick SO lines. This is in agreement with the aperture synthesis mapping by Beuther et al. (2005), and Wright et al. (1996), who find a larger source size for SO than for SO_2. The source size 18″ is used for beam-filling correction.

The rotation diagram in Fig. 5 (calculated with the total integrated intensity of the lines) displays our five SO lines. The rotation temperature without any corrections is (59 ± 2 K) and the column density N_{ROT} is (1.5 ± 0.2) × 10^{17} cm^{-2}. However, the three higher energy lines have optical depth of ~3, whereas

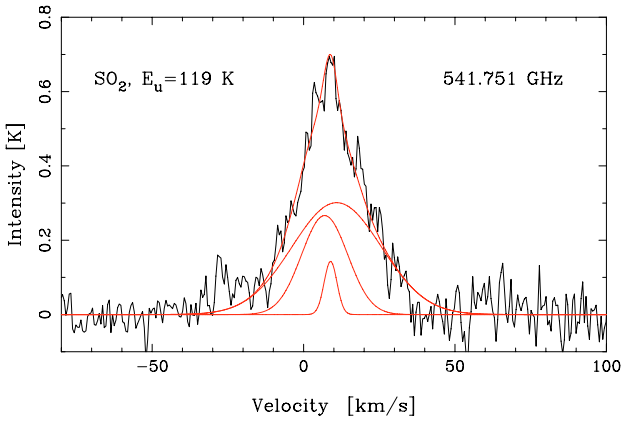

Fig. 1. The $14_{3,11}$–$13_{2,12}$ SO_2 transition with a three-component Gaussian fit shown together with the individual Gaussians. The line widths are 5 km s^{-1}, 18 km s^{-1} and 35 km s^{-1} from the CR, LVF and HVF, respectively.

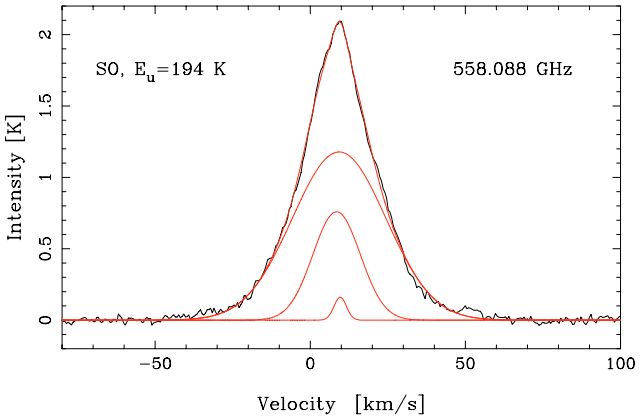

Fig. 2. The 13_{12}–12_{11} SO transition with a three-component Gaussian fit shown together with the individual Gaussians. The line widths are 5 km s^{-1}, 18 km s^{-1} and 35 km s^{-1} from the CR, LVF and HVF, respectively.

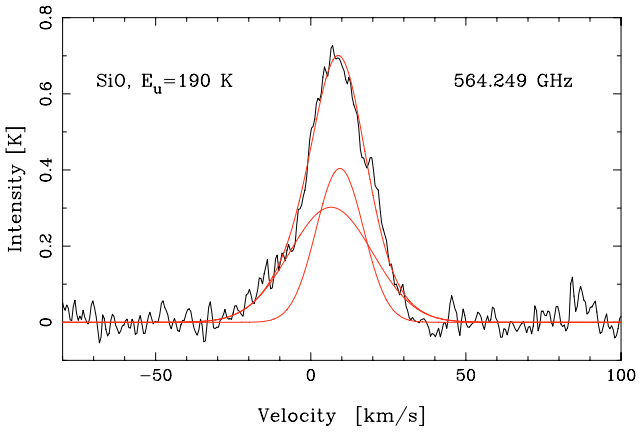

Fig. 3. The J = 13–12 SiO transition with a two-component Gaussian fit shown together with the individual Gaussians. The line widths are 18 km s^{-1} and 31 km s^{-1} from the LVF and HVF, respectively.

the two low energy transitions are optically thin with $\tau \sim 0.1$ (Eq. (15)). We make an optical depth correction for all five transitions and plot them again in Fig. 5 together with a new fit. Note that the correction is substantial for the high energy, optically thick lines (cf. Serabyn & Weisstein 1995). The rotation temperature obtained is higher than without corrections, 132 ± 22 K, but the resulting column density is only slightly higher than that found without the corrections, $N_{\rm ROT}^{\tau-{\rm corr}} = (1.6 \pm 0.5) \times 10^{17}$ cm^{-2}. This is in agreement with the column density obtained from ^{34}SO, $N_{\rm ISO} = 1.9 \times 10^{17}$ cm^{-2} (using 22.5 for [^{32}S/^{34}S]). The two optically thin SO transitions gives $N_{\rm LTE} = 1.8 \times 10^{17}$ cm^{-2}. The column densities for both isotopologues are calculated with the rotation temperature from SO.

The isotopologues, two ^{33}SO and three ^{34}SO transitions, are optically thin with opacities around 0.02 and 0.13, respectively. These transitions are plotted in Fig. 5 with the integrated intensities multiplied by appropriate isotopic ratios (5.5 for [^{34}S/^{33}S], Table 6). As seen in Fig. 5, the result of the isotopic ratio corrections is consistent with the optical depth corrected SO transitions.

As for SO_2 the column densities for each SO subregion are estimated from the Gaussian components shown in Fig. 2. Opacities cannot be calculated by comparison with the rarer isotopologues since they are too weak for a Gaussian decomposition. However, the components are likely to be optically thick and therefore the sizes of the emitting regions are calculated with T = 115 K for the CR, T = 132 K for the LVF, and T = 100 K for the HVF. The source sizes of the CR, LVF and HVF are found to be 6″, 10″ and 14″, respectively. These sizes may be larger if the opacities are low. Combining calculations of source size, optical depths, and column densities, the sizes for the LVF and HVF increase slightly to 11″ and 18″, respectively. These sizes correspond to optical depths of about 2.5 and 1.0 for respective region. The opacity-corrected column densities become 1.7×10^{16} cm^{-2}, 9.3×10^{16} cm^{-2}, and 8.5×10^{16} cm^{-2} for the CR, LVF and HVF, respectively.

The elemental isotopic ratio of [^{32}S/^{34}S] and [^{34}S/^{33}S] can be estimated from comparisons of the column densities of the isotopologues and the optically thin SO transitions. We obtain isotopic ratios of 21.0 ± 6 and 4.9, respectively in agreement with most other comparison studies listed in Table 6.

4.1.3. Silicon monoxide (SiO/^{29}SiO/^{30}SiO)

We have observed the transition J = 13–12 for each isotopologue, and we show the SiO and ^{29}SiO transitions in Fig. 28 (online material). As for SO_2 and SO, the complicated line profile of SiO suggests emission from both the LVF and the bipolar HVF (present in aperture synthesis maps of Wright et al. 1996), with widths of 18 and 31 km s^{-1} at $v_{\rm LSR}$ velocities of 9 and 7 km s^{-1}, respectively. Figure 3 shows the two-component Gaussian fit to SiO. The ^{29}SiO transition is located in the high-velocity wing of o-H_2O (at $v_{\rm LSR} \sim -130$ km s^{-1}). The width is 21 km s^{-1} at a centre velocity of ~9 km s^{-1}. The ^{30}SiO transition is a questionable assignment due to its narrow line width of 7.5 km s^{-1}.

Comparison of the peak antenna temperatures of SiO and ^{29}SiO shows that the SiO transition has an optical depth of ~1.0. The source size (Eq. (12)) is found to be 14″. This is used as beam-filling correction. Using a LVF temperature of 100 K (about the same temperature as the SO_2 rotation temperature), the total integrated intensity, and the simple LTE approximation, the opacity-corrected column density is found to be 4.0×10^{15} cm^{-2} for SiO.

The decomposition into subregions results in LVF and HVF source sizes of 8″ and 7″ with temperatures of 100 K for both sources. The rather small values are most likely due to the low opacity in these components and are therefore only lower

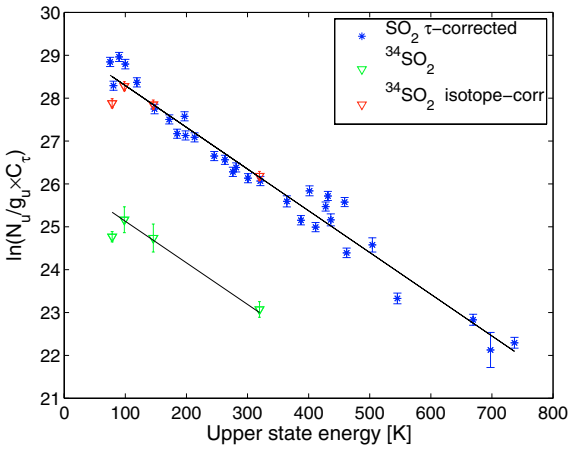

Fig. 4. Rotation diagram for SO_2 produces T_{ROT} = 103 K (extended source). The $^{34}SO_2$ fit uses the SO_2 rotation temperature.

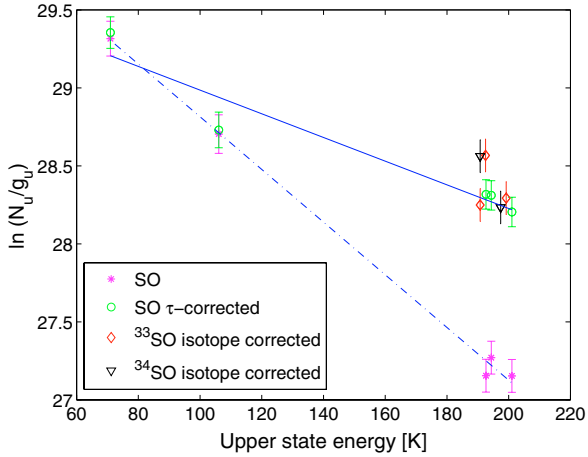

Fig. 5. Rotation diagram for SO and isotopologues (extended source). The isotopologues are plotted multiplied by respective isotopic ratio. Two fits are made: the first (dashed-dotted line) is not opacity corrected (T_{ROT} = 59 K), while the second (solid line) is corrected for opacity (T_{ROT} = 132 K).

limits. Assuming that the opacity in the LVF is about the same as for the total integrated emission, the LVF opacity-corrected source size increases to 10″. The opacity in the HVF is most likely less than in the LVF. As an upper limit the size is assumed to be the same as for the total integrated emission, which results in an HVF opacity of about 0.4. The sizes are consistent with Beuther et al. (2005). Note the similarity of the SO and SiO source sizes. In Sect. 6 the $H_2^{18}O$ sizes will also be shown to be similar. These source sizes are used to correct for beam-filling, and the resulting LVF and HVF opacity-corrected column densities are 3.3×10^{15} and 1.8×10^{15} cm^{-2}, respectively.

4.2. Outflow and Hot Core molecule

The *Hot Core* is a collection of warm (≳200 K) and dense ($n \sim 10^7$ cm^{-3}) clumps of gas. The dominating species are oxygen-free, small, saturated nitrogen-bearing molecules such as CH_3CN and NH_3. Most N-bearing molecules are strong in the HC, while the oxygen-bearing molecules peak toward the CR (e.g. Blake et al. 1987, hereafter B87; Caselli et al. 1993; Beuther et al. 2005). CH_3OH is an exception with pronounced emissions from the HC as well as from the CR. In addition, high levels of deuterium fractionation are found here. Since the HC region

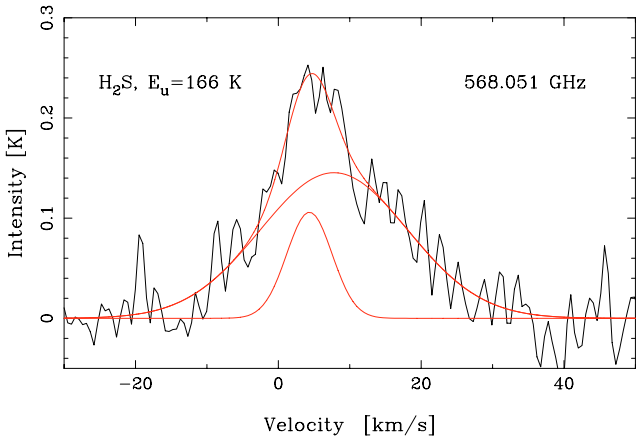

Fig. 6. The H_2S $3_{3,1}$–$3_{2,2}$ transition with a two-component Gaussian fit shown together with the individual Gaussians. The line widths are 8 km s^{-1} and 24 km s^{-1} from the HC and outflow, respectively.

probably contains one or more massive protostars it presents an ideal opportunity to study active gas-phase chemistry. And due to the high temperatures in both the HC and CR, the gas-phase chemistry will get a significant contribution of molecules from grain surface chemistry through evaporation of the icy mantles caused by the intense UV radiation from newly formed stars.

4.2.1. Hydrogen sulphide (H_2S)

We observe only the $3_{3,1}$–$3_{2,2}$ transition of H_2S, with emission from the HC and LVF, illustrated by a Gaussian decomposition in Fig. 6. The emission from the HC component has a width of ∼8 km s^{-1} at $\upsilon_{LSR} \sim 5$ km s^{-1} between velocities −5 to +15 km s^{-1}. The LVF emission has a width of ∼24 km s^{-1} at $\upsilon_{LSR} \sim 8$ km s^{-1}. The line is also shown in the bottom of Fig. 25 (online material) together with other comparison HC molecules.

The column densities are consistent with the comparison surveys assuming typical source sizes and temperatures.

4.3. Hot Core molecules

4.3.1. Methyl cyanide (CH_3CN)

Previous observations of the high density tracer CH_3CN (e.g. Blake et al. 1986; Wilner et al. 1994) have shown that the low-J transitions in the vibrational ground state appears to be a mix of CR and HC emission, while the high-J transitions and all the vibrationally excited lines originate in the HC only. This is also confirmed in our survey where we observe the 30_K–29_K transitions with K = 0–9, and 31_K–30_K with K = 0–6 and 9. These lines suggest an origin in the HC at $\upsilon_{LSR} \sim 5$–6 km s^{-1} and widths of ∼8–9 km s^{-1}, also consistent with W05 and C05. The 30_4–29_4 ground state transition is shown in Fig. 25 (online material). In addition we see a number of weak vibrational lines from the $\upsilon_8 = 1$ bending mode with 30_K–29_K where K = 0–3. In total we observe 17 line features from this molecule. Nine of these are free from blends and are used in the rotation diagram (Fig. 7). Due to the weak lines the rotation temperature of 137 ± 25 K and the column density of $(5.0 \pm 3.6) \times 10^{15}$ cm^{-2} are comparatively uncertain. The temperature is rather low compared to W03 who estimate the temperature to 227 K, and C05 to 250 K. Still, the column density agrees well with B87, Sutton et al. (1995, hereafter S95), W03, and C05.

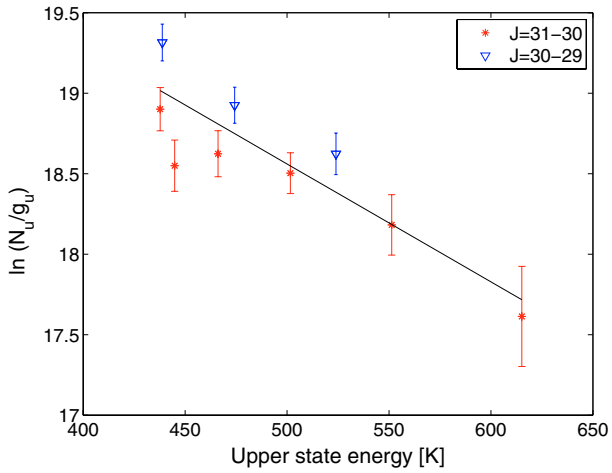

Fig. 7. Rotation diagram for CH_3CN producing T_{ROT} = 137 K (extended source).

Wilner et al. (1994) find an opacity of the HC emission of at most a few for the main lines. This could explain the rather low [$^{13}C/^{12}C$] ratios in Blake et al. (1986) and Turner (1991). Sutton et al. (1986) suggests significant opacity from their statistical equilibrium calculations, if the HC is as small as 10″. This would give even higher column densities in the HC.

The partition function is calculated as recommended in Araya et al. (2005).

4.3.2. Cyanoacetylene (HC_3N)

Two transitions of cyanoacetylene are seen, of which J = 54–53 is a blend with CH_3OH. The transition J = 60–59 is shown in Fig. 25 (online material). HC emission is here evident at v_{LSR} ~ 5–6 km s^{-1} and a line width of ~10 km s^{-1}. The column density is calculated with the simple LTE approximation and is in agreement with W03.

4.3.3. Carbonyl sulphide (OCS)

We have identified three transitions from carbonyl sulphide, J = 47–46, J = 45–44, and J = 46–45 (shown in the online Fig. 25). The emission has its origin in the HC with v_{LSR} ~ 6 km s^{-1}, and a width of ~6 km s^{-1}.

The estimated column density is about five times lower than found by both W03 and S95.

4.3.4. Nitric oxide (NO)

We observe three features with $^2\Pi_{3/2}$, J = 11/2–9/2, and $^2\Pi_{1/2}$, J = 11/2–9/2 from both e and f species, which are composed of twelve non-resolved hyperfine transitions. No separation into components is possible due to blends between the hyperfine transitions and other species. Our estimated rotation temperature from our transitions with upper state energies of 84 K and 232 K is found to be 75 K. This is highly uncertain due to the severe blends in both low energy transitions. Since S01 and C05 observed HC emission we therefore use a typical HC temperature of 200 K and source size of 10″. The resulting column density (using the high energy line) is in agreement with S01 and C05.

4.4. Hot Core and Compact Ridge molecules

The *Compact Ridge* is a more quiescent region as compared to the Hot Core. Here we find high abundances of oxygen-bearing species such as CH_3OH, $(CH_3)_2O$ and HDO (B87; Caselli et al. 1993; Beuther et al. 2005). As in the HC, the evaporation of the icy mantles in the warm CR will release molecules produced by grain surface chemistry into the gas-phase.

4.4.1. Ammonia ($NH_3/^{15}NH_3$)

The symmetric top ammonia molecule is a valuable diagnostic because its complex energy level structure covers a very broad range of critical densities and temperatures (see Ho & Townes 1983, for energy level diagram and review).

Many observations have been made of the NH_3 inversion lines at cm wavelengths since the first detection by Cheung et al. (1968). The upper state energy of the lowest metastable inversion lines are 24 K and 64 K comparable to 28 K for the rotational ground state transition 1_0–0_0 at 572 GHz. The critical density is very different though, and is 3.6 × 10^7 cm^{-3} (calculated for 20 K) for the rotational ground state transition, and about 10^3 cm^{-3} for the inversion lines. The non-metastable inversion lines also trace higher excitation and density regions. Comparison of all these transitions could therefore give valuable information about both high- and low-density and temperature regions. The previous low quantity of observations of rotational transitions is due to the fact that they fall into the submillimetre and infrared regimes, which are generally not accessible from the ground and therefore has to be observed from space.

Observations of both metastable and non-metastable inversion lines (e.g. Batrla et al. 1983; Hermsen et al. 1988a,b; Migenes et al. 1989) have shown NH_3 in the HC, CR, ER and LVF regions. The existence of an outflow component was however questioned by Genzel et al. (1982) since the hyperfine satellite lines could cause the broadness of the line if the opacity is large.

The rotational ground state transition was first and solely detected twenty-four years ago with the Kuiper Airborne Observatory (Keene et al. 1983). Note that the Kuiper Airborne Observatory had a similar beam size (2′) to that of Odin (2.′1). Using Odin, sensitive observations have been made recently for example towards Orion KL and the Orion Bar (Larsson et al. 2003), the ρ Oph A core (Liseau et al. 2003), Sgr B2 (Hjalmarson et al. 2005), as well as the molecular cloud S140. The resulting NH_3 abundance in the Orion Bar is 5 × 10^{-9} (Larsson et al. 2003).

In this spectral survey we have observed the rotational ground state 1_0–0_0 transitions of NH_3 and $^{15}NH_3$, which are shown in Fig. 25 (online material). We show the NH_3 transition twice to emphasize the line wings. Our peak temperature agrees to within 5% with Larsson et al. (2003) who used a rather different Odin observational setup, demonstrating the excellent calibration of the Odin data. The vibrational transition v_2 = 1 of this line at 466 GHz has previously been observed by Schilke et al. (1992).

Figure 8 shows our two-component Gaussian fit to the NH_3 line which has pronounced features of the CR and a broad component. The line widths are 5 and 16 km s^{-1} at LSR velocities 8, and 9 km s^{-1} for the CR and broad components, respectively. The CR emission was also observed by Keene et al. (1983), while the broader component clearly seen in our Odin data, was only marginally present in their lower signal-to-noise data. Our $^{15}NH_3$ spectrum shows only evidence of the

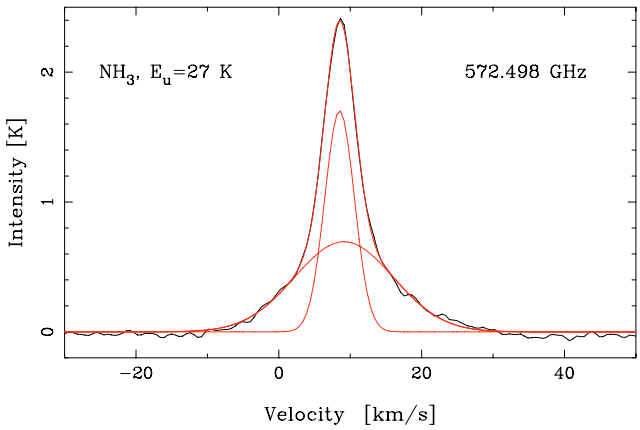

Fig. 8. The NH_3 transition with a two-component Gaussian fit shown together with the individual Gaussians. The line widths are 5 km s^{-1} and 16 km s^{-1} from the CR and HC/outflow, respectively.

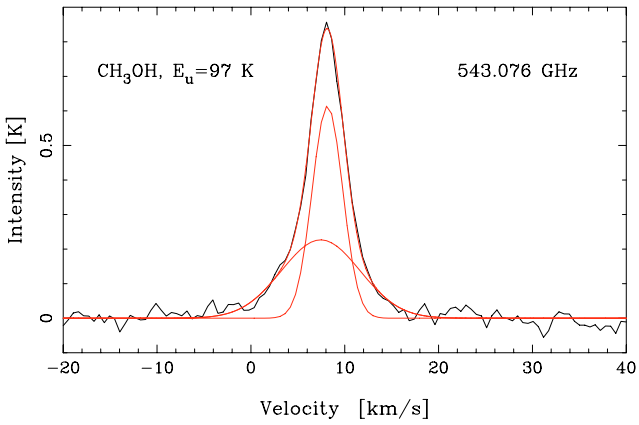

Fig. 9. Methanol line with a two-component fit shown together with the individual Gaussians. The line widths are 4 km s^{-1} and 10 km s^{-1} from the CR and HC, respectively.

HC component (cf. Hermsen et al. 1985), with a width of ∼7 km s^{-1} at $v_{LSR} \approx 7$ km s^{-1}. The width of the broad NH_3 component may seem too large to have an origin in the HC. However, the broadness of the line may be caused by opacity broadening (Eq. (21); cf. Phillips et al. 1979). From Eq. (16) combined with an assumed $^{14}N/^{15}N$ isotope ratio of 450 (Table 6), we estimate optical depths of ∼100 and ∼0.3 in the NH_3 and $^{15}NH_3$ HC lines, respectively. According to Eq. (21) this will broaden the optically thick NH_3 emission line by approximately 2.6 times from a line width comparable to the optically thin $^{15}NH_3$ HC emission to a resulting width of ∼17 km s^{-1}. This is very close to the width of our Gaussian HC component, 16 km s^{-1}. However, the high opacity in this component will cause the line profile to be flat topped with little or no line wings. Hence our broad Gaussian component not only contains the opacity broadened HC emission but also the outflow component seen by e.g. Wilson et al. (1979) and Pauls et al. (1983), in our spectrum visible as pronounced line wings. Alternatively it could be that the HC emission is hidden by optically thick NH_3 LVF emission just as in case of water (cf. Sect. 6.2.2).

The NH_3 source sizes of the CR and HC regions are found to be 17″ and 8″, respectively, and are used as beam-filling corrections. The rather large CR size as compared to the 6″ mean source size obtained for CH_3OH, might be due to the low upper state energy of 27 K for NH_3. Figure 12 shows the decreasing methanol source size with upper state energy, where the lowest methanol transitions with upper state energies of 40−100 K reach a source size of ∼11″. Hermsen et al. (1988b) find source sizes of 15″ and 6″ for the CR and HC, respectively, in agreement with our calculations. VLA maps by Migenes et al. (1989) also show that the HC emission is clumped on 1″ scales.

Hermsen et al. (1988b) find a HC temperature of 160 ± 25 K and a CR temperature above 100 K. In addition Wilson et al. (2000) detect an even hotter HC component with a temperature of about 400 K. Using HC and CR temperatures of 200 K and 115 K, respectively, we find a NH_3 HC column density (calculated from the optically thin $^{15}NH_3$ line) of 1.6×10^{18} cm^{-2}. Our comparison surveys have no observations of this molecule, but our result agrees with Genzel et al. (1982), who report column densities of NH_3 that reach 5×10^{18} cm^{-2} from the HC, with size 10″ and temperatures about 200 K. Their observations also confirmed increasing line width with increasing optical depth. Hermsen et al. (1988b) and Pauls et al. (1983) find values of 1×10^{18} cm^{-2} for the HC.

The optically thick NH_3 CR column density is found to be 3.4×10^{15} cm^{-2}. Optical depth broadening is used to estimate the opacity in this component. Batrla et al. (1983) found an intrinsic velocity width of 2.6 km s^{-1} by ammonia inversion lines observations. From a comparison with the observed line width, the opacity is estimated to be about 12 in the CR component. The opacity-corrected CR column density then becomes 4.0×10^{16} cm^{-2}. This is in agreement with the estimation of Hermsen et al. (1988b) who find a column density in the range 8×10^{15}−8×10^{16} cm^{-2} from the metastable (6,6) inversion line.

4.4.2. Methanol ($CH_3OH/^{13}CH_3OH$)

Methanol is an organic asymmetric top molecule with many energy levels (see energy level diagram in Nagai et al. 1979), and behaves like two different species labelled A and E for symmetry reasons.

We have observed 76 methanol lines of which 42 are from the $v_t = 1$ state, which is the first excited vibrational state of the torsional motion of the CH_3 group relative to the OH group. In the online Fig. 32 we have collected a number of examples of typical line profiles of CH_3OH, with different upper state energies and A-coefficients. The rarer isotopologue $^{13}CH_3OH$ is seen with 23 lines, of which two are vibrationally excited. Three typical line profiles are shown in the online Fig. 30.

The CH_3OH lines show evidence of two velocity components. One narrow, likely from the CR, with a line width of ∼3−4 km s^{-1}, and average velocity ∼8 km s^{-1}. The other broader component with a probable origin in the HC has a line width of ∼6−10 km s^{-1}, and average velocity ∼7 km s^{-1} (see an example of a two-component Gaussian fit in Fig. 9). This is consistent with the findings of Menten et al. (1988), S95, C05, and also of Beuther et al. (2005) who locate the methanol emission to the HC as well as the CR in their SMA aperture synthesis maps. According to recent CRYRING storage ring measurements (Geppert et al. 2005; Millar 2005) the dissociative recombination of a parent ion $CH_3OH_2^+ + e^- \rightarrow CH_3OH + H$ is so slow that gas-phase formation of methanol is unable to explain the abundance of this molecule, even in dark clouds where it is rare. Instead we have to rely on efficient hydrogenation reactions on grain surfaces, and subsequent release of the methanol into gas-phase. In this scenario the presence of very large amounts of CH_3OH in the compact, heated CR and HC sources is indeed expected.

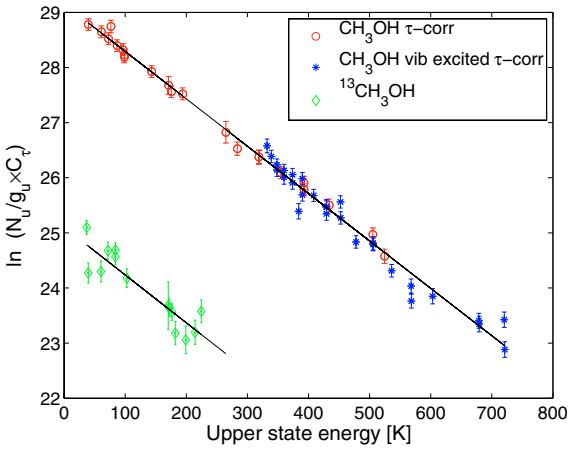

Fig. 10. CH_3OH opacity corrected rotation diagram producing T_{ROT} = 116 K (extended source). The opacity is calculated with varying source-sizes with energy. The $^{13}CH_3OH$ rotation diagram gives a temperature of 115 K.

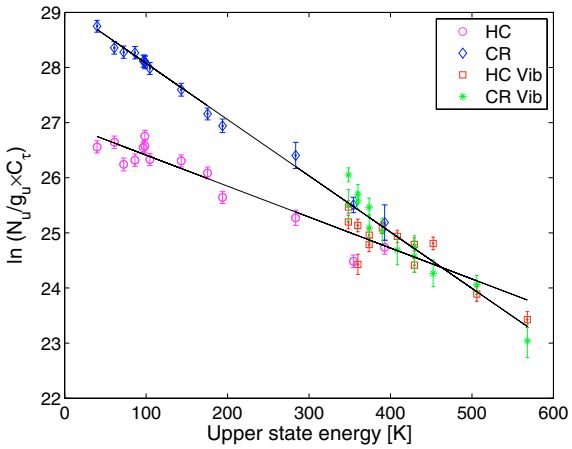

Fig. 11. Two component CH_3OH opacity corrected rotation diagram producing T_{ROT} = 178 K and 98 K for the HC and CR, respectively (extended source). The opacity is calculated with the same parameters together with varying source-size with energy.

The isotopologue $^{13}CH_3OH$ show only evidence of the narrow component, which can be well fitted by a single Gaussian with $\Delta v \approx 3$ km s^{-1} at $v_{LSR} \approx 8$ km s^{-1}. This is also consistent with Menten et al. (1988) and Beuther et al. (2005). The slight broadening of the CH_3OH narrow components compared with that of $^{13}CH_3OH$ might be caused by optical depth broadening. The $^{13}CH_3OH$ from the HC is expected to be well below our detection limit. There are 14 $^{13}CH_3OH$ lines free from blends with an upper state energy range between 37–225 K, which are used in a rotation diagram (Fig. 10). No corrections for optical depths are needed since the $^{13}CH_3OH$ transitions are optically thin. The rotation temperature is found to be 115 ± 16 K, and the column density $(5.9 \pm 1.5) \times 10^{16}$ cm^{-2}.

If we exclude blended and very weak lines we have 50 CH_3OH lines with an upper state energy range from 40 to 721 K. The large number of lines and the wide temperature range make methanol well suited to be used in a rotational diagram. However, one difficulty that may occur with this method is that the optical depths may vary considerably between the CH_3OH transitions. In the rotation diagram seen in Fig. 44 (online material) the lines are plotted (using the total integrated intensity) without any attempt to correct for optical depth or beam-dilution. As can be seen there is a large scatter of the CH_3OH lines. Three transitions with upper state energies of 77, 171 and 265 K lie clearly very high above the others due to their low transition probability and low opacity. A separate fit of these three lines is made and the resulting beam-filling corrected column density becomes $(2.6 \pm 0.4) \times 10^{18}$ cm^{-2}. This is about 3 times higher than the resulting column density from all the lines, $(9.3 \pm 1.1) \times 10^{17}$ cm^{-2}. This indicates that opacity correction needs to be included in the rotation diagram.

Using the forward model, which includes opacity and beam-filling correction (see Fig. 45 in the online material), we find a column density of $(1.3 \pm 0.1) \times 10^{18}$ cm^{-2} in a source size of 6″. (This size is used as beam-filling correction in all calculations of the column densities above.) The scatter in the rotation diagram is reduced and approaches the column density obtained from the three (assumed) optically thin lines. However, since this method has a tendency to underestimate the column density we proceed with opacity correction of the traditional rotation diagram. We note that most of the low energy lines seem to be optically thick (opacities between ~1–6) and most of the high energy lines seem to be optically thin (opacities between ~0.3–1.5). The rotation temperature would be too high if not opacity corrected.

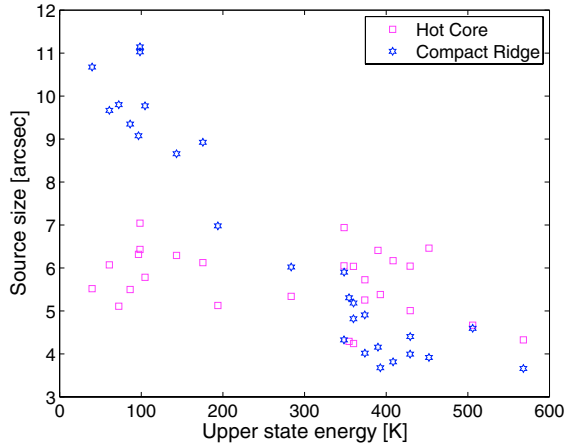

Fig. 12. Source size variation with energy for the CR and HC components of CH_3OH (opacity-corrected with $N_{CR} = 1.7 \times 10^{18}$ cm^{-2}, T_{CR} = 120 K and $N_{HC} = 7.9 \times 10^{17}$ cm^{-2}, T_{HC} = 200 K).

An additional complication is that the extent of the emitting regions may be different for lines of different energy (cf. Menten et al. 1986). This is affecting our estimation of the opacity since we need a total column density (corrected for beam-filling) in the calculations. The online Fig. 46 shows that the source size of the low-energy lines varies between 5–12″, whereas the size of the high-energy lines is almost constant (about 6″), based on Eq. (14) at T_{ROT} = 120 K.

In Fig. 10 we show the opacity corrected rotation diagram. The opacity is calculated using the column density obtained from the three optically thin lines corrected for different beam-fillings for each transition, and the same excitation temperature for all lines (120 K). The scatter in the plot is even more reduced than in the forward model and the resulting column density becomes $(3.4 \pm 0.2) \times 10^{18}$ cm^{-2}. This is much higher than in our comparison surveys, but consistent with Johansson et al. (1984), Menten et al. (1986), and S01 using the $^{13}CH_3OH$ column density (all corrected for our source size).

The rotation temperature is 116 ± 2 K with opacity correction which is the same as produced by the $^{13}CH_3OH$ rotation diagram (115 ± 16 K) and the optically thin fit (120 ± 10 K).

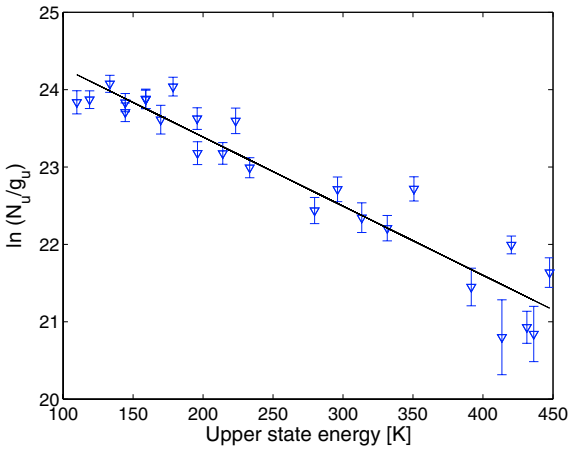

Fig. 13. Rotation diagram for $(CH_3)_2O$ producing T_{ROT} = 112 K (extended source).

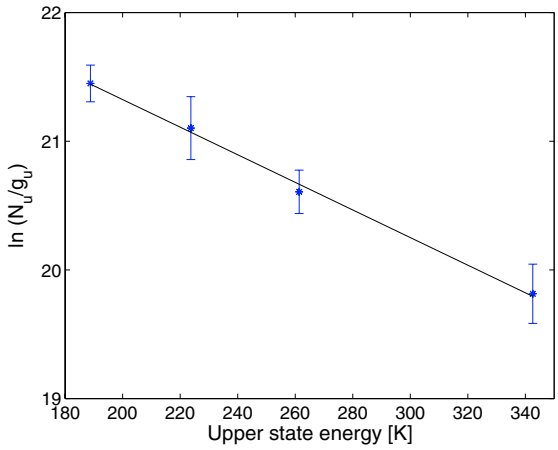

Fig. 14. Rotation diagram for H_2CS producing T_{ROT} = 93 K (extended source).

The forward model produces a slightly higher temperature (136 ± 4 K), which suggests that the opacity correction is too low with this method.

There is also a possibility that the high- and low energy lines are emitted from different regions even though our rotation diagram does not indicate a change of rotation temperature. Using the Gaussian decomposition of the 27 strongest lines, we note that the integrated intensity of the low energy lines is dominated by the narrow CR component, and the high energy lines by the broad HC emission.

When calculating the opacity of the components we again take into account the varying source size with energy. However, Fig. 12 shows that the pronounced variation in size is only true for the narrow component. The broad component seems to have approximately the same size as the energy increases. This again supports the scenario in which the narrow component arises in the CR, which is denser and hotter in the central parts. Hence only the central parts have the ability to emit the high energy lines. The broad component keeps the small size across the transition energy range, supporting an origin in the HC. This source is small and hot and thus can emit all transitions throughout the whole region. The opacity of the CR component is found to be higher than in the HC component which is about 1 or less.

Plotting the components in a opacity corrected rotation diagram (Fig. 11), produces column densities and rotation temperatures for each region: $N_{ROT} = (2.4 \pm 0.2) \times 10^{18}$ cm^{-2}, T_{ROT} = 98 ± 2 K and $(7.9 \pm 1.0) \times 10^{17}$ cm^{-2}, T_{ROT} = 178 ± 11 K for the CR and HC, respectively. Both column densities are much higher than in our comparison surveys, but agrees well with S95 (corrected for our source size). The calculated temperatures are lower than in the comparison surveys, but the high apparent rotation temperatures may be caused by high opacity. Hollis et al. (1983) found that the ground-state transitions originate in a 90 K region, while the torsionally excited transitions come from a 200 K region.

The isotopic ratio of $^{12}C/^{13}C$ can be estimated from the ratio of the optically thin CH_3OH and $^{13}CH_3OH$ column densities, and is found to be 57 ± 14. This is consistent with previous estimates (Table 6).

4.5. Compact Ridge molecules

4.5.1. Dimethyl ether ($(CH_3)_2O$)

This molecule is affected by two internal rotors which are the origin of the fine structure lines of the AA, AE, EE and EA symmetries (Groner et al. 1998). The emission only shows characteristics of the CR with narrow widths of 3−4 km s^{-1} at υ_{LSR} velocities of ∼6−8 km s^{-1}.

Since we cannot resolve these fine structure transitions, we treat them as one single line. The statistical weights and the partition function are changed accordingly. We observe 47 quartets out of which 37 are free from blends and hence can be used in the rotation diagram shown in Fig. 13. The resulting beam-filling corrected column density is $(1.3 \pm 0.3) \times 10^{17}$ cm^{-2} and the rotation temperature is 112 ± 8 K, which is higher than in the comparison line surveys (Table 1). The adopted source size is the same as obtained for CH_3OH, since these molecules most likely have a rather similar origin in the CR. This is also verified when calculating the source size with Eq. (14), assuming an opacity larger than unity. For a temperature of 112 K we find a CR size of 5−6″. This is also indicating optically thick lines which could increase the column density even further.

4.5.2. Thio-formaldehyde (H_2CS)

Five transitions of the CR-emitting H_2CS are observed, of which the $16_{3,13}-15_{3,12}$ transition is a blend with a U-line. The line profile of the $14_{1,13}-13_{1,12}$ transition is shown in Fig. 33 (online material). The four lines with no blends are used in the rotation diagram shown in Fig. 14, producing a rotation temperature, very similar to that of CH_3OH, T_{ROT} = (93 ± 4) K. The resulting beam-filling corrected column density is $(1.3 \pm 0.2) \times 10^{15}$ cm^{-2}, with a source size of 14″ guided by our calculations for the H_2CO optically thick CR emission (see Sect. 4.6.1).

A comparison of the H_2CS and the optically thin $H_2^{13}CO$ results in a molecular abundance ratio of $H_2CO/H_2CS \sim 15$. This is lower than the quoted [O/S] ratio of 35 (online Table 6) from Grevesse et al. (1996). From the comparison of H_2O and H_2S in Sect. 6 we obtain a similar value of ∼20.

4.5.3. Thioformyl cation (HCS^+)

The thioformyl cation previously has not been seen either by W03 nor S01, and here we only observe the J = 13−12 transition as a visible blend with ^{33}SO. Due to the blend we cannot analyse this transition further, but this emission is most likely emitted in the same small hot and dense CR source as CH_3OH and $(CH_3)_2O$.

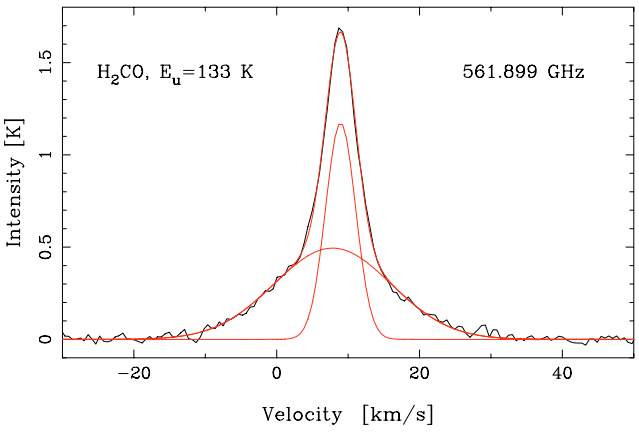

Fig. 15. The H_2CO $8_{1,8}$–$7_{1,7}$ transition with a two-component Gaussian fit shown together with the individual Gaussians. The line widths are 5 km s^{-1} and 19 km s^{-1} from the CR and LVF, respectively.

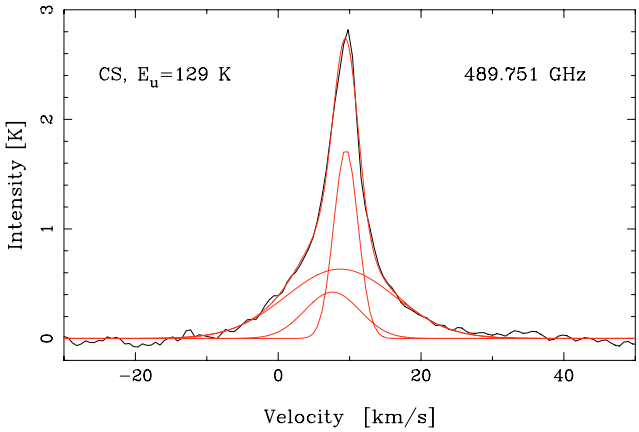

Fig. 16. The CS J = 10–9 transition with a three-component Gaussian fit shown together with the individual Gaussians. The line widths are 4 km s^{-1}, 9 km s^{-1}, and 18 km s^{-1} from the CR/ER, the HC and LVF, respectively.

4.6. Outflow and Compact Ridge molecule

4.6.1. Formaldehyde (H_2CO/$H_2^{13}CO$/HDCO)

We detect three transitions from each of H_2CO and HDCO, and one transition from $H_2^{13}CO$. Since the energy range is small (106–133 K), no rotation diagram can be made. The $8_{1,8}$–$7_{1,7}$ transition of H_2CO is shown in Fig. 33 (online material), together with the same transition of $H_2^{13}CO$ and the $9_{1,9}$–$8_{1,8}$ transition of HDCO. The H_2CO $8_{0,8}$–$7_{0,7}$ transition shows a blend with Hot Core NS at 576.720 GHz. The $8_{1,7}$–$7_{1,6}$ transition of $H_2C^{18}O$ is tentatively found at 571.477 GHz.

The H_2CO lines show two velocity components. Figure 15 shows a two-component Gaussian fit. The narrow component from the CR has widths of ∼5 km s^{-1} at υ_{LSR} ∼ 8.5 km s^{-1}, and the broader component from the LVF has widths of ∼19 km s^{-1} at υ_{LSR} ∼ 8 km s^{-1}. $H_2^{13}CO$ and HDCO show only emission from the CR with similar widths and LSR velocities as for the narrow H_2CO component. Comparison of the CR component of the H_2CO $8_{1,8}$–$7_{1,7}$ transition with the same $H_2^{13}CO$ transition, results in optical depths of ∼6.6 and ∼0.1, respectively (using [^{12}C/^{13}C] = 60).

Since the CR component is optically thick in H_2CO, this source size is calculated with Eq. (14) and is found to be as large as 14″ for a temperature of 115 K, in agreement with Mangum et al. (1990). The LVF source size becomes 10″, which might be caused by a low opacity. Hence a LVF size of 15″ is used for beam-filling correction. The resulting CR and LVF column densities are 3.0×10^{15} cm^{-2} and 4.3×10^{15} cm^{-2}, respectively. With the use of the optically thin $H_2^{13}CO$ the CR column density increases to 2.0×10^{16} cm^{-2}, in agreement with Turner (1990), Mangum et al. (1990), and S95.

Since H_2CO is optically thick we cannot calculate the [^{12}C/^{13}C] elemental ratio. But with the use of the optically thin $H_2^{13}CO$ and HDCO, the abundance ratio of D/H is estimated to ∼0.01, which implies a high deuterium fractionation in the CR. Turner (1990) derived a ratio of HDCO/H_2CO = $0.14^{+0.12}_{-0.07}$ and D_2CO/HDCO = $2.1^{+1.2}_{-0.5} \times 10^{-2}$ for the CR. These large abundance ratios were interpreted as a result of active grain surface chemistry.

4.7. Outflow, Hot Core and Compact/Extended Ridge molecules

4.7.1. Carbon monosulfide (CS/^{13}CS)

Figure 16 shows a three-component Gaussian fit to the observed J = 10–9 transition of CS. Emission is seen from a narrow component, the HC and the LVF at LSR velocities 9, 7 and 10 km s^{-1} with widths 4, 9 and 18 km s^{-1}, respectively. The narrow component may have an origin either from the ER or the CR, hence the column density is calculated with both alternatives. The CS line is also compared to H_2CS and isotopologues of H_2CO in Fig. 33 (online material).

The ^{13}CS J = 12–11 transition is observed with emission from a narrow (ER or CR) component, but is blended with a $^{34}SO_2$ transition. This makes the Gaussian fit with a width of 5 km s^{-1}, at LSR velocity 7 km s^{-1} approximate. Comparison of peak antenna temperatures of the isotopologues (using a ^{12}C/^{13}C ratio of 60) suggests that the narrow CS component is optically thick (τ ∼ 6–12). The source size of an ER component is calculated with Eq. (14) and is found to be 30″ for at temperature of 60 K. This suggests that either the emission of this component is rather extended and clumpy (see Sect. 8), or has an origin in the CR. For a typical CR temperature of 115 K, we find a size of 20″.

The resulting column densities are listed in Table 1. The column density of the LVF agrees well with B87, S95, S01 and C05, and the HC column also agrees with S95, but is lower than found in C05. The narrow component from either the CR och ER is more difficult to compare. Our ER column agrees rather well with B87, but is an order of magnitude lower than found by S95. As CR emission it agrees with S95. The differences may arise due to opacity, beam-sizes and energy levels.

4.7.2. Hydrogen isocyanide (HNC)

Figure 17 shows a four-component Gaussian fit of the HNC J = 6–5 transition with an upper state energy of 91 K, and a U-line seen in the red-ward LVF line wing at a velocity of 22 km s^{-1}. As for CS, three velocity components, from the ER, HC, and LVF, are clearly seen at υ_{LSR} = 9, 6 and 7 with widths of 4, 9 and 27 km s^{-1}, respectively. The sizes and temperatures for the subregions are taken to be representative of typical values

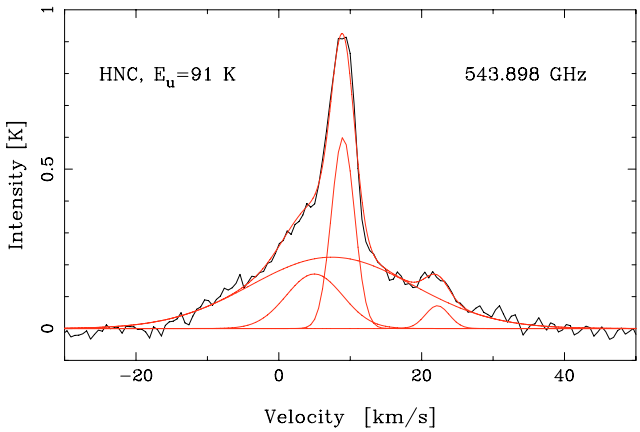

Fig. 17. The HNC J = 6−5 transition and a U-line at 543.873 GHz with a four-component Gaussian fit shown together with the individual Gaussians. The line widths are 4 km s^{-1} for the U-line, 4 km s^{-1}, 9 km s^{-1}, and 27 km s^{-1} for the HNC ER, HC and outflow components, respectively.

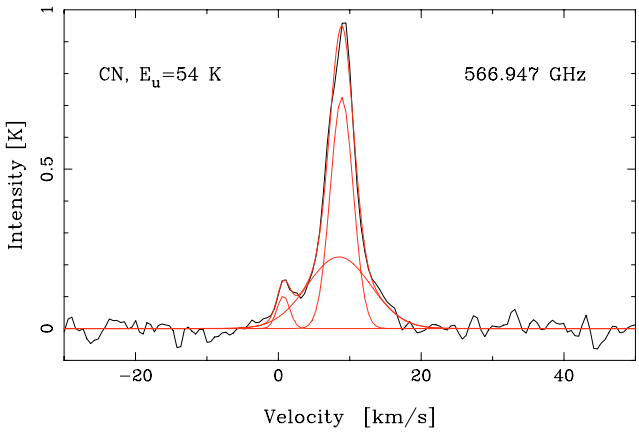

Fig. 18. CN with a three-component Gaussian fit of five unresolved hyperfine-structure lines shown together with the individual Gaussians. The widths are 4 km s^{-1} and 11 km s^{-1} for the PDR/ER and HC components of the three strong hyperfine-structure lines, respectively, and 2 km s^{-1} for the weak transitions at a velocity of 0 km s^{-1}.

(see Table 1). The HNC line is also shown in Fig. 31 (online material).

4.8. PDR/Extended Ridge and Hot Core molecule

4.8.1. The cyanide radical (CN)

The main CN emission has its origin in the PDR/ER region and the HC (Rodríguez-Franco et al. 1998) at $\upsilon_{\rm LSR}$ ∼ 9 and 8.5 km s^{-1} with widths of ∼4 and ∼10 km s^{-1}, respectively. In total we have observed three lines with 8 non-resolved hyperfine structure features. Figure 31 (online material) shows one of the N = 5−4 transitions, consisting of three non-resolved hyperfine structure lines, with two additional ones in the line wing at a velocity of 1 km s^{-1}. The same transitions are shown in Fig. 18 with a three-Gaussian fit of the five transitions. No rotation diagram is made since the upper state energy of 54 K is the same for all transitions.

Using Gaussian fits, the LTE approximation and typical temperatures and source sizes, the column densities for the HC and PDR/ER regions are estimated to be 7.9×10^{15} cm^{-2}, and 4.9×10^{13} cm^{-2} for the HC and PDR/ER, respectively. Our comparison surveys have no observations of CN, but Rodríguez-Franco et al. (2001) obtained column densities by CN mapping, ranging from 10^{13} cm^{-2} in the Trapezium region to 10^{14}−10^{15} cm^{-2} in the Ridge region. S95 find $N = 1 \times 10^{15}$ cm^{-2} with a 14″ beam, and B87 also find the same CN column density with a 30″ beam.

4.9. Extended Ridge molecule

4.9.1. Diazenylium (N_2H^+)

The diazenylium transition J = 6−5 is shown in Fig. 31 (online material). The width of ∼5 km s^{-1} at $\upsilon_{\rm LSR} \approx 9$ km s^{-1} indicates an ER origin of the emission, in agreement with mapping of the J = 1−0 transitions by Womack et al. (1990) and Ungerechts et al. (1997). The column density of 1.0×10^{12} cm^{-2}, that we calculate using the simple LTE approximation, is much lower than that found by Ungerechts et al. (1997), 8.4×10^{12} cm^{-2}.

4.10. Unidentified line features

We observe 64 unidentified line features. Tentative assignments have been given to 26 lines, such as the first tentative detections of ND, and of the anion SH^- (see Fig. 34, Tables 34, and 35 in the online material and Table 3 in Paper I). There are 28 U-lines, i.e. clearly detected lines, and 36 T-lines, which means that they are only marginally visible against the noise or in a blend. The tentative assignments also include the species SO^+, CH_3CHO, CH_3OCHO, SiS, HNCO, $H_2C^{18}O$, and a high energy HDO line. For details see Paper I.

The strongest U-line is found at 542.945 GHz with a peak intensity of 140 mK. The line appears to show emission from two components, probably the CR and the HC (see Fig. 34 in the online material).

5. Carbon monoxide (CO/^{13}CO/C^{17}O/C^{18}O), carbon (C) and H_2 column densities

We have observed the J = 5−4 transition of CO, ^{13}CO, C^{17}O, and C^{18}O (Fig. 26). The CO line is the most intense single line in our 42 GHz wide band. The FWZP (Full Width Zero Power) of CO is approximately 230 km s^{-1}, as compared to 120 km s^{-1} reported in Wirström et al. (2006, hereafter W06), a result of our much lower noise level. Since W06 also used Odin but with another observation mode, we can again demonstrate the high accuracy of the Odin calibration with a comparison of the amplitudes, which agree within less than five percent.

As pointed out in W06 it is clear that CO J = 5−4 has emission from at least three different components – LVF, HVF and a narrow component. The high brightness temperature of the last component suggests that this emission originates in the extended and warm PDR, whereas the narrow components from the optically thin isotopologues have approximately equal emission from the PDR and the colder ER gas behind it. We observe all three components in the CO and ^{13}CO emission, but only the narrow ER/PDR component and the LVF for the C^{17}O and C^{18}O isotopologues (W06). The Gaussian components are given in Tables 8 and 32 in the online material, and agree well with W06, especially when our higher signal-to-noise ratio is taken into account, which enables us to see line wings that were previously unobserved.

A summary of the resulting column densities, estimated optical depths, used source sizes and temperatures is found in Table 2, and also in more detail in the online Table 8. Here also column densities calculated from all isotopologues are given together with the parameters of the Gaussian fits. Note that the column density for the CO narrow component (calculated from $C^{17}O$) is lowered by a factor of two, since this component only has emission from the PDR, while the isotopologues have approximately equal emission from both the PDR and ER. For detailed arguments see W06.

The only observed atomic species in this survey is the $^3P_1$–$^3P_0$ transition of C at 492.1607 GHz. It shows a narrow line profile from an extended emission with a width of 4.5 km s^{-1}, at LSR velocity ∼9 km s^{-1}. Due to the loss of orbits during this observation, the noise level here is 200 mK, as compared to our average level of 25 mK in the rest of the spectral survey. This makes it impossible to distinguish a possible broad emission in this transition. Our beam-averaged column density of C is 5.6×10^{17} cm^{-2}. Tauber et al. (1995) find a lower limit for a beam-averaged C column density of $\sim 7 \times 10^{17}$ cm^{-2} (beam size 17″) in the Orion bar. Ikeda et al. (1999) find a column density very similar to ours (6.2×10^{17} cm^{-2}) from observations of the 492.1607 GHz transition with the Mount Fuji submillimetre-wave telescope towards the Orion KL position, in a HPBW of 2.′2. The optical depth was estimated to be 0.2. B87 find $N \gtrsim 7.5 \times 10^{17}$ cm^{-2} with a 30″ beam towards the Orion KL region. Plume et al. (2000) presented maps of the same transition, obtained with the SWAS satellite, resulting in an average column density of 2×10^{17} cm^{-2}.

When estimating abundances we need comparison column densities of H_2 for each subregion (results also given in Table 2). This is provided by $C^{17}O$ for the PDR/ER and LVF components, using $[CO]/[H_2] = 8 \times 10^{-5}$ (e.g. Wilson & Matteucci 1992), an isotope ratio $[^{18}O]/[^{17}O] = 3.9$ (Table 6), together with $[^{16}O]/[^{18}O] = 330$ (Olofsson 2003). The latter value was found from high S/N $S^{18}O$ observations of molecular cloud cores. This is somewhat lower than the usually quoted value of 560 (Wilson & Rood 1994), valid for the local ISM and estimated from H_2CO surveys in 1981 and 1985. A likely explanation for the lower value is a local enrichment of ^{18}O relative to ^{16}O by the ejecta from massive stars. For the HVF component we use ^{13}CO since $C^{17}O$ has no HVF emission.

The resulting H_2 column density from the LVF is 3.2×10^{23} cm^{-2}. This is close to the limits given by Masson et al. (1987) $(3–10) \times 10^{22}$ cm^{-2}, as well as 1×10^{23} cm^{-2} by Genzel & Stutzki (1989). Wright et al. (2000) find a beam-averaged H_2 column density of 2.8×10^{23} cm^{-2} from observations of the 28.2 μm H_2 0–0 S(0) line for a temperature of 130 K (beam size 20″ × 33″).

Our resulting HVF H_2 column density is 3.9×10^{22} cm^{-2}, in agreement with the Genzel & Stutzki value of 5×10^{22} cm^{-2}. In contrast, Watson et al. (1985) found that the HVF column of warm shock heated H_2 is only 3×10^{21} cm^{-2}, a result based upon their KAO observation of high-J CO lines.

Tauber et al. (1995) reported an average H_2 column density of $\sim 3 \times 10^{22}$ cm^{-2} from the Orion Bar (calculated from ^{13}CO mapping). This is in agreement with our total narrow component, which we find to be 4×10^{22} cm^{-2}. When we calculate the abundances in Sect. 7, we divide this value by two, since there are about equal contributions from the PDR and ER to the $C^{17}O$ emission (W06). Our value is also consistent with the results of Goldsmith et al. (1997) convolved with the 2.′1 Odin beam.

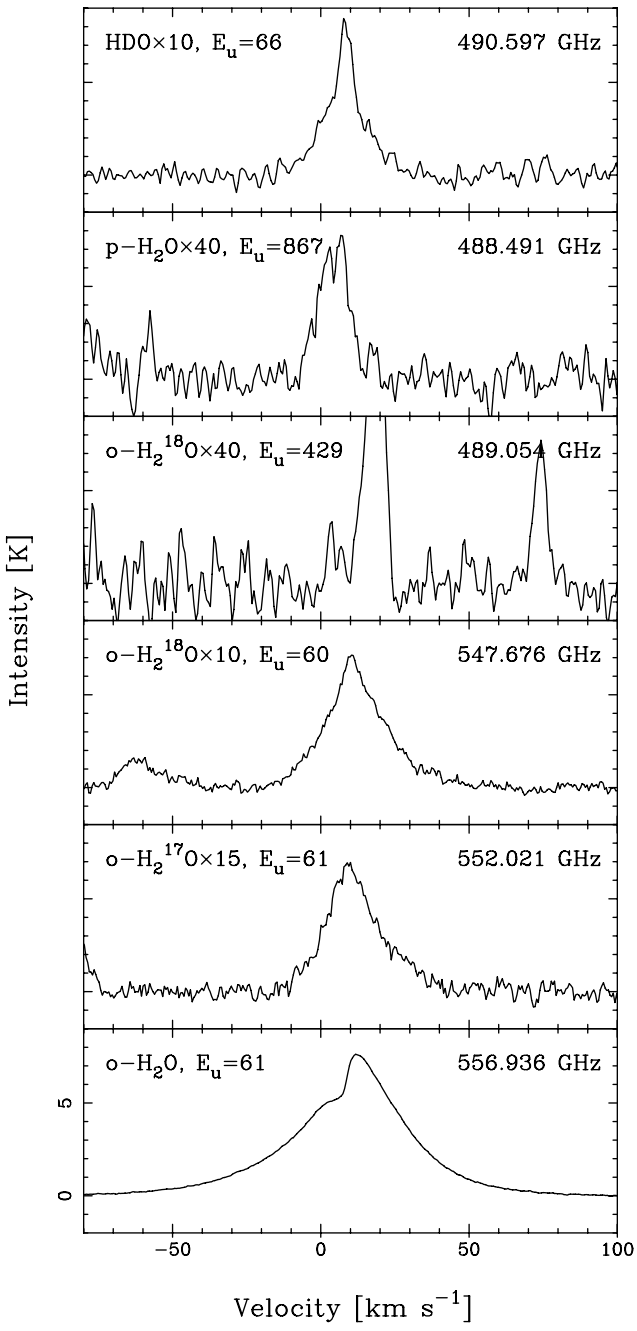

Fig. 19. Water and isotopologues. The o-$H_2^{17}O$ is reconstructed spectra with blending lines subtracted. An intensity scale factor is given after the molecular species.

6. Water (o-$H_2^{16}O$, p-$H_2^{16}O$, o-$H_2^{17}O$, o-$H_2^{18}O$, HDO)

6.1. Correcting the water emission lines for blends

Because of the large number of methanol and sulphur dioxide lines observed, they cause the most common blends in all lines. Since we are particularly interested in water, we attempt to reconstruct the water isotopologues without blends. We use observed transitions in our survey with similar parameters (E_u, A-coefficient and g_u), and scale them with the parameters of the blending lines before removal from the water isotopologue line of interest. The molecular line parameters of the blending transitions are found in the online Tables 9, 10 and 20.

Two lines are blended with the o-$H_2^{18}O$ $1_{1,0}$–$1_{0,1}$ ground state rotational transition. The $^{34}SO_2$ $21_{3,19}$–$20_{2,18}$ transition is blended with the red wing, and in the blue wing there is an overlapping methanol line, $15_{1,15}$–$15_{2,14}$, $v_t = 1$. However, since the simultaneous observations of o-$H_2^{17}O$ show that the $H_2^{18}O$ transition is optically thick even in the line wings (see next section), we do not attempt to remove these blending transitions.

The o-$H_2^{17}O$ ground state rotational transition is, however, optically thin in the line wings, and we therefore remove three blending lines. In Fig. 38 (online material) we show two of the blending lines together with the o-$H_2^{17}O$ line. In the blue o-$H_2^{17}O$ wing the blending SO_2 transition $26_{6,20}$–$26_{5,21}$ is overlapping. In the red wing there are two blends. One from the $6_{6,1}$–$7_{5,3}$ methanol transition shown, and one from the very weak SO_2 $34_{1,33}$–$34_{0,34}$ transition.

6.2. Water analysis

We have observed the $1_{1,0}$–$1_{0,1}$ ground state rotational transition of o-H_2O and its isotopologues o-$H_2^{18}O$ and o-$H_2^{17}O$, which mainly show emission from the Plateau. A very weak feature at 489.054 GHz is tentatively identified as the HC-tracing $4_{2,3}$–$3_{3,0}$ transition of o-$H_2^{18}O$ with an upper state energy of 429 K. The HC-tracing p-H_2O transition $6_{2,4}$–$7_{1,7}$ with an upper state energy of 867 K, is also observed, as well as the $2_{0,2}$–$1_{1,1}$ HDO transition showing emission from the CR, HC and LVF. Figure 19 shows all detected water lines after removal of some blends in $H_2^{17}O$ as discussed in the previous section.

The optical depths, column densities, assumed source sizes and excitation temperatures are found in Table 2, and in more detail in Table 7 (online material), together with the parameters of the Gaussian fits.

Both the o-$H_2^{18}O$ and o-$H_2^{17}O$ ground state rotational transition show features of a weak, narrow component from the CR, a broad stronger component from the LVF, and with HVF emission mainly in the red wing. Figures 35 and 36 (online material) show three-component Gaussian fits to the water isotopologues. The emission from the ER and PDR is considered to be very low since the water mainly will be frozen onto the dust grains at the rather low temperatures in this region.

The o-H_2O line is very optically thick at all velocities as seen in Fig. 39 (online material) which displays the ratio of o-H_2O and o-$H_2^{18}O$. The excitation conditions for these two isotopologues are therefore very different. A similar figure of the ratio of o-$H_2^{18}O$ and o-$H_2^{17}O$ (Fig. 40 in the online material) shows an almost constant ratio of 1.5 for velocities between −10 and +30 km s^{-1}. This demonstrates that the two line profiles are almost identical, and that the o-$H_2^{18}O$ emission is rather optically thick at all velocities since $[^{18}O/^{17}O] = 3.9$. By comparison of column densities from the total integrated intensities, the optical depths for o-$H_2^{17}O$ and o-$H_2^{18}O$, are 0.9 and 3.4, respectively. The small changes of the ratio with velocity as seen in Fig. 40 also are consistent with our decomposition into Gaussian components. The LVF is optically thick in both isotopologues, whereas the HVF and CR have lower optical depths causing increase of the ratio at their emission velocities.

6.2.1. *Ortho*-H_2O from the low- and high velocity flow and the Compact Ridge

The similarity of the line profiles is also illustrated in Fig. 20 showing a comparison of o-$H_2^{17}O$, o-$H_2^{18}O$ and the $19_{3,17}$–$18_{2,16}$ SO_2 transition, all normalised to their respective peak temperature. The remarkable similarity of the line profiles suggests a very similar origin and chemistry of the water isotopologues and SO_2: the LVF and with additional HVF emission mainly in the red wings.

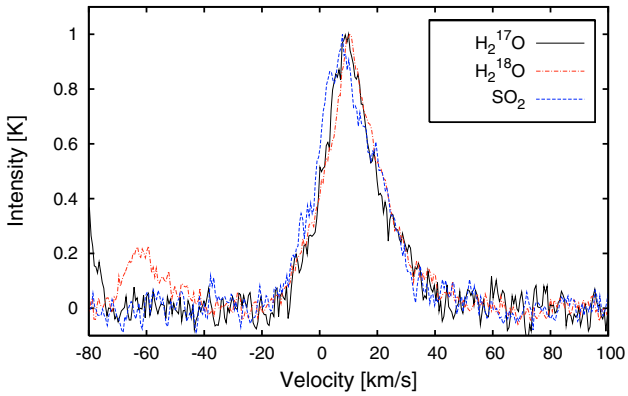

Fig. 20. Comparison of $H_2^{18}O$, with $H_2^{17}O$, and the $19_{3,17}$–$18_{2,16}$ SO_2 transition, all normalised with respective peak temperature. The high degree of similarity of all three line profiles suggests an origin in the same gas and velocity fields, mainly from the LVF with additional emission from HVF in the red wings.

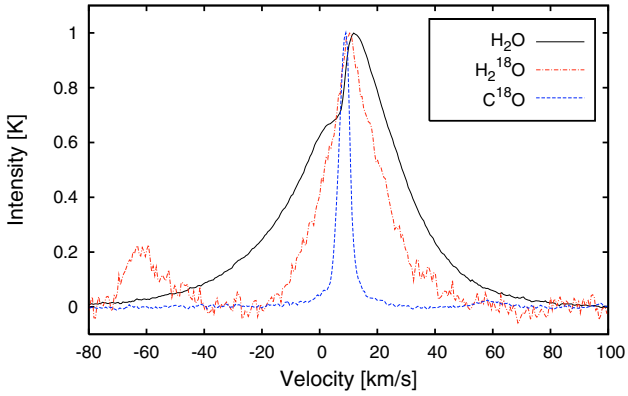

Fig. 21. Comparison of the optically thick self-absorbed o-H_2O with o-$H_2^{18}O$ and $C^{18}O$ $J = 5$–4, all normalised with respective peak intensity. The LVF self-absorption of o-H_2O in the blue wing is seen when compared to o-$H_2^{18}O$, which shows LVF emission in both wings and HVF emission mainly in the red wing.

The resulting column densities (found in Table 2 and in the online Table 7) are calculated with the simple LTE approximation and for an *ortho*/*para* ratio of 3. As a first approximation of the column density we have used the full integrated intensity of the lines, assuming the Plateau to be the main emitting source (with $T_{ex} = 72$ K and a source size of 15″, see below). We have also calculated the column densities for the different subregions using the Gaussian components. In addition, the o-$H_2^{17}O$ and o-$H_2^{18}O$ column densities are calculated with and without optical depth corrections. Since the o-H_2O transition is highly optically thick, we calculate the column density from o-$H_2^{17}O$ and o-$H_2^{18}O$. With isotope ratios of $[^{18}O]/[^{17}O] = 3.9$ and $[^{16}O]/[^{18}O] = 330$ (Table 6), we determine the opacity-corrected column density of H_2O to be 1.7×10^{18} cm^{-2}. The opacity-corrected LVF and HVF column densities, obtained from the Gaussian fits of the isotopologues, are 8.7×10^{17} cm^{-2} and 8.8×10^{17} cm^{-2}, respectively. These calculations assume LVF and HVF source sizes for the isotopologues of 15″ (cf. Olofsson et al. 2003), which is the same extent as the submillimetre HDO emission from the

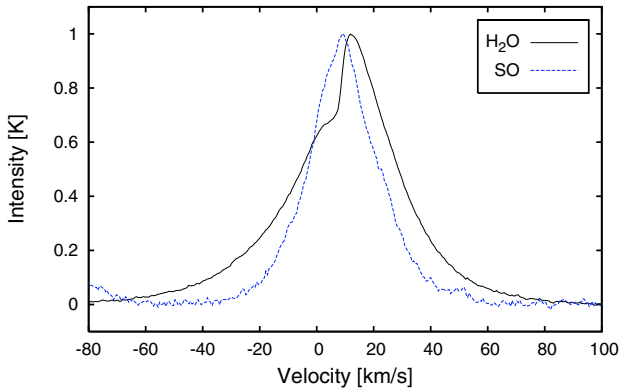

Fig. 22. Comparison of the 13_{13}–12_{12} SO transition and o-H_2O, both normalised with respective peak intensity. Both species show emission from the LVF and the HVF, but the water LVF is self-absorbed in the blue-shifted emission.

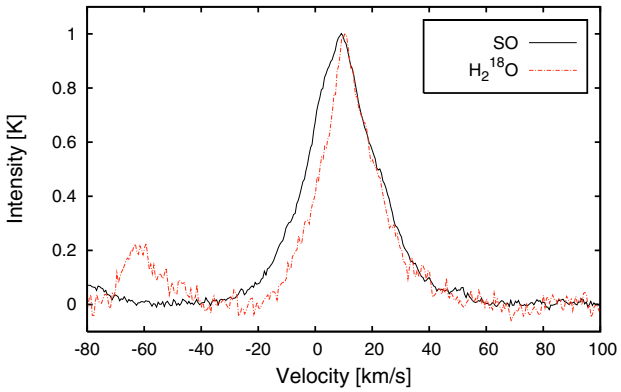

Fig. 23. Comparison of the 13_{13}–12_{12} SO transition, and o-$H_2^{18}O$ normalised with respective peak intensity.

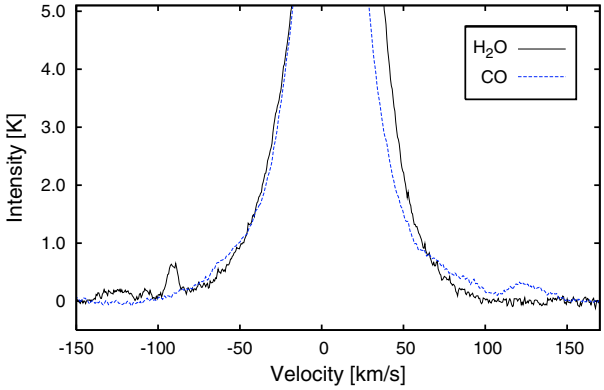

Fig. 24. Comparison of the broad HVF emission in the line wings of CO and o-H_2O scaled 2.5 times. Note the large velocity scale.

LVF mapped by Pardo et al. (2001). As excitation temperature for both LVF and HVF we use 72 K as found by Wright et al. (2000). We also calculate the H_2O HVF column density from the Gaussian fit to H_2O itself, and with opacity-correction (calculated from the isotopologues) almost the same value is obtained as from the isotopologues. The size of the H_2O HVF is assumed to have an extent of 70″ (Olofsson et al. 2003; Hjalmarson et al. 2005).

The opacity-corrected column density for the H_2O CR is 5.6×10^{17} cm^{-2}. For the CR we use the temperature and size obtained from our CH_3OH rotation diagram of 115 K and 6″. This is also consistent with our calculation of the excitation temperature from the optically thick $H_2^{18}O$ CR component, if a source size of 6″ is assumed.

The o-H_2O line has a central asymmetry that suggests strong self-absorption in the blue LVF by lower excitation foreground gas. The steep change in the self-absorption occurs in the velocity range of 2 to 12 km s^{-1}. Figure 21 compares the self-absorbed o-H_2O transition both with o-$H_2^{18}O$, and with the narrow emission from the $C^{18}O$ $J = 5$–4 line, all normalised to their respective peak temperature. The LVF self-absorption of o-H_2O in the blue wing is seen when compared to o-$H_2^{18}O$, which shows LVF emission in both wings, and HVF emission mainly in the red wing. Figure 22 shows a similar comparison between o-H_2O and an optically thick SO transition at 559.320 GHz. Both species display emission from LVF and HVF, although the blue water LVF emission is self-absorbed.

In Fig. 23 we show the same SO 13_{13}–12_{12} transition again, but this time compared to o-$H_2^{18}O$. In the blue wing SO has excess emission as compared to the water emission, whereas the red wings of SO and o-$H_2^{18}O$ are almost identical. This might be caused by shock chemistry in the red HVF which is pushing into the ambient molecular cloud (Genzel & Stutzki 1989), thereby producing a high water abundance. In the blue HVF, which is leaving the molecular cloud, no such shock chemistry seems to be present. The water abundance in this part of the HVF is likely due to evaporation from icy dust grains, which produces less water than shock chemistry. In contradiction to this, the SO emission is symmetric in both wings, suggesting that shock chemistry is not required to produce high SO abundances.

The similarity of the broad HVF emissions from CO and H_2O is shown in Fig. 24. The FWZP of the broad component is ∼230 km s^{-1} for o-$H_2^{16}O$, 50 km s^{-1} for the isotopologues, and 35 km s^{-1} for HDO.

6.2.2. *Para*-H_2O from the Hot Core

In the main o-H_2O $1_{1,0}$–$1_{0,1}$ line spectrum (Fig. 19) possible emission from the HC and CR would be blended with the much stronger and broader component from the LVF. Melnick et al. (2000) concluded that the HC contributes negligibly to the water emission within the SWAS beam, and the CR would contribute less than 5–10%. The highest energy levels in the ISO data presented by Lerate et al. (2006) and Cernicharo et al. (2006) may have a contribution from the HC, but those authors remark that the large far-IR line-plus-continuum opacity probably would hide most of this emission.

However, our detected optically thin p-H_2O $6_{2,4}$–$7_{1,7}$ transition with upper state energy 867 K, clearly reveals the emission from the HC. The width of the line is 12 km s^{-1} at $\upsilon_{\rm LSR}$ ∼ 4.4 km s^{-1}, between velocities −8 and 15 km s^{-1}. When column densities are calculated using the simple LTE approximation, we find values in the range $(3.7–12) \times 10^{18}$ cm^{-2} for a temperature range of 200–500 K and a typical source size of 10″. Since no clear HC emission is seen from the ground rotational state transition in $H_2^{17}O$, either the temperature in the HC is high enough to result in the negligible emission of this transition from the HC, or the $H_2^{17}O$ transition has an optically thick LVF emission which is blocking possible HC emission. If the temperature is 500 K, the emission from the HC would only be about 10% of the total (if no optical depths are taken into account), and therefore would be hidden in the stronger and broader LVF emission even if $H_2^{17}O$ is optically thin. However, if the temperature in the HC is about 200 K, the $H_2^{17}O$ LVF emission has to have an optical depth larger than unity. Since our estimated value is about

1.5, this is consistent with a HC temperature of 200 K and a column density of HC H_2O 1.2×10^{19} cm^{-2}. This is in agreement with the only previous observation of H_2O emission from the HC made by S01. They detected the vibrationally excited $1_{1,0}-1_{0,1}$ $v_2 = 1$ transition and found a HC column density of 3×10^{19} cm^{-2} with a temperature of 200 K and a water abundance of 1×10^{-5}. Gensheimer et al. (1996) estimated the HC $H_2^{18}O$ column density to be 2.7×10^{16} cm^{-2} from $H_2^{18}O$ mapping of the quasi-thermal $3_{1,3}-2_{2,0}$ transition with the IRAM telescope (12″ beam). This column density translates to 1.3×10^{19} cm^{-2} for H_2O (corrected for source size and isotopologue ratio differences), in excellent agreement with our result, even though their observations suffered from severe blends. Their HC water mapping also showed that the emission from both $H_2^{18}O$ and HDO were unresolved by their beam, and the HDO mapping showed sizes of 6–8″.

Our tentative detection of the optically thin HC emitting o-$H_2^{18}O$ $4_{2,3}-3_{3,0}$ transition, with an upper state energy of 430 K, results in a HC H_2O column density of about 4×10^{19} cm^{-2}.

6.2.3. Comparisons of outflow column densities

Our column density results for the Plateau agrees excellently with those of Wright et al. (2000), who observed 19 pure rotational lines in absorption using the Short Wavelength Spectrometer (SWS) on board the Infrared Space Observatory (ISO), with a beam size of 14″ × 20″ to 20″ × 30″. Their rotation diagram, including a generalised curve-of-growth method, results in a rotation temperature of 72 K, and a beam-averaged column density (from the total emission) of 1.5×10^{18} cm^{-2}. They also conclude that the observed water arises from an outflow centred near IRc2.

Lerate et al. (2006) observed more than 70 far-IR pure rotational $H_2^{16}O$ lines, and 5 $H_2^{18}O$ lines, with the ISO LWS (Long Wavelength Spectrometer) between ~43 and 197 μm (beam size about 80″). Their rotation diagram of the total emission from $H_2^{18}O$ results in a beam-averaged column density of $(2-5) \times 10^{14}$ cm^{-2}, and a rotation temperature of 60 K. For a 15″ outflow source, their result translates to $(1.8-4.7) \times 10^{18}$ cm^{-2} for $H_2^{16}O$, also in good agreement with our value. In the analysis by Cernicharo et al. (2006) of this data set, they concluded that most of the water emission and absorption arises from an extended flow of gas with velocity 25 ± 5 km s^{-1}, with an inferred kinetic gas temperature of 80–100 K.

6.2.4. HDO from the Compact Ridge, low velocity flow and the Hot Core

The deuterated species HDO is observed in the $2_{0,2}-1_{1,1}$ transition with $E_u = 66$ K, and shows evidence of CR, LVF, and also HC emission as is observed by W03. Figure 37 shows a three-component Gaussian fit. Pardo et al. (2001) reported detections of the $2_{1,2}-1_{1,1}$ and $1_{1,1}-1_{0,0}$ lines in the 850–900 GHz spectral region, which seem to trace the Plateau gas and not the HC. Their conclusion is that the HC component is hidden behind the optically thick HDO LVF in their transitions, which is supporting our analysis of the non-detection of HC emission in the ground state rotational water transitions.

A T-line at 559.816 GHz tentatively is identified as the high energy (580 K) HDO transition $6_{2,4}-6_{2,5}$.

Our estimated column density of HDO, assuming that the main emission originates in the outflows, is 9.1×10^{15} cm^{-2}, which is about the same value as reported by Lerate et al. (2006), 8.5×10^{15} cm^{-2} (corrected for source size). The column density reported by Pardo et al. (2001) is higher, 5×10^{16} cm^{-2}, calculated from an LVG model with a source size of 15″, and opacities of 3.7 and 6.7 for their two lines.

We also calculate the column densities for the CR, LVF and HC separately, which are found to be 1.8×10^{16} cm^{-2}, 4.5×10^{15} cm^{-2}, and 1.5×10^{16} cm^{-2}, respectively. With correction for source-size, this is 2–4 times lower than found in Olofsson (1984) by mapping the $1_{1,0}-1_{1,1}$ transition with a 47″ beam (at Onsala Space Observatory); 3×10^{16} cm^{-2}, 1×10^{16} cm^{-2}, and 7×10^{16} cm^{-2}, respectively.

6.2.5. Molecular abundance ratios

The [D/H] ratio calculated from from HDO/H_2O is 0.005, 0.001 and 0.03 in the LVF, HC, and CR, respectively (Table 6). The CR ratio may be compared to the HDCO/$H_2^{13}CO$ ratio from which we obtain a similar [D/H] value of 0.01 (see Sect. 4.6.1). Lerate et al. (2006) found [D/H] values in the range 0.004–0.01.

The column densities for H_2O and H_2S from the LVF are also used to estimate the molecular abundance ratio of O/S to ~20 (Table 6). Using the $H_2CS/H_2^{13}CO$ ratio we obtain a similar value of ~15 (see Sect. 4.5.2).

7. Molecular abundance estimates

7.1. Gas-phase abundances from the Odin spectral line survey

Our estimated abundances for each subregion are summarised in Table 3, together with comparison abundances mostly from B87 and S95. We find very high gas-phase abundances of H_2O, NH_3, SO_2, SO, NO, and CH_3OH. Note that both our LVF and HC abundances are source averages. S95 use beam-averaged abundances (with a HPBW of 14″), and B87 use a HC size of 10″ and a Plateau size of 20″, while we separate the LVF and HVF emissions with a slightly smaller size for the LVF (15″). The beam-averaged CR abundances in both B87 and S95 are corrected to our source-sizes to allow an easier comparison.

A large source of uncertainty in these calculations is the adopted H_2 column densities. Whenever possible we have used our own calculated H_2 column densities (for the ER, LVF, HVF, Table 2). For the HC and CR we have adopted $N(H_2) = 1 \times 10^{24}$ cm^{-2} (calculated for a HC size of 10″ in B87), and $N(H_2) = 2 \times 10^{23}$ cm^{-2} (Wilson et al. 1986; B87; Goldsmith et al. 1997), respectively. In case of the HVF we also compare the (shocked) water column with the column density of the hot (shocked) H_2, where $N_{HVF} = 3 \times 10^{21}$ cm^{-2} (Watson et al. 1985). When we calculate the abundances we assume that the derived H_2 column density spatially coincides with the emission from the species of interest.

Most of our abundances, listed in Table 3, are in very good agreement with B87 and S95. However, there are a few exceptions – a 4–15 times higher abundance for SO_2 in the LVF, and 2–5 times higher abundances in general in the CR than in B87 and S95. The differences may arise because our observed transitions probe higher density and more compact regions in the CR. Since we cannot discriminate between CR or ER emission for CS, the abundance is calculated with both alternatives. It turns out that the CS abundance is about the same for either source of emission. However, the high ER abundance of CS compared to that of B87 is to a large extent due to the very different H_2 column densities used in our survey

Table 3. Derived abundances and comparisons.

Region	Species	X[g] [$\times 10^7$]	B87 X[h] [$\times 10^7$]	S95 X[i] [$\times 10^7$]
LVF[a]	H_2O	29		
	HDO	0.15	0.17	
	SO_2	20	5.2	1.3
	SO	3.1	5.2	2
	SiO	0.11	0.28	0.08
	H_2S	1.5	0.98	
	H_2CO	0.14	0.31	1.1
	CS	0.12	0.22	0.04
	HNC	0.012		
HVF	H_2O/Total H_2[b]	220	200–300[j]	
	H_2O/Hot H_2[c]	2900	2000–5000[k]	
	SO_2	225		
	SO	21		
	SiO	0.45		
HC[d]	H_2O	120	140[l]	
	HDO	0.15	0.5	0.14
	H_2S	0.27	0.3[m]	
	CH_3CN	0.05	0.078	0.04
	NH_3	16	10[n]	
	HC_3N	0.018	0.016	0.018
	OCS	0.17		1.1
	CH_3OH	7.9[o]	1-10[p]	1.4
	HNC	0.0044		
	CS	0.029		0.06
	CN	0.079		0.008
	NO	2.8	2.0[m]	
CR[e]	H_2O	28		
	HDO	0.87		0.93
	NH_3	2.0		
	CH_3OH	120[o]	30	22
	$(CH_3)_2O$	6.5	2.5	1.0
	H_2CO	1.0	0.6	0.46
	HDCO	0.014		
	H_2CS	0.065	0.06	0.014
	SO_2	10		
	SO	0.85		
	CS as CR	0.40		0.1
ER[f]	CS as ER	0.21	0.025	0.11
	HNC	0.001	0.005	
	N_2H^+	0.0005		
PDR[f]	H_2O	$\gtrsim$1.1[q]	0.33[r]	
	CN	0.02	0.03	
	NH_3	0.05[s]		

[a] LVF $N(H_2) = 3 \times 10^{23}$ cm^{-2} (this work). [b] HVF total $N(H_2) = 4 \times 10^{22}$ cm^{-2} (this work). [c] HVF hot $N(H_2) = 3 \times 10^{21}$ cm^{-2} (Watson et al. 1985). [d] HC $N(H_2) = 1 \times 10^{24}$ cm^{-2} (B87). [e] CR $N(H_2) = 2 \times 10^{23}$ cm^{-2} (Wilson et al. 1986; Goldsmith et al. 1997). [f] For both the ER and PDR: $N(H_2) = 2.0 \times 10^{22}$ cm^{-2} (this work, see Sect. 5). [g] Source averages with sizes given in Tables 1 and 2. [h] Source averages from Blake et al. (1987). [i] Source averages from Sutton et al. (1995). [j] Plateau abundance (both LVF and HVF), Cernicharo et al. (2006). [k] Wright et al. (1996). [l] Gensheimer et al. (1996). [m] C05. [n] Hermsen et al. (1988a). [o] Estimated from the CH_3OH two-component rotation diagram. [p] Menten et al. (1988). [q] W06. [r] Melnick et al. (2000). [s] Larsson et al. (2003) towards the Orion Bar.

and B87, $N(H_2) = 2 \times 10^{22}$ cm^{-2} and $N(H_2) = 3 \times 10^{23}$ cm^{-2}, respectively.

Our HVF H_2O abundance, as compared to the total H_2 density in the flow, is 3×10^{-5}, in agreement with the water abundance in the Plateau estimated by Cernicharo et al. (2006). If we compare the HVF water abundance to the hot shocked H_2 it is consistent with Wright et al. (2000) and Melnick et al. (2000), who estimate the shocked Plateau water abundance to be $(2-5) \times 10^{-4}$.

The HC H_2O abundance is in agreement with the mapping of $H_2^{18}O$ towards the Orion Hot Core with the IRAM telescope (12″ beam) by Gensheimer et al. (1996). Their estimated abundance is 1.4×10^{-5}. S01 estimate the water abundance to be $\sim 1.0 \times 10^{-5}$ from their observation of the vibrationally excited H_2O $1_{1,0}-1_{0,1}$ $v_2 = 1$ transition, also in accordance with our value.

High water abundances in high temperature regions, for example in outflows, PDRs, and hot cores are consistent with both water and deuterated water forming on grains at low temperatures, and subsequently evaporating from the grain surfaces at high temperatures above ~90 K. At temperatures above ~400 K, easily reached in shocks, neutral-neutral reactions produce even higher water abundances (cf. Neufeld et al. 1995). Hence, our high abundance in the HC of H_2O can be the result of evaporation from grain surfaces, which also applies to CH_3OH and NH_3, as is discussed in more detail in Sect. 7.2. The water abundance in the CR and LVF is about the same, and lower than in the HC. This might be a natural consequence of a lower temperature in these regions with less evaporation from grain surfaces, which also applies to the PDR region. This is also the cause of the non-detection of water in the ER which has a temperature below the sublimation temperature. The highest water abundance is found in the HVF, which is suggestive of an even more efficient production in shocks.

Table 4. Relative abundances ratios and comparisons with ice abundances.

Abundance ratio	LVF	HC	CR	Ice abundances[a]	
	$N/N(H_2O) \times 100$			Orion IRc2	W33A
CH_3OH/H_2O		7	430	10	11–17
HDO/H_2O	0.52	0.13	3.2		0.3
$HDCO/H_2CO$			1.2		
NH_3/H_2O		13	7		15
SO_2/H_2O	69		36		~1.6
H_2CO/H_2O	0.5		3.6		~3
SO/H_2O	11		3.0		
OCS/H_2O		0.14		<0.2	0.2
CS/H_2O	0.41	0.02	1.4		
H_2S/H_2O	5.2	0.22			

[a] Gibb et al. (2000) and (2004).

7.2. Gas-phase vs. grain surface abundances

Ratios of our observed gas-phase column densities in the Orion LVF, HC and CR sources (as derived from Tables 1 and 2) and the water column density is found in Table 4. These ratios are compared with the corresponding grain-surface abundance ratios towards two of the sources observed by ISO (Gibb et al. 2000, 2004), Orion IRc2 and the embedded high-mass protostar W33A.

Some suggestions from these comparisons are:

– Both CH_3OH and H_2O are very abundant in the dense and warm HC, and their gas-phase abundance ratio is very similar to that in the grain-surface ice of Orion IRc2 and W33A. This strongly points at a dominant production via hydrogenation on cold grain surfaces and subsequent evaporation in the warm and hot cores (cf. Brown et al. 1988; Caselli et al. 1993; Stantcheva & Herbst 2004; Garrod & Herbst 2006;

Chang et al. 2007), especially so since gas-phase production of CH_3OH has been shown to be very inefficient (cf. Geppert et al. 2005; Millar 2005; Garrod et al. 2007). In the CR the CH_3OH/H_2O ratio is about 60 times higher than in the HC and in ices, caused by the four times decrease of the water abundance, and the 15 times higher methanol abundance as compared to the HC. This may suggest that H_2O is consumed in the formation of CH_3OH in accordance with the recent laboratory study of methanol formation from electron-irradiated mixed H_2O/CH_4 ice at 10 K by Wada et al. (2006).

- The rather similar gas-phase HDO/H_2O abundance ratios in the LVF and HC compared with the ice ratio in W33A most likely suggest efficient deuteration reactions on grain surfaces as the cause of the high water deuteration level. This is supported by our previous conclusions about the grain surface origin of the high water abundances. The much higher HDO/H_2O ratio found in the CR, as well as the similar $HDCO/H_2CO$ ratio, at least partly is caused by a decreasing H_2O abundance – possibly a result of H_2O consumption in the efficient grain-surface formation of CH_3OH in this source.
- Likewise, the gas-phase abundance ratios of NH_3 and H_2O in the CR and HC are similar to the W33A ice abundance ratio, again strongly suggesting that both these abundant species originate primarily from hydrogenation on cold grain surfaces with subsequent evaporation (cf. Stantcheva & Herbst 2004; Garrod et al. 2007).
- The high SO_2/H_2O abundance ratio observed in the LVF is contrasted with a low ice ratio in W33A. The latter ratio is most likely explained by rather inefficient gas-phase formation of SO_2 and subsequent adsorption onto already icy grain mantles formed by efficient hydrogenation on the cold grains. The high gas-phase H_2O abundance in the LVF may directly result from evaporation caused by the strong radiation from the nearby LVF driving source. This heating also could release S and Si atoms from the grains. Subsequent gas-phase reactions, based upon undepleted elemental abundances, then could lead to the elevated abundances of SO_2, SO, H_2S and SiO observed in the LVF. These abundances are several orders of magnitude higher than those in quiescent clouds where the abundances of S and Si appear to be depleted (B87; Irvine et al. 1987). In this scenario the ISO observations of OH at high abundance in the LVF (Goicoechea et al. 2006) are important. Low velocity shocks also may play a role here (cf. Mitchell 1984; Pineau des Forêts et al. 1993).
- The very similar CR H_2CO/H_2O gas-phase and W33A ice abundances most likely just tells us that both abundance ratios have the same main origin.
- The similarity of the HC gas-phase OCS/H_2O abundance ratio and the corresponding ratio in the W33A ice, also might hint at a grain surface origin of OCS. However, the comparatively low OCS abundance is accommodated by current ion-molecule reaction models and the ice content then likely is a result of adsorption.

8. Discussion – source sizes and source structure

We have in our column density and molecular abundance calculations in all cases treated the various Orion KL subregions, probed by the large Odin antenna beam, as homogeneous sources having specified average temperatures, densities and equivalent circular sizes and beam-filling factors.

However, the *High Velocity Outflow* is known to be bi-polar with a FWHP size of 60−70″, as estimated from simultaneous Odin mapping of the H_2O and CO $J = 5-4$ brightness distributions (Olofsson et al. 2003; Hjalmarson et al. 2005). As seen from the radiative transfer equation, the H_2O excitation temperature corresponding to a size of 70″ is only 26 K, while a temperature of 72 K as found by Wright et al. (2000) corresponds to a size of only 32″. This indicates a very clumpy H_2O brightness distribution, and that this source is filled with approximately one fourth of water emission. Similar results are obtained investigating the size-temperature relation of CO. In fact, the appearance of the HVF may be similar to the clumpy, finger-like emission seen in shock-excited H_2 (Salas et al. 1999)[4].

The *Low Velocity Outflow* has a NE-SW elongated structure, roughly orthogonal to the HVF, which also must have small scale structure (Genzel et al. 1981; Greenhill et al. 1998). If we guide ourselves by the optically thick HDO lines observed by Pardo et al. (2001) and use a HPBW size of 15″ for $H_2^{18}O$, the corresponding excitation temperature is only 40 K. The size corresponding to 72 K is 10″ which suggests that this source is filled with about one half of radiating gas-phase water. Similar results are found for all optically thick outflow species.

The *Compact Ridge* and *Hot Core* size-temperature relations are more consistent with the assumed values, although we know from Beuther et al. (2005) that both sources are very clumpy. This might be caused by their much smaller size as compared to the outflows, where the clumping affects larger scales. As seen from the CH_3OH Fig. 46 (online material) and Fig. 12, the source size of the CR also varies with the upper state energies of the lines. This might indicate considerable temperature and density variations within the CR.

Considering the uncertainties discussed above and in Sects. 3 and 10.2 (Appendix), the striking agreement with B87 and S95 strengthens our confidence of our results.

9. Summary

We present first results from a spectral line survey towards Orion KL in a frequency range inaccessible from the ground covering 487−492 and 542−577 GHz.

Some of the results from this survey:

1. We detect a total of 280 lines from 38 different molecular species.
2. In addition we detect 64 unidentified lines, which represents 19% of the total. Some tentative assignments of a few of them have been made such as the interstellar anion SH^-, ND, SO^+, and CH_3OCHO.
3. The total *beam-averaged* emission in our survey is dominated by CO, *o*-H_2O, SO_2, SO, ^{13}CO and CH_3OH. Species with the largest number of lines are CH_3OH, $(CH_3)_2O$, SO_2, $^{13}CH_3OH$, CH_3CN and NO.
4. Six water lines are detected, including the ground state rotational transition $1_{1,0}-1_{0,1}$ of *o*-H_2O, and its isotopologues *o*-$H_2^{18}O$ and *o*-$H_2^{17}O$, which shows emission from the Low- and High Velocity Flow and the Compact Ridge. Hot Core emission from water is observed from the *p*-H_2O transition $6_{2,4}-7_{1,7}$ with an upper state energy 867 K, and from a weak line feature at 489.054 GHz identified as the $4_{2,3}-3_{3,0}$ transition of *o*-$H_2^{18}O$ with an upper state energy of 430 K. We have also observed the HDO $2_{0,2}-1_{1,1}$ transition from the Low

[4] See also www: `http://subarutelescope.org/Science/press-release/9901/OrionKL_300.jpg`

Velocity Flow, Compact Ridge and the Hot Core, and have a tentative detection of the high energy transition (581 K) $6_{2,4}-6_{2,5}$ of HDO.

5. We detect the 1_0–0_0 transitions of NH_3 and the isotopologue $^{15}NH_3$. The main isotopologue shows emission from both the Hot Core, LVF and Compact Ridge, while the rarer isotopologue only exhibits emission from the Hot Core.
6. Isotopologue abundance ratios of D/H, $^{12}C/^{13}C$, $^{32}S/^{34}S$, $^{34}S/^{33}S$ and $^{18}O/^{17}O$ are calculated, as well as the molecular abundance ratio of O/S, all in agreement with previous findings.
7. Different methods are used to obtain rotation temperatures and column densities. For eight different species with at least four lines and a sufficient energy range in the transitions, the rotation diagram method and the forward model are applied. The LTE approximation is used for all the other species.
8. Abundances are estimated for the observed species from the different subregions, and we find very high gas-phase abundances of H_2O, NH_3, SO_2, SO, NO, and CH_3OH. An important fact here is that all our abundance determinations, including those for water vapour, are based upon the same methodology.
9. A comparison of our estimated gas-phase abundances with the ice inventory of ISO is shedding new light on the chemical origins of H_2O, CH_3OH, NH_3 and SO_2 in the various Orion KL subregions.
10. The line density in our survey is 4–20 per GHz, with a mean of 8 per GHz. This is comparable with larger telescopes ($\sim$10 GHz^{-1}), showing the excellent performance of the Odin satellite.

Acknowledgements. Generous financial support from the Research Councils and Space Agencies in Sweden, Canada, Finland and France is gratefully acknowledged. We sincerely thank Frank Lovas for a CD containing his molecular spectroscopy database SLAIMØ3, and are very grateful to the dedicated scientists supporting the molecular spectroscopy database the Cologne Database for Molecular Spectroscopy (CDMS) and the Jet Propulsion Laboratory (JPL) for making the difficult but absolutely necessary molecular spectroscopy available on the Internet. We also thank the referees whose constructive comments led to significant improvements of the paper.

References

Araya, E., Hofner, P., Kurtz, S., Bronfman, L., & DeDeo, S. 2005, ApJS, 157, 279
Batrla, W., Wilson, T. L., Bastien, P., & Ruf, K. 1983, A&A, 128, 279
Bensch, F., Pak, I., Wouterloot, J. G. A., Klapper, G., & Winnewisser, G. 2001, ApJ, 562, L185
Beuther, H., Zhang, Q., Greenhill, L. J., et al. 2005, ApJ, 632, 355
Bevington, P. R. 1969, Data Reduction and Error Analysis for the Physicas Sciences (McGraw-Hill book company)
Blake, G. A., Sutton, E. C., Masson, C. R., & Phillips, T. G. 1986, ApJS, 60, 357
Blake, G. A., Sutton, E. C., Masson, C. R., & Phillips, T. G. 1987, ApJ, 315, 621 (B87)
Brown, P. D., Charnley, S. B., & Millar, T. J. 1988, MNRAS, 231, 409
Caselli, P., Hasegawa, T. I., & Herbst, E. 1993, ApJ, 408, 548
Cernicharo, J., Goicoechea, J. R., Daniel, F., et al. 2006, ApJ, 649, 33
Chang, Q., Cuppen, H. M., & Herbst, E. 2007, A&A, 469, 973
Cheung, A. C., Rank, D. M., Townes, C. H., Thornton, D. D., & Welch, W. J. 1968, Phys. Rev. Lett., 21, 1701
Chin, Y.-N., Henkel, C., Whiteoak, J. B., Langer, N., & Churchwell, E. B. 1996, A&A, 305, 960
Comito, C., Schilke, P., Phillips, T. G., et al. 2005, ApJS, 156, 127 (C05)
Friberg, P. 1984, A&A, 132, 265
Garrod, R. T., & Herbst, E. 2006, A&A, 457, 927
Garrod, R. T., Wakelam, V., & Herbst, E. 2007, A&A, 467, 1103
Gensheimer, P. D., Mauersberger, R., & Wilson, T. L. 1996, A&A, 314, 281
Genzel, R., & Stutzki, J. 1989, ARA&A, 27, 41
Genzel, R., Reid, M. J., Moran, J. M., & Downes, D. 1981, ApJ, 244, 884
Genzel, R., Downes, D., Ho, P. T. P., & Bieging, J. 1982, ApJ, 259, L103
Geppert, W., Hellberg, F., Österdahl, et al. 2005, IAU Symp. 231, ed. D. C. Lis, G. A. Blake, & E. Herbst (Cambridge University Press), 117
Gibb, E. L., Whittet, D. C. B., Schutte, W. A., et al. 2000, ApJ, 536, 347
Gibb, E. L., Whittet, D. C. B., Boogert, A. C. A., & Tielens, A. G. G. M. 2004, ApJS, 151, 35
Goicoechea, J. R., Cernicharo, J., Lerate, M. R., et al. 2006, ApJ, 641, L49
Goldsmith, P. F., & Langer, W. D. 1999, ApJ, 517, 209
Goldsmith, P. F., Bergin, E. A., & Lis, D. C. 1997, ApJ, 491, 615
Greenhill, L. J., Gwinn, C. R., Schwartz, C., Moran, J. M., & Diamond, P. J. 1998, Nature, 396, 650
Grevesse, N., Noels, A., & Sauval, A. J. 1996, ASP Conf. Ser., 99, 117
Groner, P., Albert, S., Herbst, E., & de Lucia, F. C. 1998, ApJ, 500, 1059
Hermsen, W., Wilson, T. L., Walmsley, C. M., & Batrla, W. 1985, A&A, 146, 134
Hermsen, W., Wilson, T. L., & Bieging, J. H. 1988a, A&A, 201, 276
Hermsen, W., Wilson, T. L., Walmsley, C. M., & Henkel, C. 1988b, A&A, 201, 285
Hjalmarson, Å., Bergman, P., Biver, N., et al. 2005, Adv. Space Res., 36, 1031
Ho, P. T. P., & Townes, C. H. 1983, ARA&A, 21, 239
Hollis, J. M., Lovas, F. J., Suenram, R. D., Jewell, P. R., & Snyder, L. E. 1983, ApJ, 264, 543
Ikeda, M., Maezawa, H., Ito, T., et al. 1999, ApJ, 527, L59
Irvine, W. M., Schloerb, F. P., Hjalmarson, Å., & Herbst, E. 1985, in Protostars and Planets II, ed. D. C. Black, & M. S. Matthews (University of Arizona Press), 579
Irvine, W. M., Goldsmith, P. F., & Hjalmarson, Å. 1987, in Interstellar Processes, ed. D. J. Hollenbach, & H. A. Thronson, Jr. (Reidel Publishing Co), 561
Johansson, L. E. B., Andersson, C., Elldér, J., et al. 1984, A&A, 130, 227
Kahane, C., Gomez-Gonzalez, J., Cernicharo, J., & Guélin, M. 1988, A&A, 1988, 190, 167
Keene, J., Blake, G. A., & Phillips, T. G. 1983, ApJ, 271, L27
Lampton, M., Margon, B., & Bowyer, S. 1976, ApJ, 208, 177
Larsson, B., Liseau, R., Bergman, P., et al. 2003, A&A, 402, L69
Lerate, M. R., Barlow, M. J., Swinyard, B. M., et al. 2006, MNRAS, 370, 597
Liseau, R., Larsson, B., Brandeker, A., et al. 2003, A&A, 402, L73
Lovas, F. J. 2003, Spectral Line Atlas for Interstellar Molecules (SLAIMØ3) Ver.1, private communication of a CD
Mangum, J. G., Wootten, A., Loren, R. B., & Wadiak, E. J. 1990, ApJ, 348, 542
Masson, C. R., Lo, K. Y., Phillips, T. G., et al. 1987, ApJ, 319, 446
Melnick, G. J., Stauffer, J. R., Ashby, M. L. N., et al. 2000, ApJ, 539, L77
Menten, K. M., Walmsley, C. M., Henkel, C., et al. 1986, A&A, 169, 271
Menten, K. M., Walmsley, C. M., Henkel, C., & Wilson, T. L. 1988, A&A, 198, 253
Migenes, V., Johnston, K. J., Pauls, T. A., & Wilson, T. L. 1989, ApJ, 347, 294
Millar, T. J. 2005, IAU Symp., 231, ed. D. C. Lis, G. A. Blake, & E. Herbst (Cambridge University Press), 77
Mitchell, G. F. 1984, ApJ, 287, 665
Müller, H. S. P., Thorwirth, S., Roth, D. A., & Winnewisser, G. 2001, A&A, 370, L49
Nagai, T., Kaifu, N., Nagane, K., & Akaba, K. 1979, PASJ, 31, 317
Neufeld, D. A., Lepp, S., & Melnick, G. J. 1995, ApJS, 100, 132
Neufeld, D. A., Green, J. D., Hollenbach, et al. 2006, ApJ, 647, L33
Nordh, H. L., von Schéele, F., Frisk, U., et al. 2003, A&A, 402, L21
Nummelin, A., Dickens, J. E., Bergman, P., et al. 1998, A&A, 337, 275
Nummelin, A., Bergman, P., Hjalmarson, Å., et al. 2000, ApJS, 128, 213
Olofsson, H. 1984, A&A, 134, 36O
Olofsson, H., Hjalmarson, Å., & Rydbeck, O. E. H. 1981, A&A, 100, L30
Olofsson, H., Elldér, J., Hjalmarson, Å., & Rydbeck, O. E. H. 1982, A&A, 113, L18
Olofsson, A. O. H. 2003, Thesis, Chalmers University of Techonology, ISBN 91-7291-341-X
Olofsson, A. O. H., Olofsson, G., Hjalmarson, Å., et al. 2003, A&A, 402, L47
Olofsson, A. O. H., Persson, C. M., Koning, N., et al. 2007, A&A, 476, 791 (Paper I)
Pardo, J. R., Cernicharo, J., Herpin, F., et al. 2001, ApJ, 562, 799
Pauls, T. A., Wilson, T. L., Bieging, J. H., & Martin, R. N. 1983, A&A, 124, 23
Penzias, A. A. 1981a, ApJ, 249, 513
Penzias, A. A. 1981b, ApJ, 249, 518
Phillips, T. G., Wannier, P. G., Scoville, N. Z., & Huggins, P. J. 1979, ApJ, 231, 720
Pickett, H. M., Poynter, R. L., Cohen, E. A., et al. 1998, J. Quant. Spectrosc. & Rad. Transfer, 60, 883
Pineau des Forêts, G., Roueff, E., Schilke, P., & Flower, D. R. 1993, MNRAS, 262, 915

Plume, R., Bensch, F., Howe, J. E., et al. 2000, ApJ, 539, L133
Rodríguez-Franco, A., Martín-Pintado, J., & Fuente, A. 1998, A&A, 329, 1097
Rodríguez-Franco, A., Wilson, T. L., Martín-Pintado, J., & Fuente, A. 2001, ApJ, 559, 985
Salas, L., Rosando., M., Cruz-González, I., et al. 1999, ApJ, 511, 822
Savage, C., Apponi, A. J., Ziurys, L. M., & Wyckoff, S. 2002, ApJ, 578, 211
Schilke, P., Güsten, R., Schulz, A., Serabyn, E., & Walmsley, C. M. 1992, A&A, 261, L5
Schilke, P., Benford, D. J., Hunter, T. R., Lis, D. C., & Phillips, T. G. 2001, ApJS, 132, 281 (S01)
Schöier, F. L., van der Tak, F. F. S., van Dishoeck, E. F., & Black, J. H. 2005, A&A, 432, 369
Serabyn, E., & Weisstein, E. 1995, ApJ, 451, 238
Stantcheva, T., & Herbst, E. 2004, A&A, 423, 241
Sutton, E. C., Blake, G. A., Genzel, R., Masson, C. R., & Phillips, T. G. 1986, ApJ, 311, 921
Sutton, E. C., Peng, R., Danchi, W. C., et al. 1995, ApJS, 97, 455 (S95)
Tauber, J. A., Lis, D. C., Keene, J., Schilke, P., & Büttgenbach, T. H. 1995, A&A, 297, 567
Turner, B. E. 1990, ApJ, 362, L29
Turner, B. E. 1991, ApJS, 76, 617
Ungerechts, H., Bergin, E. A., Goldsmith, et al. 1997, ApJ, 482, 245
Wada, A., Mochizuki, N., & Hiraoka, K. 2006, ApJ, 644, 300
Watson, D. M., Genzel, R., Townes, C. H., & Storey, J. W. V. 1985, ApJ, 298, 316
White, G. J., Araki, A., Greaves, J. S., Ohishi, M., & Higginbottom, N. S. 2003, A&A, 407, 589 (W03)
Wilner, D. J., Wright, M. C. H., & Plambeck, R. L. 1994, ApJ, 422, 642
Wilson, T. L., & Matteucci, F. 1992, A&ARv., 4, 1
Wilson, T. L., & Rood, R. 1994, ARA&A, 32, 191
Wilson, T. L., Downes, D., & Bieging, J. 1979, A&A, 71, 275
Wilson, T. L., Serabyn, E., Henkel, C., & Walmsley, C. M. 1986, A&A, 158, L1
Wilson, T. L., Gaume, R. A., Gensheimer, P., & Johnston, K. J. 2000, ApJ, 538, 665
Wirström, E. S., Bergman, P., Olofsson, A. O. H., et al. 2006, A&A, 453, 979 (W06)
Womack, M., Ziurys, L. M., Wyckoff, S., & Sage, L. 1990, BAAS, 22, 1329
Wouterloot, J. G. A., Brand, J., & Henkel, C. 2005, A&A, 430, 549
Wright, M. C. H., Plambeck, R. L., & Wilner, D. J. 1996, ApJ, 469, 216
Wright, C. M., van Dishoeck, E. F., Black, J. H., et al. 2000, A&A, 358, 689

Online Material

10. Data analysis methods

10.1. Single line analysis

With the assumption of optically thin emission, neglecting the background radiation, and assuming that the source fills the antenna main beam, the beam averaged upper state column density is calculated as

$$N_{\rm u}^{\rm thin} = \frac{8\pi k \nu_{{\rm u}l}^2}{hc^3} \frac{1}{A_{{\rm u}l}} \int T_{\rm mb}\, {\rm d}\upsilon, \tag{8}$$

where k is the Boltzmann constant, $\nu_{{\rm u}l}$ is the frequency of the transition, h is the Planck constant, c is the speed of light, $A_{{\rm u}l}$ is the Einstein A-coefficient for the transition, and $T_{\rm mb}$ is the main beam brightness temperature. As customary the frequency axis ν has been converted to a velocity axis υ using the speed of light.

The total column density of each species can then be found assuming LTE (Local Thermodynamic Equilibrium), where the excitation temperatures, $T_{\rm ex}$, for all the energy levels are the same. The molecular population of each level is then given by the Boltzmann equation, which also defines $T_{\rm ex}$

$$N_{\rm u} = N_{\rm tot} \frac{g_{\rm u}}{Q(T)}\, {\rm e}^{-E_{\rm u}/kT_{\rm ex}}, \tag{9}$$

where $g_{\rm u}$ is the statistical weight of the upper state, and $Q(T)$ is the partition function, which only depends on temperature and molecular constants and hence differs for different kinds of species. The A-coefficients, statistical weights, partition functions and upper state energy levels are available via the databases JPL, CDMS, Leiden[5] (Schöier et al. 2005) or SLAIMØ3. For a few molecules, e.g. $(CH_3)_2O$, we calculate the A-coefficients using line strengths found in SLAIMØ3 as

$$A_{{\rm u}l} = \frac{16\,\pi^3\,\nu_{{\rm u}l}^3\,\mu^2}{3\,\epsilon_0\,h\,c^3} \frac{S_{{\rm u}l}}{g_{\rm u}} \tag{10}$$

where $S_{{\rm u}l}$ is the rotational part of the line strength, and μ is the molecular dipole moment.

From Eqs. (9) and (1), we obtain *the beam-averaged total column density*

$$N_{\rm tot}^{\rm thin} = \frac{8\pi k \nu_{{\rm u}l}^2}{hc^3} \frac{1}{A_{{\rm u}l}} \frac{Q(T)}{g_{\rm u}} {\rm e}^{\,E_{\rm u}/kT_{\rm ex}} \int T_{\rm mb}\, {\rm d}\upsilon \tag{11}$$

assuming optically thin emission.

The solution of the radiative transport equation, neglecting background radiation and with a constant source function, is

$$T_{\rm A}^* = T_{\rm b}\,\eta_{\rm mb}\,\eta_{\rm bf} = J(T_{\rm ex})\,(1-{\rm e}^{-\tau})\,\eta_{\rm mb}\,\eta_{\rm bf}, \tag{12}$$

where the beam-filling factor $\eta_{\rm bf} = \theta_{\rm s}^2/(\theta_{\rm s}^2+\theta_{\rm mb}^2)$, assuming that both the source brightness distribution and the antenna response are circularly symmetric and Gaussian. The radiation temperature, $J(T_{\rm ex})$ is

$$J(T_{\rm ex}) = \frac{h\nu}{k} \frac{1}{{\rm e}^{h\nu/kT_{\rm ex}}-1} \approx T_{\rm ex}, \tag{13}$$

where the approximation is valid only if $h\nu \ll kT_{\rm ex}$. For the appropriate temperatures in this region, $T \approx 100{-}200$ K, and frequencies ~550 GHz, the radiation temperature will differ from $T_{\rm ex}$ by approximately 10−15%. Accordingly, we use $J(T_{\rm ex})$ and not $T_{\rm ex}$ in our calculations.

[5] http://www.strw.leidenuniv.nl/~moldata/

If the emission is optically thick ($\tau \gg 1$) Eq. (12) simplifies to

$$T_{\rm A}^* = J(T_{\rm ex})\,\eta_{\rm mb}\,\eta_{\rm bf} = J(T_{\rm ex})\,\eta_{\rm mb}\,\frac{\theta_{\rm s}^2}{\theta_{\rm s}^2+\theta_{\rm mb}^2}. \tag{14}$$

Using this equation the beam-filling, and hence the approximate source size, can be determined without relying on correctly calculated optical depths. The variation in $T_{\rm A}^*$ that is seen mainly will be due to variations in the beam-filling factor, but there can also be variations in $T_{\rm ex}$, both along the path and between different states, which cannot be determined.

Since molecular clouds are known to be clumpy down to very small scales, it is indeed likely that the source does not fill the beam. This is especially true in case of the large Odin beam, and the total column density from Eq. (11) will be too low by a factor of $1/\eta_{\rm bf}$. Variations in beam-filling between the different transitions of the same molecule also are probable. Hence, when we are comparing other observations (e.g. interferometry mapping) with ours to estimate the beam-filling, by necessity we have to compare transitions with similar parameters tracing the same gas.

The optical depth at the centre of the line can be calculated, assuming LTE and a Gaussian line profile, using

$$\tau_{\rm max} = \sqrt{\frac{\ln 2}{16\,\pi^3}} \frac{c^3}{\nu_{{\rm u}l}^3\,\Delta\upsilon}\, A_{{\rm u}l}\, N_{\rm tot}\, \frac{g_{\rm u}}{Q(T)}\, {\rm e}^{-E_{\rm u}/kT_{\rm ex}}\, ({\rm e}^{h\nu_{{\rm u}l}/kT_{\rm ex}}-1) \tag{15}$$

where $\Delta\upsilon$ is the width of the line, and $E_{\rm u}$ is the upper state energy. However, this approach demands knowledge of the total column density. If we have observations of isotopologues, and if the isotopologue abundance ratio R is known, then the optical depths can be determined by means of Eq. (12). If the excitation temperatures are about the same for both isotopologues, and the optical depth of isotopologue one is larger than isotopologue two by a factor R, we then will have

$$\frac{T_{\rm A,1}}{T_{\rm A,2}} = \frac{(1-{\rm e}^{-\tau_1})\,\eta_{\rm bf,1}}{(1-{\rm e}^{-\tau_2})\,\eta_{\rm bf,2}} = \frac{(1-{\rm e}^{-R\,\tau_2})\,\eta_{\rm bf,1}}{(1-{\rm e}^{-\tau_2})\,\eta_{\rm bf,2}}. \tag{16}$$

This will give the mean optical depths of both species. If the emissions are co-spatial the beam-filling factors cancel.

Once a transition has become optically thick, the value of $N_{\rm u}/g_{\rm u}$ cannot increase any further. The derived total column density will then be too low and needs an optical depth correction factor C_τ, which will be one or larger

$$C_\tau = \frac{\tau}{1-{\rm e}^{-\tau}}. \tag{17}$$

With corrections for optical depth and beam-filling the *true total source averaged column density* will be

$$N_{\rm tot} = \frac{C_\tau}{\eta_{\rm bf}} \frac{8\pi k \nu_{{\rm u}l}^2}{hc^3} \frac{1}{A_{{\rm u}l}} \frac{Q(T)}{g_{\rm u}} {\rm e}^{E_{\rm u}/kT_{\rm ex}} \int T_{\rm mb}\, {\rm d}\upsilon = \frac{C_\tau}{\eta_{\rm bf}}\, N_{\rm tot}^{\rm thin}. \tag{18}$$

If no information about optical depth is available this correction is not taken into account. For the excitation temperature in Eqs. (14) and (18), we use an adopted temperature that fits the species (Table 1), or the calculated rotation temperature $T_{\rm ROT}$ (see Sect. 3.2.1).

Note the importance of the partition function $Q(T)$, and the statistical weight $g_{\rm u}$ in Eq. (18). If the statistical weights include the *ortho*/*para* ratio whenever these molecular sub-divisions exist, the partition function must include them. It is also important to use the same statistical weights $g_{\rm u}$ in Eq. (18) when the partition function $Q(T)$ is calculated.

10.2. Additional limitations

If there are deviations from the basic assumptions, errors will occur in the calculations for all models (cf. Goldsmith & Langer 1999). These effects can to some extent be corrected for, like optical depth effects and beam-filling, as discussed above. In addition we have:

1. *Several excitation temperatures/non-LTE.* The population distribution may not be characterised by a single rotational temperature. The temperature can vary due to density, excitation gradients along the line-of-sight, IR flux, subthermal excitation etc. Since our beam is very large and encompasses a variety of different conditions, we may expect emission from several different sources, each with different temperature.
2. *Adopted excitation temperature.* Whenever we have too few lines to use the rotation diagram method or forward model we use the LTE approximation for a single line. The excitation temperature is then adopted from a rotation temperature of a similar species in our survey, or taken from the literature. This can create errors if the adopted temperature is not appropriate.
3. *Source structure.* The beam-filling correction are calculated assuming a homogenous source (see also Sect. 8). Clumping and substructures can introduce errors in the beam-filling corrections. Vastly different opacitites between the isotopologues (with NH_3 and H_2O as good examples) also complicate the analysis, as the beam-filling factors may be very different.
4. *Gaussian decomposition.* Errors in our Gaussian decompositions can introduce errors in the calculated optical depths and the column densities.
5. *H_2 column densities.* The largest source of uncertainty in the abundances in Sect. 7 is the adopted H_2 column densities and the assumption that the H_2 emission and the molecule of interest spatially coincides. This can create errors by orders of magnitude.
6. *Observational errors.* Errors may exist in the measured line intensities due to misidentifications, unresolved blends, or pointing and calibration. However, the errors must be rather large to create significant errors in the column density obtained from the rotation diagram and forward model.
7. *Background radiation.* The background radiation, for example emission from warm dust, may be too large to be neglected. If the condition $T_{\rm ex} \gg T_{\rm bg}$ is violated, shifts along the ordinate in the rotation diagram with a factor of $\ln(1-T_{\rm bg}/T_{\rm ex})$ will occur. The dust continuum radiation will for example affect the level populations of water, and must be included in accurate calculations for these transitions.

10.3. Determination of relative chemical abundances

The definition of molecular abundance of a species with respect to H_2 is the ratio of the volume densities. This demands detailed knowledge of the geometry of the emitting region. If this is not known, column densities can be used as a substitute, with the assumption that the two species are well mixed and emitted from the same region, to obtain average abundances along the line of sight

$$X_{\rm species} = \frac{N_{\rm species}}{N_{\rm H_2}}. \tag{19}$$

The use of column densities will provide a higher degree of accuracy than the use of volume densities (Irvine et al. 1985). As long as the molecules are emitted from the same region with approximately the same source size, there is no dependence of beam-filling. In addition, since we have a uniformly calibrated set of data, uncertainties in calibration will not affect the result.

The relative isotopologue abundance R can be determined in the same way as the molecular abundances,

$$R = \frac{N_1}{N_2}, \tag{20}$$

when we have observations of optically thin isotopologues, or opacity-corrected column densities.

10.4. Optical depth broadening

If the intrinsic line shape is Gaussian, a high line opacity will increase the observed line width (cf. Phillips et al. 1979) as

$$\Delta\upsilon \approx \Delta\upsilon_i \left(\frac{\ln\tau_{\rm p}}{\ln 2}\right)^{1/2} \tag{21}$$

where $\Delta\upsilon_i$ is the intrinsic velocity width of the line and $\tau_{\rm p}$ ($\gg$1) is the peak optical depth in the line.

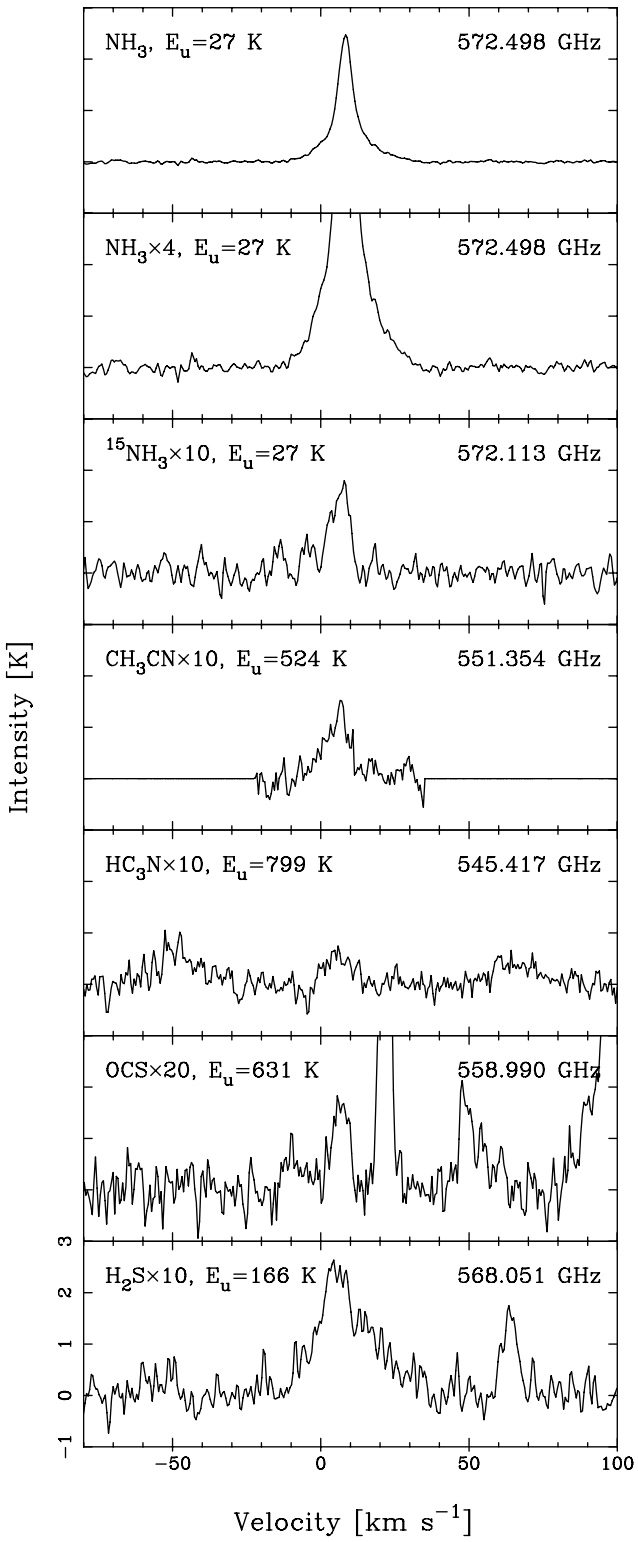

Fig. 25. Top figure shows the NH_3 line, the second figure shows four times magnified NH_3 line wings. The NH_3 line profile shows emission from the CR and HC. The $^{15}NH_3$, CH_3CN, HC_3N and OCS transitions suggest emission from the HC, and H_2S from both the HC and LVF. An intensity scale factor is given after the molecular species.

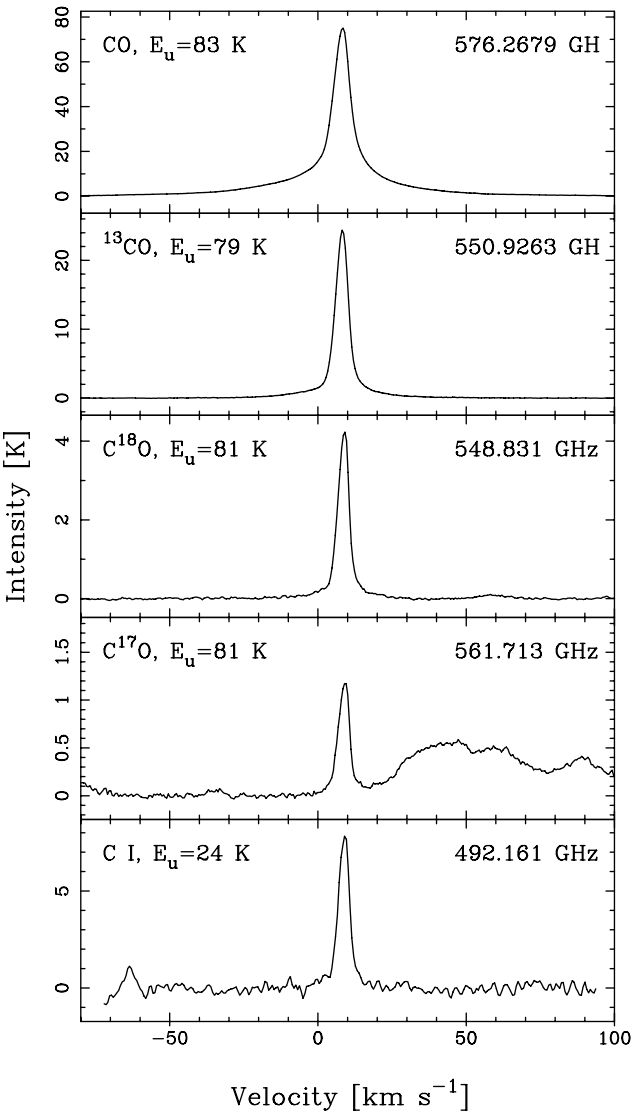

Fig. 26. CO, isotopologues and atomic C. Note the different intensity scales.

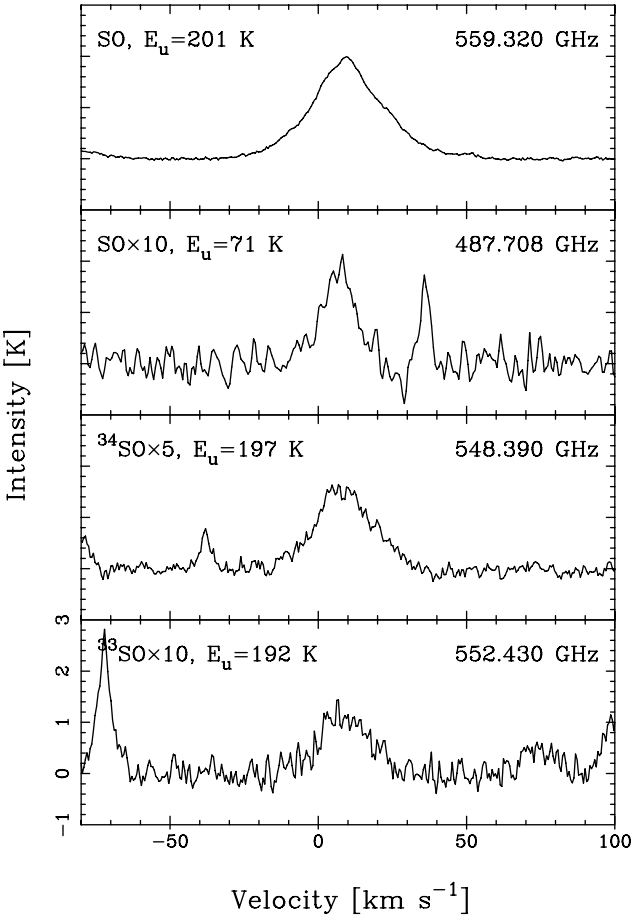

Fig. 27. SO and isotopologues. The SO line in the top panel is optically thick, and shows clear HVF line wings. The low-energy SO transition is optically thin. An intensity scale factor is given after the molecular species.

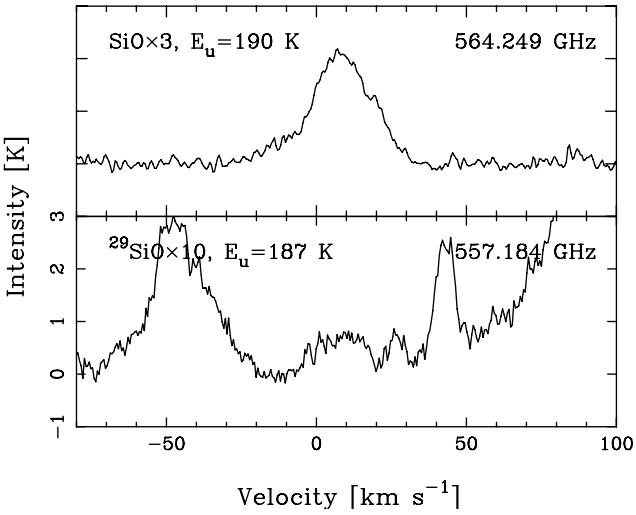

Fig. 28. The J = 13–12 transition for both SiO and ^{29}SiO. The SiO line is optically thick and also exhibits pronounced HVF line wings. A blend from CH_3OH and $^{13}CH_3OH$ is visible at 19.6 km s^{-1} in the SiO line. An intensity scale factor is given after the molecular species.

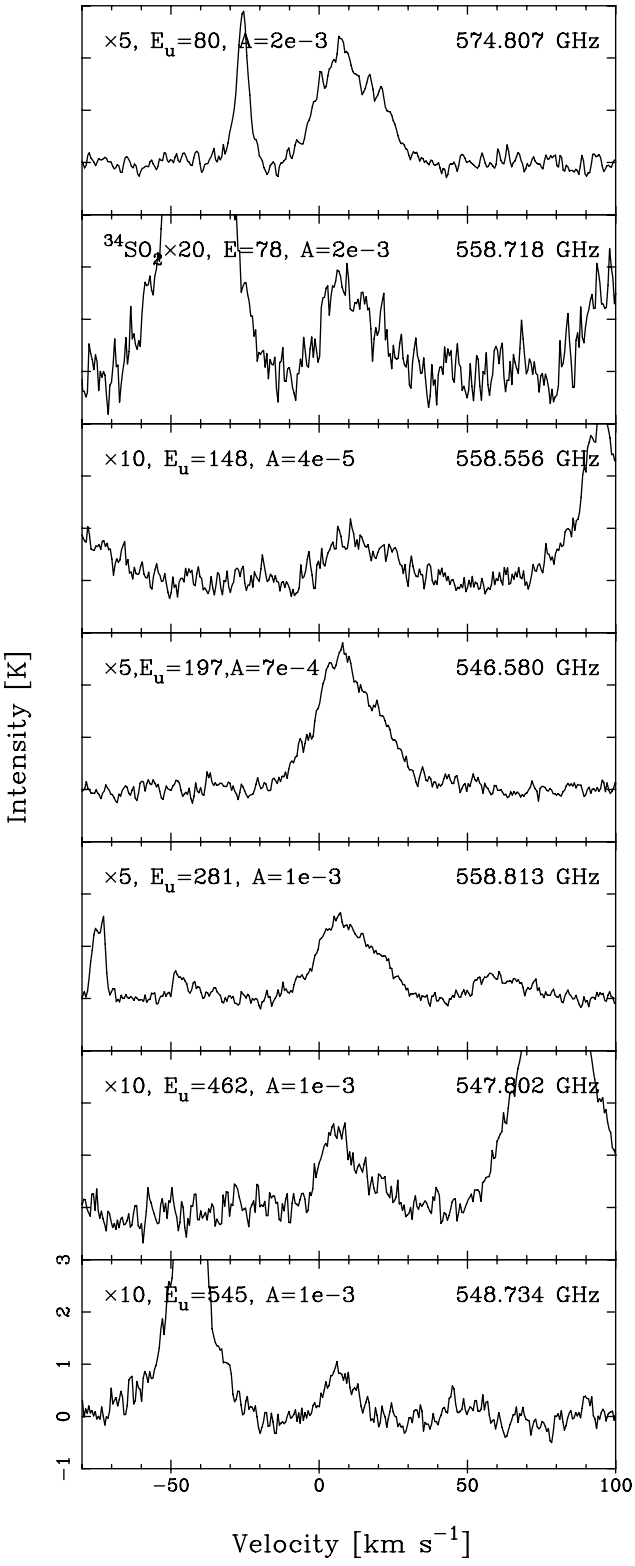

Fig. 29. SO_2 with different upper state energy levels and A-coefficients. The $^{34}SO_2$ line is the same transition as the SO_2 transition with E_u = 80 K. An intensity scale factor is given in the top left corners.

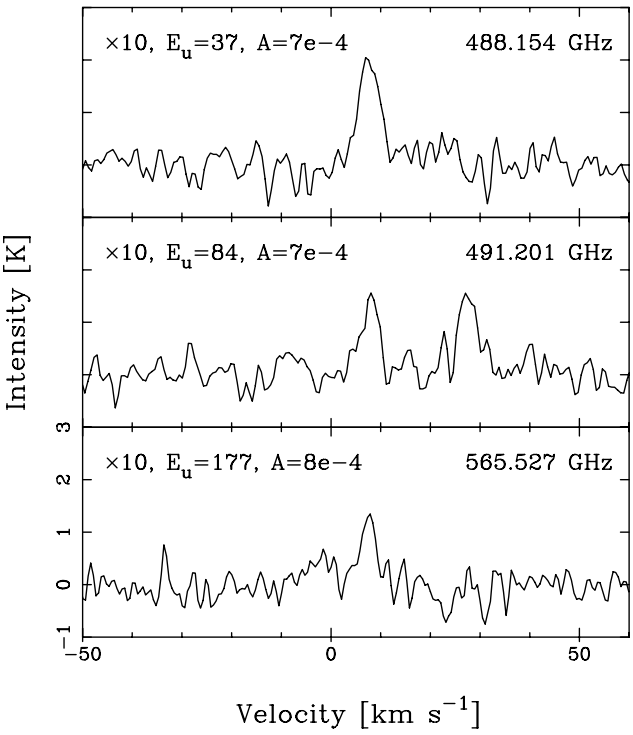

Fig. 30. $^{13}CH_3OH$ with emission from the CR. An intensity scale factor is given in the top left corners, upper state energies given in K and A-coefficients in s^{-1}.

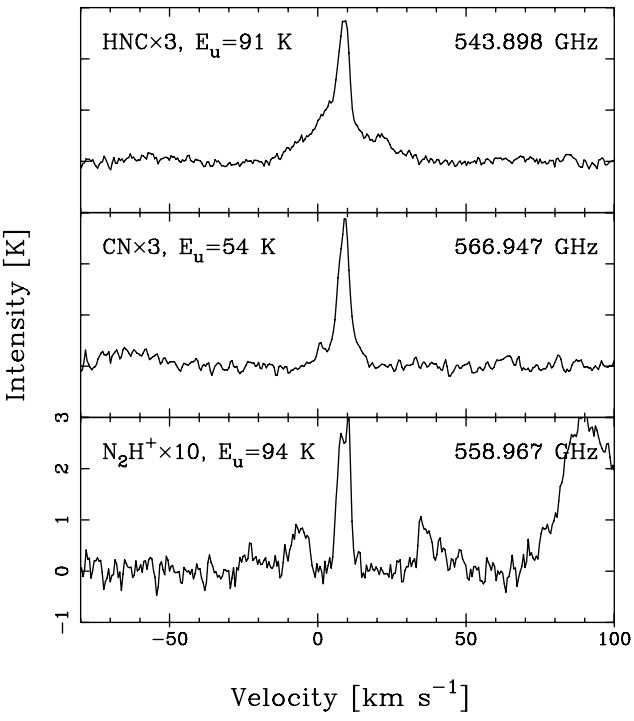

Fig. 31. The line profile of HNC shows emission from the ER, HC and LVF, CN from the PDR/ER and HC, and N_2H^+ from the ER. The line at $v \approx -8$ km s^{-1} next to N_2H^+ is OCS, which is also shown in Fig. 25. An intensity scale factor is given after the molecular species.

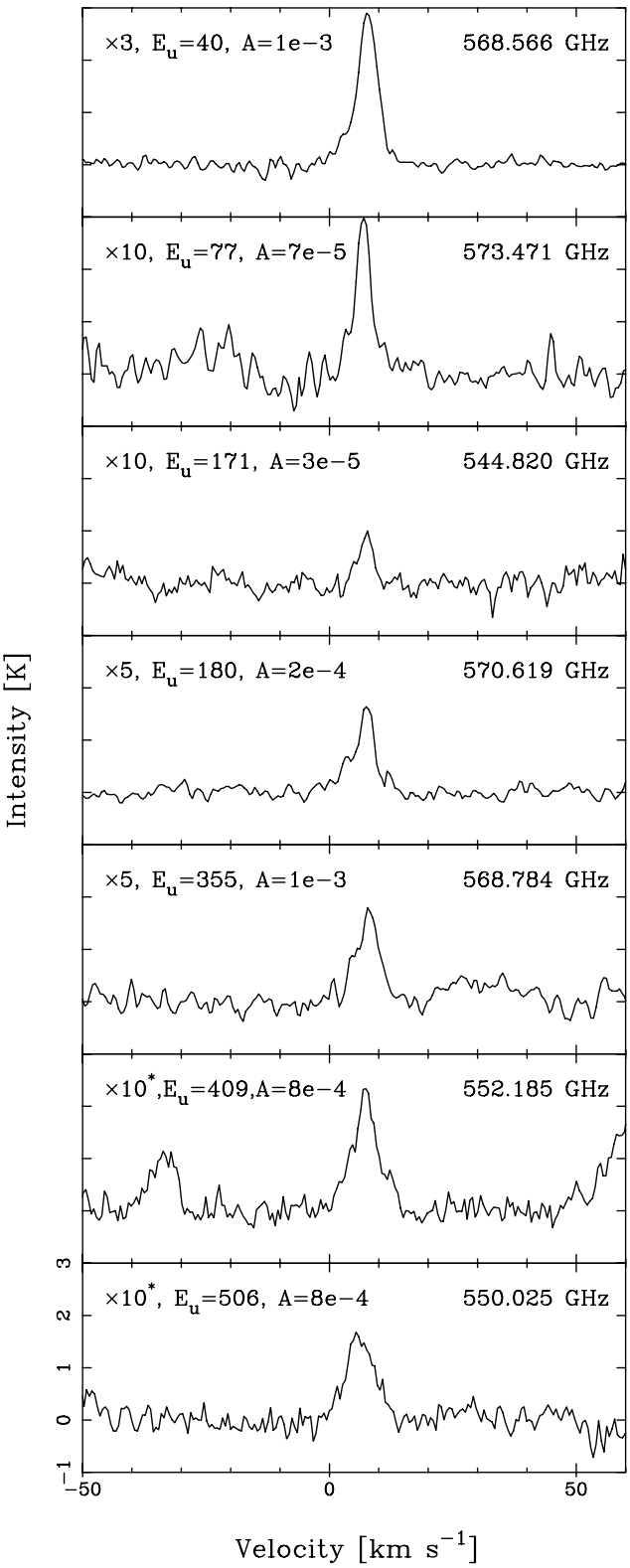

Fig. 32. CH_3OH with emission from both the CR and HC. Vibrationally excited transitions are marked by $*$ after the intensity scale factor given in the top left corners, with upper state energies given in K and A-coefficients in s^{-1}.

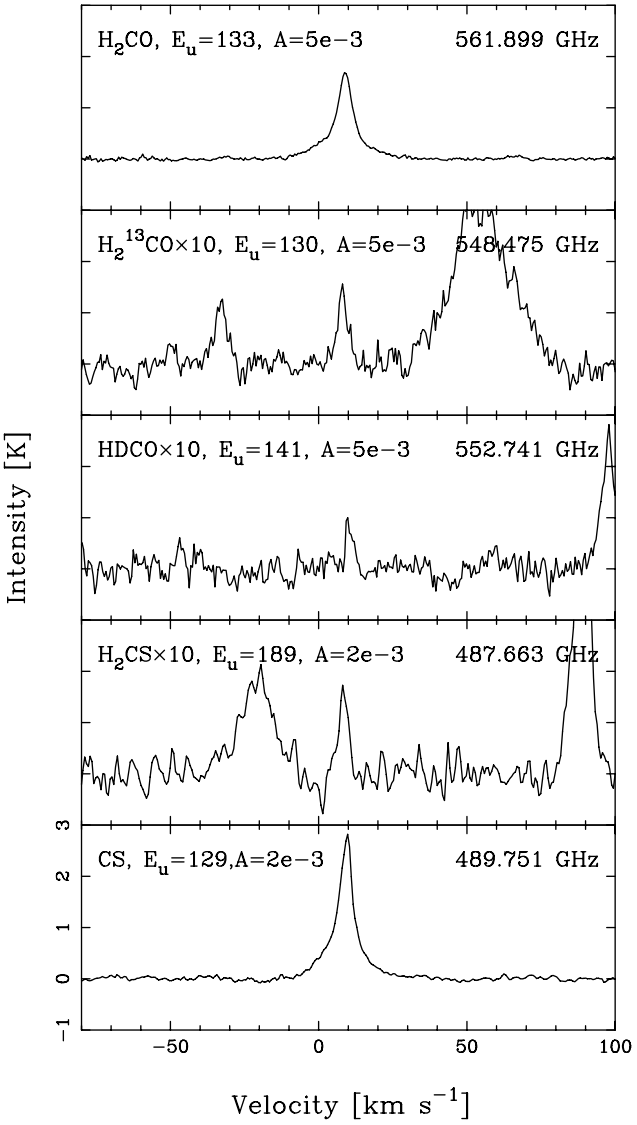

Fig. 33. The optically thick line profile of H_2CO show emission from the CR and LVF. The optically thin transitions of $H_2^{13}CO$, HDCO, and H_2CS show only emission from the CR. The CS line profile shows emission from the HC, LVF and a narrow component from the CR or ER. An intensity scale factor is given after the molecular species, the upper state energies are given in K and the *A*-coefficients in s^{-1}.

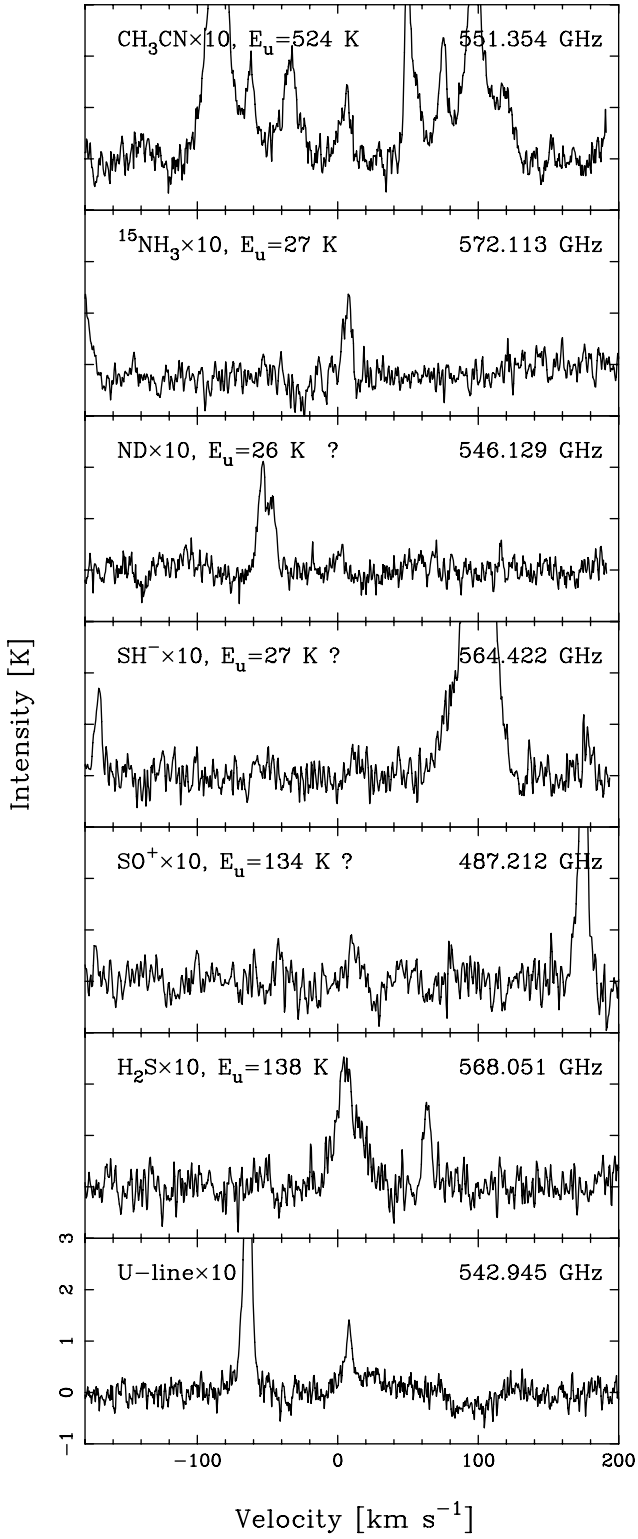

Fig. 34. Identification suggestions for a few U-lines together with $^{15}NH_3$, H_2S and CH_3CN as comparison lines. The U-line at 542.945 GHz is our strongest non-identified U-line. An intensity scale factor is given after the molecular species.

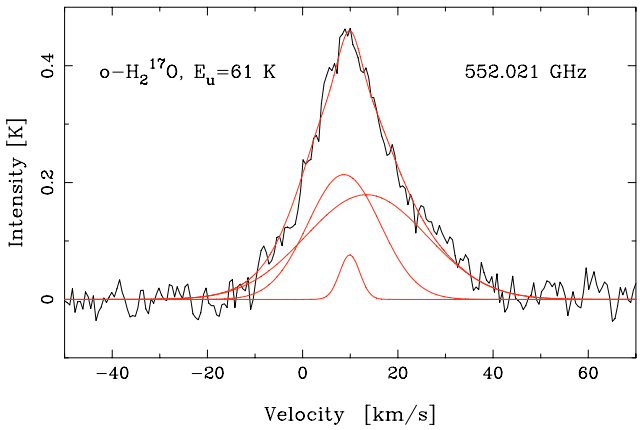

Fig. 35. A three-component Gaussian fit to $H_2^{17}O$ shown together with the individual Gaussians. The line widths are 5 km s^{-1}, 18 km s^{-1}, and 30 km s^{-1} from the CR, LVF and HVF, respectively.

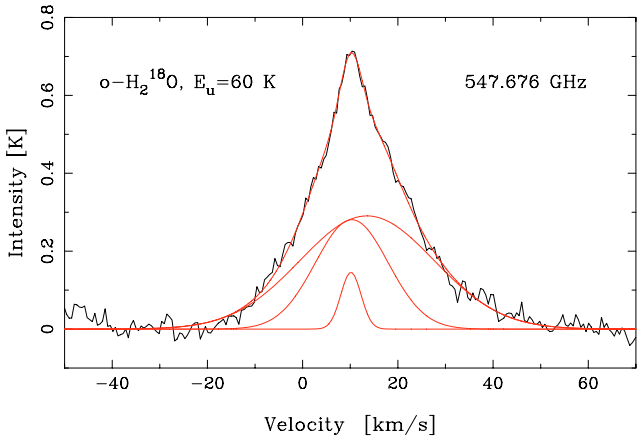

Fig. 36. A three-component Gaussian fit to $H_2^{18}O$ shown together with the individual Gaussians. The line widths are 5 km s^{-1}, 18 km s^{-1}, and 33 km s^{-1} from the CR, LVF and HVF, respectively.

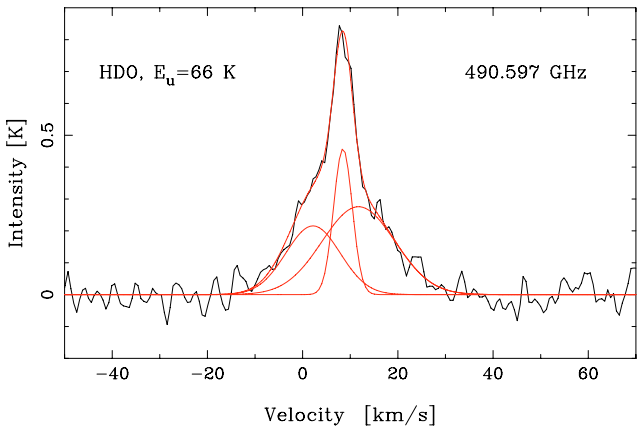

Fig. 37. A three-component Gaussian fit to HDO shown together with the individual Gaussians. The line widths are 5 km s^{-1}, 13 km s^{-1}, and 18 km s^{-1} for the CR, HC, and LVF, respectively.

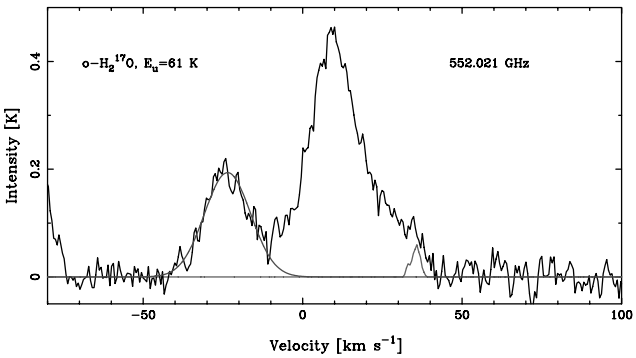

Fig. 38. $H_2^{17}O$ before removal of blends with reconstructed lines from SO_2 and CH_3OH shown.

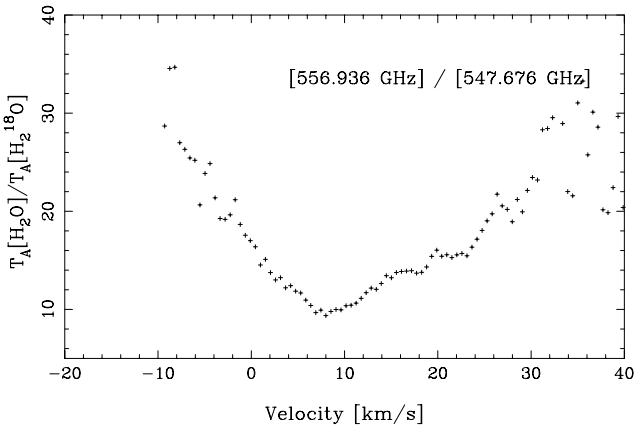

Fig. 39. Ratio of *o*-H_2O over *o*-$H_2^{18}O$.

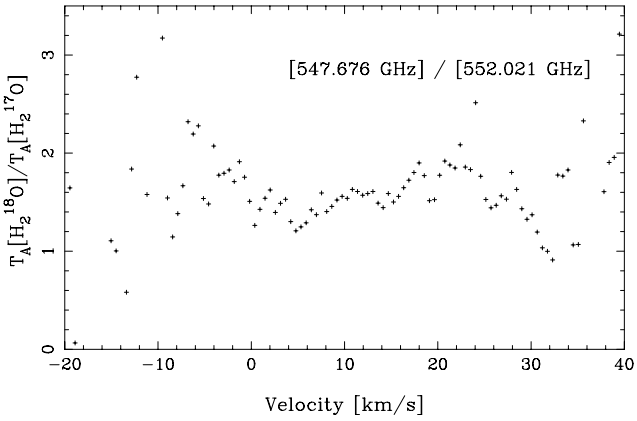

Fig. 40. Ratio of *o*-$H_2^{18}O$ over *o*-$H_2^{17}O$.

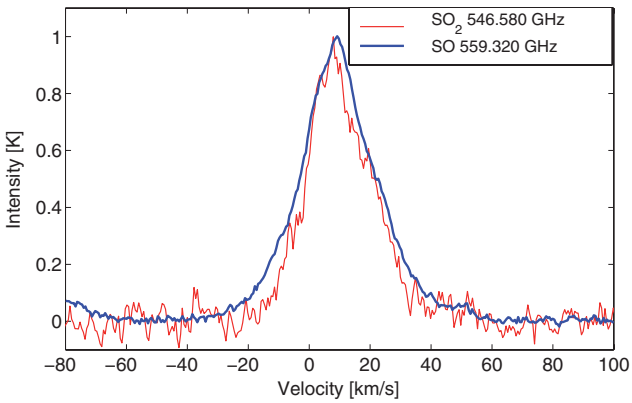

Fig. 41. Comparison of the SO and SO_2 line profiles. Both lines are normalised to unity.

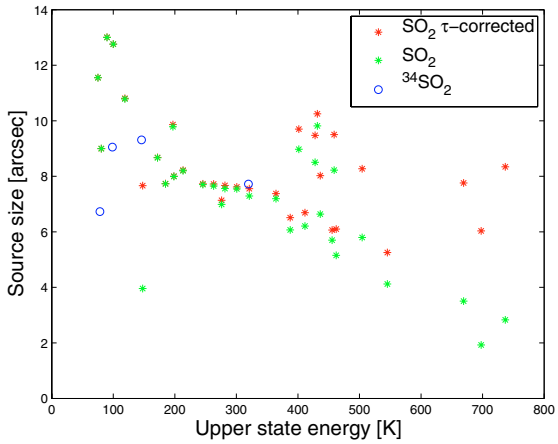

Fig. 42. Source sizes for opacity-corrected SO_2 (calculated with T_{ROT} = 103 K and source size = 8″) vs. non corrected SO_2 together with $^{34}SO_2$ (calculated with T_{ROT} = 125 K).

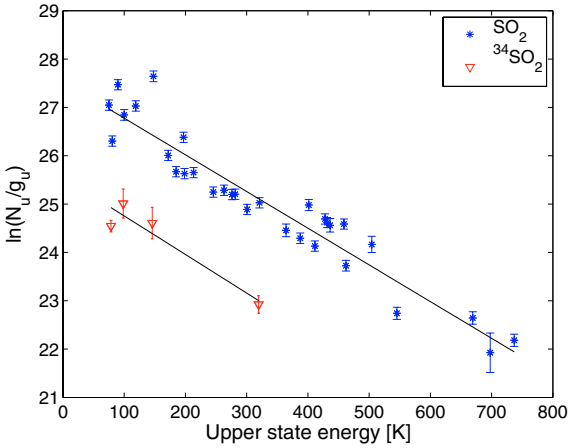

Fig. 43. Rotation diagram for SO_2, not corrected for opacity, produces T_{ROT} = 132 K and $N_{ROT} = 3.9 \times 10^{17}$ cm^{-2} (extended source). The $^{34}SO_2$ fit give T_{ROT} = 125 K and $N_{ROT} = 5.4 \times 10^{16}$ cm^{-2}.

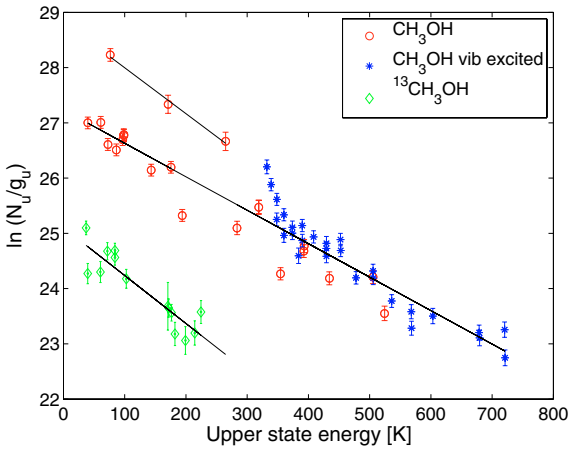

Fig. 44. Rotation diagrams: CH_3OH producing T_{ROT} = 165 K and $N_{ROT} = 9.3 \times 10^{17}$ cm^{-2} (not opacity corrected); three optically thin CH_3OH lines produces T_{ROT} = 120 K and $N_{ROT} = 2.6 \times 10^{18}$ cm^{-2}; $^{13}CH_3OH$ producing T_{ROT} = 115 K and $N_{ROT} = 5.9 \times 10^{17}$ cm^{-2} (extended source).

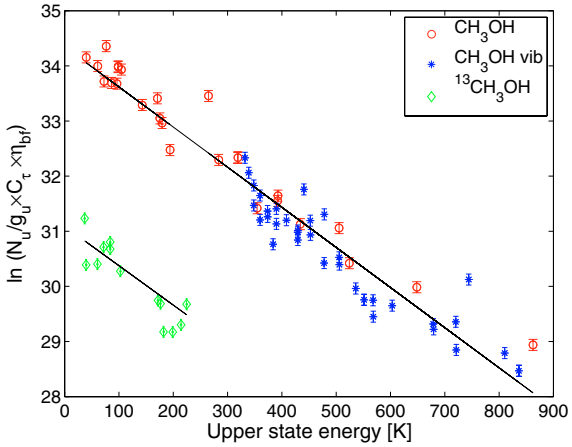

Fig. 45. CH_3OH forward model producing $T_{ROT} = 136^{+3}_{-4}$ K, $N = (1.3 \pm 0.1) \times 10^{18}$ cm^{-2} and a source size of $6''^{+0.1}_{-0.3}$. The $^{13}CH_3OH$ forward model use the rotation temperature and source size obtained from CH_3OH.

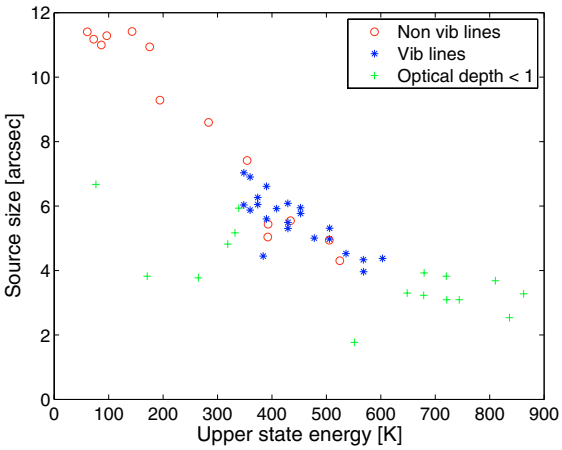

Fig. 46. Source size variation with energy for CH_3OH (no opacity corrections). The low-energy transitions have larger source sizes than higher-energy transitions. Note that all lines with an optical depth less than one, fall below the general trend of decreasing source size with higher energy, since Eq. (14) is only valid for optically thick lines.

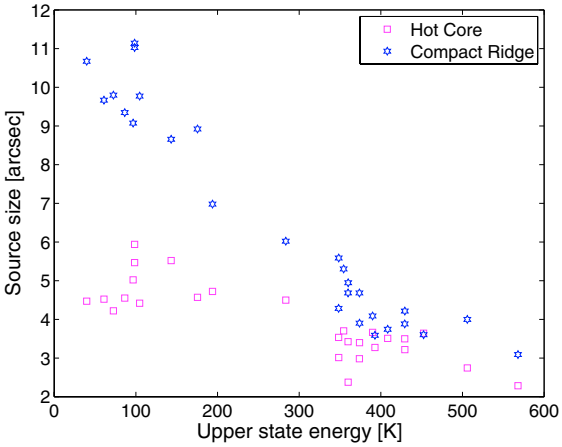

Fig. 47. Source size variation with energy for two components of CH_3OH with no opacity correction.

Table 5. Summary of all detected species.

Species	Number of lines	Upper state energy range [K]	$\int T_A^* d\upsilon$ [K km s^{-1}]
CH_3OCH_3	47	106–448	18.3
SO_2	42	75–737	239.9
$^{34}SO_2$	5	79–457	2.6
SO	5	71–201	181.5
^{33}SO	3	191–199	6.5
^{34}SO	2	191–197	15.6
CH_3OH υ_t=1	42	332–836	
CH_3OH	34	38–863	108.6
$^{13}CH_3OH$	21	37–499	6.8
$^{13}CH_3OH$ υ_t=1	2	373–670	
CH_3CN	17	410–1012	9.3
NO	12	84–232	11.1
CN	8	54	8.5
H_2CS	5	138–343	1.7
H_2CO	3	106–133	38.5
$H_2^{13}CO$	1	130	0.6
HDCO	3	114–141	2.8
OCS	3	604–658	1.3
o-H_2O	1	61	320.3
p-H_2O	1	867	2.2
o-$H_2^{17}O$	1	61	9.4
o-$H_2^{18}O$	2	60–430	16.2
HDO	1	66	10.7
HC_3N	2	648–799	0.6
CO	1	83	1 100
^{13}CO	1	79	174.3
$C^{17}O$	1	81	6.0
$C^{18}O$	1	79	24.3
C	1	24	38.7
NH_3	1	27	20.6
$^{15}NH_3$	1	27	0.7
HNC	1	91	10.7
N_2H^+	1	94	1.5
H_2S	1	166	4.4
CS	1	129	24
^{13}CS	1	173	v blend
SiO	1	190	17.6
^{29}SiO	1	187	1.4
^{30}SiO	1	185	0.5
HCS^+	1	186	v blend
NS	1	442	v blend
U-line	28		9.1
T-line	36		7.2
No. of species	38		
No. of lines	344		
Total $\int T_A^* d\upsilon$			2455

Table 6. Isotopologue abundance ratios from our survey, or from the literature, as compared to terrestrial values. The molecular abundance O/S ratios are also included.

	$[^{12}C/^{13}C]$	$[^{32}S/^{34}S]$	$[^{34}S/^{33}S]$	$[^{18}O/^{17}O]$	$[^{16}O/^{18}O]$	[D/H]	[O/S]	$[^{14}N/^{15}N]$	$[^{28}Si/^{29}Si]$
This survey	57 ± 14^a	21 ± 6^b–23 ± 7^c	4.9^d	3.6^e		0.001^f–0.03^g	15^h–20^i		
Terrestrial	89^j	22.5^j	5.5^j	5.5^k			35^v	273^l	19.6^m
K88[j]	47^{+6}_{-5}	$20.2^{+2.6}_{-2.1}$	$5.7^{+0.8}_{-0.6}$						
W&R94[n]	77 ± 7	~ 22		3.2 ± 0.2	560 ± 25			450 ± 22	
C96[o]	75 ± 21	35 ± 10	7.53 ± 0.45						
B01[p]	65.0 ± 9.2			4.15 ± 0.59					
P81b[q]				3.9 ± 0.2					
Various surveys	43 ± 7^r			4.17 ± 0.26^s	330 ± 69^t	2×10^{-5} [u]			16.9 ± 2.0^m

[a] From $^{12}CH_3OH/^{13}CH_3OH$. [b] From $^{32}SO/^{34}SO$. [c] From $^{32}SO_2/^{34}SO_2$. [d] From $^{34}SO/^{33}SO$. [e] From $C^{18}O/C^{17}O$. [f] From $HDO/H_2^{17}O$ Hot Core. [g] From $HDO/H_2^{17}O$ Compact Ridge. [h] From $H_2^{13}CO/H_2^{12}CS$ CR. [i] From $H_2^{17}O/H_2S$ LVF. [j] Kahane et al. (1988), the envelope of IRC+10216. [k] Blake et al. (1987). [l] Ho & Townes (1983). [m] Penzias (1981a). [n] Wilson & Rood (1994) and references therein, local ISM. [o] Chin et al. (1996), towards Orion KL. [p] Bensch et al. (2001), towards ρ Ophiuchi Molecular Cloud. [q] Penzias (1981b), towards Orion A. [r] Savage et al. (2002), towards Orion A using CN and ^{13}CN. [s] Wouterloot et al. (2005), towards ρ Ophiuchi Molecular Cloud, value from LTE column densities. [t] Olofsson (2003), from $S^{18}O$ observations of molecular cloud cores. [u] Neufeld et al. (2006). [v] Standard abundances, Grevesse et al. (1996).

Table 7. H_2O and isotopologue parameters and derived column densities.

Species	Comp[a]	υ_{LSR} [km s^{-1}]	$\Delta\upsilon$ [km s^{-1}]	T_A^* [K]	T_k [K]	Size ["]	N^b	τ cm^{-2}]	$N^c_{\tau\,corr}$ cm^{-2}]	N^d_{ISO} [cm^{-2}]
o-$H_2^{16}O$	Total				72	(15)[e]		$\sim 1100^f$		1.7×10^{18}
	CR				115	(6)[e]		$\sim 860^f$		5.6×10^{17}
	LVF				72	(15)[e]		$\sim 1900^f$		8.7×10^{17}
	HVF	5.3	67.1	2.452	72	70	8.7×10^{14}	$\sim 910^f$	8.0×10^{17}	8.8×10^{17}
p-$H_2^{16}O$	HC	4.4	12.0	0.181	200	10	1.2×10^{19}	0.3^g		
o-$H_2^{17}O$	Total				72	15	8.6×10^{14}	0.9^f	1.3×10^{15}	
	CR	9.9	5.0	0.076	115	6	3.2×10^{14}	0.7^f	4.4×10^{14}	
	LVF	8.7	18.0	0.214	72	15	3.5×10^{14}	1.5^f	6.7×10^{14}	
	HVF	13.4	30.1	0.179	72	15	4.9×10^{14}	0.7^f	6.8×10^{14}	
o-$H_2^{18}O$	Total				72	15	1.4×10^{15}	3.4^f	5.0×10^{15}	5.0×10^{15}
	CR	10.1	5.0	0.145	115	6	6.2×10^{14}	2.6^f	1.8×10^{15}	1.7×10^{15}
	LVF	10.5	18.0	0.275	72	15	4.6×10^{14}	5.9^f	2.7×10^{15}	2.6×10^{15}
	HVF	13.4	33.4	0.298	72	15	9.3×10^{14}	2.8^f	2.8×10^{15}	2.7×10^{15}
HDO	Total				72	15	9.1×10^{15}	$\sim 1.5^g$		
	CR	8.5	4.6	0.459	115	6	1.8×10^{16}	$\sim 3^g$		
	LVF	11.8	18.0	0.273	72	15	4.5×10^{15}	$\sim 0.3^g$		
	HC	2.2	13.4	0.216	200	10	1.5×10^{16}	$\sim 0.5^g$		

[a] Total = the total integrated intensity is used, CR = Compact Ridge, LVF = Low Velocity Flow, HVF = High Velocity Flow, HC = Hot Core.
[b] Corrected for beam-filling.
[c] Corrected for beam-filling, and for optical depth with factor $\tau/(1 - e^{-\tau})$.
[d] Column calculated from isotopologue *o*-$H_2^{17}O$, beam-filling and optical depth corrected.
[e] Size from isotopologues. The full LVF *o*-$H_2^{16}O$ emission may have a larger extent.
[f] Calculated from the ratio of $H_2^{18}O$ and $H_2^{17}O$ column densities.
[g] Calculated with Eq. (15).

Table 8. CO and isotopologue parameters and derived column densities.

Species	Comp[a]	$\upsilon_{\rm LSR}$	$\Delta\upsilon$	$T_{\rm A}^*$ [K]	$\int T_{\rm A}^* {\rm d}\upsilon$ [K km s^{-1}]	$T_{\rm k}$ [K]	Size [″]	N [cm^{-2}]	τ	$N_{\rm ISO}(\rm C^{17}O)$ [cm^{-2}]	$N_{\rm ISO}(\rm C^{18}O)$	$N_{\rm ISO}(^{13}\rm CO)$
CO	PDR[b]					100	...			1.6×10^{18}	1.5×10^{18}	1.2×10^{18}
	LVF					100	(30)[d]			2.5×10^{19}	2.2×10^{19}	2.3×10^{19}
	HVF					100	(70)[d]					2.2×10^{18}
^{13}CO	N[c]	8.1	4.8	21.6	109.9	100	...	5.7×10^{16}		5.4×10^{16}	4.9×10^{16}	
	LVF	7.8	18.0	2.18	41.6	100	30	3.9×10^{17}		4.2×10^{17}	3.7×10^{17}	
	HVF	6.7	48.7	0.470	24.2	100	70	5.2×10^{16}				
$\rm C^{17}O$	N[c]	8.8	4.2	1.11	4.95	100	...	2.5×10^{15}	0.07			
	LVF	9.9	18.0	0.116	2.21	100	30	2.0×10^{16}	0.1			
$\rm C^{18}O$	N[c]	8.7	4.2	3.81	17.0	100	...	8.9×10^{15}	0.3	9.8×10^{15}		
	LVF	7.8	18.0	0.367	7.00	100	30	6.7×10^{16}	0.3	7.7×10^{16}		
$\rm H_2$	PDR[b]						...			2.0×10^{22}	1.8×10^{22}	1.5×10^{22}
	ER[b]						...			2.0×10^{22}	1.8×10^{22}	1.5×10^{22}
	LVF						(30)[d]			3.2×10^{23}	2.8×10^{23}	2.3×10^{23}
	HVF						(70)[d]					3.9×10^{22}

[a] N = Narrow, LVF = Low Velocity Flow, HVF = High Velocity Flow.
[b] This is half of the column density obtained from the narrow components of the isotopolouges, since CO narrow component only has emission from the PDR, while the isotopologues have ~equal emission from PDR and ER (as discussed in W06).
[c] Consists of approximately equal emission from PDR and ER.
[d] Size from CO isotopologues. The size of the full LVF CO emission is larger than the isotopologues and calculated to be 45″.

Table 9. SO_2 parameters[a].

ν_{ul} [MHz]	$\Delta\nu_p$ [MHz]	$\Delta\nu_g$ [MHz]	Transition $J_{Ka,Kc}$	E_u [K]	A_{ul} [s^{-1}]	T_A^*(peak) [mK]	Ampl. [mK]	Width [km s^{-1}]	$\int T_A^* d\upsilon$ [K km s^{-1}]	Note
491934.7			$7_{4,4}-6_{3,3}$	65.0	9.49e-4					blend HDCO
541750.9	0.9		$14_{3,11}-13_{2,12}$	119.0	6.31e-4	695			15.80	
		0.0					143	5.0		3G: CR
		-0.1					266	18.0		3G: LVF
		3.2					301	34.9		3G: HVF
541810.6			$30_{6,24}-30_{5,25}$	516.7	1.34e-3					weak
543413.5	−2.5	−0.5	$29_{2,28}-28_{1,27}$	401.5	1.64e-3	457	411	25.5	10.70	blend CH_3OH & SO_2
543467.7			$37_{3,35}-37_{2,36}$	664.0	7.77e-4					v blend CH_3OH & SO_2
545318.5	3.5	5.5	$37_{6,32}-37_{5,33}$	736.9	1.43e-3	66	41	17.5	0.72	
545517.3	−0.7	−2.7	$35_{6,30}-35_{5,31}$	669.3	1.42e-3	99	63	16.5	1.07	
546579.8	−1.2	2.8	$19_{3,17}-18_{2,16}$	197.0	7.40e-4	546	488	25.1	12.90	
547802.2	1.2	−1.8	$28_{6,22}-28_{5,23}$	462.2	1.36e-3	160	136	16.8	2.41	
548734.3	−3.7	−2.7	$31_{6,26}-31_{5,27}$	545.3	1.40e-3	102	87	11.3	1.02	
548838.9			$40_{4,36}-39_{5,35}$	808.3	5.52e-4					blend $C^{18}O$
549303.3	3.3	11.3	$10_{4,6}-9_{3,7}$	89.8	1.07e-3	890	857	32.8	29.20	blend CH_3OH, $^{13}CH_3OH$ & ^{34}SO
549566.4	15.4	5.4	$30_{1,29}-29_{2,28}$	427.9	1.73e-3	455	369	24.7	9.38	blend CH_3OCH_3
550946.7			$29_{6,24}-29_{5,25}$	488.9	1.40e-3					blend ^{13}CO
551622.9	−3.1		$38_{2,36}-38_{1,37}$	697.7	7.94e-4	43			0.31	weak
552069.4	−11.6		$34_{1,33}-34_{0,34}$	542.8	4.43e-4					blend $H_2^{17}O$, SO_2
552078.9	−2.1	0.0	$26_{6,20}-26_{5,21}$	411.4	1.37e-3	223	197	17.1	3.33	blend $H_2^{17}O$, SO_2
553164.9	2.9	2.9	$27_{6,22}-27_{5,23}$	436.3	1.39e-3	224	225	22.5		v blend & 3G CH_3OH;
554212.8	7.8	1.8	$31_{1,31}-30_{0,30}$	431.5	2.34e-3	545	490	21.4	10.90	blend CH_3OH
555121.5	−2.5		$24_{6,18}-24_{5,19}$	364.4	1.37e-3	264			4.20	blend $(CH_3)_2O$
555204.1	−6.9		$25_{6,20}-25_{5,21}$	387.4	1-38e-3	223	188	19.9	3.75	
555666.3	0.7	−0.7	$5_{5,1}-4_{4,0}$	75.1	2.18e-3	742	677	28.1	20.00	blend CH_3OCH_3
556959.9			$23_{6,18}-23_{5,19}$	342.2	1.37e-3					blend H_2O
557283.2	−3.8	0.2	$22_{6,16}-22_{5,17}$	321.0	1.36e-3	303	271	22.9	6.72	
558101.2			$15_{9,7}-16_{8,8}$	308.6	1.54e-3					blend SO
558390.9	−1.1	−1.1	$21_{6,16}-21_{5,17}$	300.8	1.35e-3	335	290	20.0	5.55	blend & 3G CH_3OH;
558555.8	4.8	9.2	$16_{3,13}-16_{0,16}$	147.8	3.90e-5	115	80	23.8	1.93	
558812.5	−2.5	2.5	$20_{6,14}-20_{5,15}$	281.4	1.34e-3	327	291	23.7	7.17	
559500.4	−0.6	−0.6	$19_{6,14}-19_{5,15}$	263.0	1.32e-3	352	298	23.1	7.31	
559882.1	−1.9	0.1	$18_{6,12}-18_{5,13}$	245.5	1.31e-3	331	302	21.7	6.59	
560318.9	−1.1	−1.1	$17_{6,12}-17_{5,13}$	229.0	1.29e-3	393	376	18.1		v blend & 2G CH_3OH;
560613.5	−1.5	1.5	$16_{6,10}-16_{5,11}$	213.3	1.27e-3	354	342	23.4	8.52	blend $^{34}SO_2$
560891.0	−3.0		$15_{6,10}-15_{5,11}$	198.6	1.25 e-3	378	325	22.6	7.68	
561094.8	−1.2	−1.2	$14_{6,8}-14_{5,9}$	184.8	1.22e-3	326	304	23.0	7.30	
561265.6	−0.4	1.4	$13_{6,8}-13_{5,9}$	171.9	1.19e-3	467	382	23.2	9.26	blend CH_3OH
561361.4			$21_{3,19}-20_{2,18}$	234.7	8.31e-4	522				blend SO_2
561392.9	0.9		$12_{6,6}-12_{5,7}$	160.0	1.14e-3	436				blend CH_3OH & SO_2
561490.5	0.5		$11_{6,6}-11_{5,7}$	149.0	1.09e-3	383				blend SO_2
561560.3	−1.7		$10_{6,4}-10_{5,5}$	138.8	1.02e-3	402				v blend SO_2
561608.6	−0.4		$9_{6,4}-9_{5,5}$	129.7	9.37e-4	502				v blend SO_2
561639.3	−0.7		$8_{6,2}-8_{5,3}$	121.4	8.18e-3	564				v blend SO_2
561656.7	16.7		$7_{6,2}-7_{5,3}$	114.0	6.50e-4	547				v blend SO_2
561664.2	24.2		$6_{6,0}-6_{5,1}$	107.6	3.99e-4	547				v blend SO_2
567592.7	−1.3		$11_{4,8}-10_{3,37}$	100.0	1.12e-3	822			16.80	
571532.6	−7.4	−1.4	$32_{2,30}-31_{3,29}$	504.3	1.34e-3	465	171	21.3		blend & 2G SO_2;
571553.3	−2.7	0.3	$32_{0,32}-31_{1,31}$	459.0	2.58 e-3	465	343	21.2	11.30	blend & 2 G SO_2;
574587.8	−7.2	−3.2	$23_{3,21}-22_{2,20}$	276.0	9.46e-4	276	248	21.4	5.47	
574807.3	−2.7	3.3	$6_{5,1}-5_{4,2}$	80.7	2.07e-3	478	410	23.4	9.97	blend $^{34}SO_2$
576042.1	−5.9	−4.9	$31_{2,30}-30_{1,29}$	455.6	2.03e-3	200	165	16.0	2.72	
Total No.	49									

[a] ν_{ul} = rest frequency of the transition $u \rightarrow l$; $\Delta\nu_p$ = the difference between freq and the observed frequency at the peak temperature; $\Delta\nu_g$ = the difference between freq and the frequency of the Gaussian fit; Transition = the quantum numbers for the transition; E_u = the upper state energy; A_{ul} = the Einstein A-coefficient; T_A^*(peak) = the observed peak temperature of the transition; Ampl. = the peak temperature of the Gaussian fit; Width = the width of the transition from the Gaussian fit; $\int T_A^* d\upsilon$ = the integrated intensity from the observed spectra; Note: 2G or 3G denotes a two- or three-component Gaussian fit, v blend denotes a visible blend, Total No. = the total number of transitions of the molecule in the table. All these lines are also marked in the spectra shown in Paper I Appendix A, and listed in the online Table of Paper I. These total numbers of lines include not visible blends, which are not counted in Table 5.

Table 10. $^{34}SO_2$ parameters[a].

ν_{ul} [MHz]	Δv_p [MHz]	Δv_g [MHz]	Transition $J_{Ka,Kc}$	E_u [K]	A_{ul} [s^{-1}]	T_A^*(peak) [mK]	Ampl. [mK]	Width [km s^{-1}]	$\int T_A^* dv$ [K km s^{-1}]	Note
542097.7	−0.3	4.7	$11_{6,6}-11_{5,7}$	145.8	9.83e-4		102	16.0		from 3G CH_3OH
542177.4			$10_{6,4}-10_{5,5}$	135.7	9.23e-4					
542233.5			$9_{6,4}-9_{5,5}$	126.5	8.44e-4					weak
542270.1			$8_{6,2}-8_{5,3}$	118.3	7.37e-4					weak
542291.7			$7_{6,2}-7_{5,3}$	110.9	5.86e-4					weak
542302.3			$6_{6,0}-6_{5,1}$	104.5	3.60e-4					weak
547613.5			$21_{3,19}-20_{2,18}$	233.5	7.87e-4					blend $H_2^{18}O$
551767.4			$31_{1,31}-30_{0,30}$	429.7	2.32e-3					blend CH_3OH, weak
554708.2		−6.8	$11_{4,8}-10_{3,7}$	98.5	1.04e-3	141	123	20.1		v blend ^{13}CS; from 2G ^{13}CS
558717.5	2.5	3.5	$6_{5,1}-5_{4,2}$	78.5	1.90e-3	98	83	19.5	1.67	
560590.2			$23_{3,21}-22_{2,20}$	274.7	9.02e-4					blend SO_2
569091.6	−3.4		$32_{0,32}-31_{1,31}$	457.0	2.55e-3	74			0.33	weak
573527.3	2.3		$25_{3,23}-24_{2,22}$	319.5	1.05e-3	92			0.68	weak
574797.9			$12_{4,8}-11_{3,9}$	109.5	1.10e-3					blend SO_2
Total No.	14									

[a] Notation as in Table 9.

Table 11. SO parameters[a].

ν_{ul} [MHz]	Δv_p [MHz]	Δv_g [MHz]	Transition N_J	E_u [K]	A_{ul} [s^{-1}]	T_A^*(peak) [mK]	Ampl. [mK]	Width [km s^{-1}]	$\int T_A^* dv$ [K km s^{-1}]	Note
487708.5	0.5	−1.5	7_7-6_7	71.0	1.70e-5	206	178	13.8	2.67	
558087.7	2.7		$13_{12}-12_{11}$	194.4	2.28e-3	2094			59.00	blend SO_2
		2.7					160	4.7		3G; CR
		0.7					759	18.0		3G; LVF
		2.7					1178	35.5		3G; HVF
559319.8	3.8		$13_{13}-12_{12}$	201.1	2.30e-3	1996			56.90	
		3.8					165	5.0		3G; CR
		−0.2					674	18.0		3G; LVF
		4.8					1163	35.3		3G; HVF
560178.7	2.7		$13_{14}-12_{13}$	192.7	2.32e-3	2168			61.70	
		2.7					213	5.0		3G; CR
		0.7					666	18.0		3G; LVF
		1.7					1285	35.6		3G; HVF
568741.6	9.6	1.6	9_9-8_9	106.1	1.90e-5	105	78	15.9	1.24	
Total No.	5									

[a] Notation as in Table 9.

Table 12. ^{33}SO parameters[a].

ν_{ul} [MHz]	Δv_p [MHz]	Δv_g [MHz]	Transition N_J	E_u [K]	A_{ul} [s^{-1}]	T_A^*(peak) [mK]	Ampl. [mK]	Width [km s^{-1}]	$\int T_A^* dv$ [K km s^{-1}]	Note
552429.8	−2.2	1.8	$12_{13}-11_{12}$	192.5	2.18 e-3	138	112	20.3	2.41	
553681.3	−6.7	−2.7	$13_{13}-12_{12}$	199.2	2.20e-3	113	85	17.0		Blend 2 U-lines & CH_3CN
554555.6	−3.4	−3.4	$14_{13}-13_{12}$	190.8	2.24e-3	110	100	20.5	2.06	
Total No.	3									

[a] Notation as in Table 9.

Table 13. ^{34}SO parameters[a].

ν_{ul} [MHz]	Δv_p [MHz]	Δv_g [MHz]	Transition N_J	E_u [K]	A_{ul} [s^{-1}]	T_A^*(peak) [mK]	Ampl. [mK]	Width [km s^{-1}]	$\int T_A^* d\upsilon$ [K km s^{-1}]	Note
547119.6	−5.4	−2.4	$12_{13}-11_{12}$	190.7	2.15e-3	380	326	27.6	9.35	
548389.8	−2.2	0.8	$13_{13}-12_{12}$	197.4	2.17 e-3	324	304	22.8	7.31	
549278.7			$14_{13}-13_{12}$	189.0	2.19e-3					blend CH_3OH, SO_2 & $^{13}CH_3OH$
561700.4			9_9-9_8	104.3	1.83e-5					blend SO_2 & $C^{17}O$
Total No.	4									

[a] Notation as in Table 9.

Table 14. SiO and isotopologue parameters[a].

Species	ν_{ul} [MHz]	Δv_p [MHz]	Δv_g [MHz]	Transition J	E_u [K]	A_{ul} [s^{-1}]	T_A^*(peak) [mK]	Ampl. [mK]	Width [km s^{-1}]	$\int T_A^* d\upsilon$ [K km s^{-1}]	Note
SiO	564249.2	−2.8		13−12	189.6	9.66e-3	729			17.60	
			2.2					391	18.0		2G; LVF
			−1.8					315	31.5		2G; HVF
^{29}SiO	557184.4	2.4	1.4	13−12	187.2	9.31e-3	82	72	21.2	1.39	blend H_2O
^{30}SiO	550605.2	−9.8	−5.8	13−12	185.0	8.98e-3	71	59	7.5	0.45	?
Total No.	3										

[a] Notation as in Table 9.

Table 15. H_2S parameters[a].

ν_{ul} [MHz]	Δv_p [MHz]	Δv_g [MHz]	Transition J_{K_a,K_c}	E_u [K]	A_{ul} [s^{-1}]	T_A^*(peak) [mK]	Ampl. [mK]	Width [km s^{-1}]	$\int T_A^* d\upsilon$ [K km s^{-1}]	Note
567079.6			$6_{4,2}-6_{3,3}$	540.2	6.52e-4					blend NO
568050.7	−7.3		$3_{3,1}-3_{2,2}$	165.9	3.32e-4	247			4.41	
		−7.3					106	7.5		2G; HC
		−0.3					145	24.4		2G; Plateau
Total No.	2									

[a] Notation as in Table 9.

Table 16. CH_3CN parameters[a].

ν_{ul} [MHz]	$\Delta\nu_p$ [MHz]	$\Delta\nu_g$ [MHz]	Transition J_K	E_u [K]	A_{ul} [s^{-1}]	T_A^*(peak) [mK]	Ampl. [mK]	Width [km s^{-1}]	$\int T_A^* d\upsilon$ [K km s^{-1}]	Note
550671.7			30_9-29_9	984.6	1.34e-2					blend CH_3OH
550850.0	−6.0		30_8-29_8	864.2	1.37e-2					v blend ^{13}CO
551007.4	0.4		30_7-29_7	758.0	1.39e-2					v blend ^{13}CO
551143.9	−5.1	−5.1	30_6-29_6	665.8	1.41e-2	145	125	13.2		v blend NO; from 5G CH_3CN, NO & CH_3OH
551259.6		−8.4	30_5-29_5	587.8	1.43e-2	159	160	10.6		v blend CH_3OCH_3; from 2G CH_3OCH_3
551354.2	−1.8	−4.8	30_4-29_4	524.0	1.45e-2	144	112	9.4	1.09	
551427.9	−1.1	−4.1	30_3-29_3	474.3	1.46e-2	221	198	9.9	1.80	
551480.6	−2.4	−4.4	30_2-29_2	438.8	1.47e-2	210	173	9.0	1.43	
551512.2			30_1-29_1	417.5	1.47e-2					v blend NO
551522.7			30_0-29_0	410.4	1.48e-2					v blend NO
552646.6*	−1.4		30_1-29_1 $\ell=+1$	930.2	1.48e-2					weak
552970.8*	−3.2		30_0-29_0 $\ell=\pm1$	936.7	1.49e-2					weak
553007.8*	−6.2		30_2-29_2 $\ell=-1$	991.9	1.48e-2					weak
553029.1*	−0.9		30_1-29_1 $\ell=-1$	957.2	1.49e-2					weak
553240.3*	−2.7		30_3-29_3 $\ell=+1$	961.1	1.48e-2					weak
553362.2*			30_2-29_2 $\ell=+1$	938.9	1.48e-2					weak & narrow
553707.6				931.8						weak
568999.3	−1.7		31_9-30_9	1011.9	1.49e-2	81				weak
569486.9	−3.1	−5.1	31_6-30_6	693.2	1.57e-2	144	98	7.8	0.77	strange shape
569606.3	−1.7	−3.7	31_5-30_5	615.2	1.58e-2	91	77	3.3	0.25	
569704.0	−6.0	−5.0	31_4-30_4	551.3	1.60e-2	130	124	3.6	0.45	
569780.1	−6.9	−6.9	31_3-30_3	501.6	1.61e-2	241	165	8.4	1.26	
569834.5	−1.5	−3.5	31_2-30_2	466.2	1.62e-2	126	126	5.8	0.71	
569867.1	−4.9	−2.9	31_1-30_1	444.9	1.63e-2	159	151	5.1	0.66	blend CH_3CN
569878.0	−3.0	−2.0	31_0-30_0	437.8	1.63e-2	220	208	5.5	0.95	blend CH_3CN
Total No.	25									

[a] Notation as in Table 9. * Vibrationally excited transition, $v_8 = 1$.

Table 17. NH_3 and $^{15}NH_3$ parameters[a].

Species	ν_{ul} [MHz]	$\Delta\nu_p$ [MHz]	$\Delta\nu_g$ [MHz]	Transition J_K	E_u [K]	A_{ul} [s^{-1}]	T_A^*(peak) [mK]	Ampl. [mK]	Width [km s^{-1}]	$\int T_A^* d\upsilon$ [K km s^{-1}]	Note
NH_3	572498.2	1.2		1_0-0_0	27.5	1.61e-3	2409			20.60	
			1.2					1704	4.9		2G fit; CR
			2.2					694	16.2		2G fit; HC
$^{15}NH_3$	572112.8	–0.2		1_0-0_0	27.5	1.57e-3	167	150	6.7	1.02	
Total No.	2										

[a] Notation as in Table 9.

Table 18. HC_3N parameters[a].

ν_{ul} [MHz]	$\Delta\nu_p$ [MHz]	$\Delta\nu_g$ [MHz]	Transition J	E_u [K]	A_{ul} [s^{-1}]	T_A^*(peak) [mK]	Ampl. [mK]	Width [km s^{-1}]	$\int T_A^* d\upsilon$ [K km s^{-1}]	Note
490955.7	−6.3	−5.3	54–53	648.2	9.50e-3	91	86	6.4	0.53	blend CH_3OH
545417.1	−3.9		60–59	798.7	1.30e-2	70	57	10.3	0.60	
Total No.	2									

[a] Notation as in Table 9.

Table 19. OCS parameters[a].

ν_{ul} [MHz]	$\Delta\nu_p$ [MHz]	$\Delta\nu_g$ [MHz]	Transition J	E_u [K]	A_{ul} [s^{-1}]	T_A^*(peak) [mK]	Ampl. [mK]	Width [km s^{-1}]	$\int T_A^* d\upsilon$ [K km s^{-1}]	Note
546859.8	−3.2		45−44	603.9	4.81e-4	67			0.31	blend SO_2, $^{13}CH_3OH$
558990.5	−4.5	−2.5	46−45	630.7	5.14e-4	88	88	6.5	0.58	
571119.7	−2.3		47−46	658.1	5.49e-4	68			0.41	?
Total No.	3									

[a] Notation as in Table 9.

Table 20. CH_3OH parameters[a].

ν_{ul} [MHz]	$\Delta\nu_p$ [MHz]	$\Delta\nu_g$ [MHz]	Transition J_{K_a,K_c}	E_u [K]	A_{ul} [s^{-1}]	T_A^*(peak) [mK]	Ampl. [mK]	Width [km s^{-1}]	$\int T_A^* d\upsilon$ [K km s^{-1}]	Note
486940.9	0.9		$4_{2,3}-4_{1,4}$ A	60.9	5.45e-4	884			5.13	
		0.9					635	3.8		2G; CR
		−0.1					241	10.1		2G; HC
487531.9	0.9		$10_{1,9}-9_{1,8}$ A	143.3	5.15e-4	855			4.85	
		0.9					509	3.3		2G; CR
		−0.1					359	8.1		2G; HC
488945.5*	−0.5	−1.0	$7_{2,5}-8_{3,5}$ E	429.4	5.79e-4	191	188	5.0	1.01	
489037.0	0.0		$5_{2,4}-5_{1,5}$ A	72.5	5.70e-4	849			4.36	
		0.0					652	3.7		2G; CR
		−2.0					210	8.5		2G; HC
489224.3	0.3	0.3	$23_{1,23}-22_{2,20}$ A	648.5	1.92e-4	74	69	2.9	0.21	
490960.0	−2.0		$21_{3,19}-20_{4,17}$ E	598.5	2.27e-4					blend HC_3N
491550.9	0.1		$6_{2,5}-6_{1,6}$ A	86.4	5.87e-4	821			4.76	
		−0.1					593	3.8		2G; CR
		−1.1					244	9.5		2G; HC
492278.6	0.0		$4_{1,4}-3_{0,3}$ E	37.6	7.65e-4	927	920	4.4	2.58	
542000.9	0.9		$6_{3,4}-5_{2,3}$ A	98.5	7.93e-4	1261			6.89	
		0.9					817	3.2		2G; CR
		0.9					413	9.3		2G; HC
542081.9	−0.1		$6_{3,3}-5_{2,4}$ A	98.5	7.94e-4	1230				
		−0.1					834	3.5		from 3G $^{34}SO_2$; CR
		1.9					350	9.0		from 3G $^{34}SO_2$; HC
542163.0*	−2.0	−4.0	$20_{1,20}-20_{2,19}$	810.4	7.35e-4	91	68	6.0	0.35	
543076.1	0.1		$8_{0,8}-7_{1,7}$ E	96.6	4.54e-4	856			4.75	
		0.1					614	3.8		2G; CR
		−0.9					227	9.9		2G; HC
543457.3*	−2.7		$19_{1,19}-19_{2,18}$ A	764.3	7.49e-4					v blend SO_2
544653.1*	−4.9		$18_{1,18}-18_{2,17}$ A	720.4	7.62e-4	98			0.55	?
544820.5	−0.5	−1.5	$5_{5,1}-6_{4,2}$ E	170.9	2.60e-5	98	91	3.4	0.32	
545034.8	0.8		$26_{3,23}26_{2,24}$ E	862.5	9.00e-4	72			0.31	
545755.6*	−6.4	−4.4	$17_{1,17}-17_{2,16}$ A	678.8	7.75e-4	70	70	5.6	0.50	
546226.8*	−1.2		$11_{3,9}-12_{4,9}$ E	570.1	8.26e-4					v blend CH_3OH
546239.0	−1.0		$17_{2,16}-17_{1,17}$ A	392.5	7.38e-4	212			2.13	blend CH_3OH
547698.9*			$15_{1,15}-15_{2,14}$ A	602.6	7.97e-4					blend $H_2^{18}O$
548548.7*	−1.3		$14_{1,14}-14_{2,13}$ A	568.0	8.07e-4	126			0.63	
		−2.3					64	2.7		2G; CR
		−2.3					61	7.5		2G; HC
549322.8*			$13_{1,13}-13_{2,12}$ A	535.6	8.16e-4					blend SO_2, & $^{13}CH_3OH$
550025.2*	−4.8	−2.8	$12_{1,12}-12_{2,11}$ A	505.6	8.24e-4	166	157	6.9	1.15	
550659.3*	−2.7	−3.7	$11_{1,11}-11_{1,11}$ A	477.9	8.31e-4	168	153	5.9	0.94	blend CH_3CN

[a] Notation as in Table 9. * Vibrationally excited transition, $v_t = 1$.

Table 20. continued.

ν_{ul} [MHz]	$\Delta\nu_p$ [MHz]	$\Delta\nu_g$ [MHz]	Transition J_{K_a,K_c}	E_u [K]	A_{ul} [s^{-1}]	T_A^*(peak) [mK]	Ampl. [mK]	Width [km s^{-1}]	$\int T_A^* d\upsilon$ [K km s^{-1}]	Note
551228.6*	−1.4		$10_{1,10}-10_{2,9}$ A	452.4	8.36e-4	237				blend CH_3OCH_3, NO, & CH_3CN
							90	3.3		5G CH_3CN,
							152	9.4		NO & CH_3OH
551736.2*	−0.8		$9_{1,9}-9_{2,8}$ A	429.3	8.40e-4	248			1.33	
		−0.8					101	2.5		2G; CR
		−1.8					143	8.1		2G; HC
551968.8		−2.2	$6_{6,1}-7_{5,3}$ E	227.5	2.10e-5					v blend $H_2^{17}O$
552184.8*	−1.2		$8_{1,8}-8_{2,7}$ A	408.5	8.41e-4	235			1.46	
		−1.2					94	2.3		2G; CR
		−1.2					144	8.4		2G; HC
552577.2*	−0.8		$7_{1,7}-7_{2,6}$ A	390.0	8.40e-4	293			1.58	
		−0.8					110	2.2		2G; CR
		−0.8					161	7.9		2G; HC
552915.4*	0.4		$6_{1,6}-6_{2,5}$ A	373.8	8.35e-4	263			1.32	
		−0.6					147	3.2		2G; CR
		−0.6					104	7.6		2G; HC
553146.3	0.3		$8_{1,7}-7_{0,7}$ E	104.6	4.63e-4	1036			6.35	blend SO_2
		0.3					640	3.3		from 3G SO_2
		−3.7					228	9.4		from 3G SO_2
553201.6*	−1.4		$5_{1,5}-5_{2,4}$ A	359.9	8.22e-4	319			1.48	
		−0.4					132	1.9		2G; CR
		−1.4					171	7.4		2G; HC
553437.5*	−0.5		$4_{1,4}-4_{2,3}$ A	348.4	7.96e-4	244			1.00	
		−0.5					123	1.6		2G; CR
		−2.5					146	5.3		2G; HC
553570.9	−2.1		$18_{2,17}-18_{1,18}$ A	434.2	7.56e-4	206			1.35	
		−2.1					39	3.0		2G;CR
		−3.1					149	8.0		2G; HC
553624.5*	−1.5		$3_{1,3}-3_{2,2}$ A	339.1	7.40e-4	236			1.20	
		−1.5					128	2.5		2G; CR
		−3.5					116	8.8		2G; HC
553763.7*	−1.3		$2_{1,2}-2_{2,1}$ A	332.2	5.93e-4	179			1.07	
		−1.3					106	3.5		2G; CR
		−3.3					78	8.6		2G; HC
554052.7*	−4.3		$2_{1,1}-2_{2,0}$ A	332.2	5.94e-4	549			3.19	blend CH_3OH
554055.5	−1.5		$12_{1,11}-11_{2,9}$ E	202.1	3.13e-4					blend CH_3OH
554202.9*	−1.1		$3_{1,2}-3_{2,1}$ A	339.2	7.41e-4					v blend SO_2
554402.5*	−1.5		$4_{1,3}-4_{2,2}$ A	348.4	7.99e-4	331			1.30	
		−1.5					209	2.8		2G; CR
		−4.5					106	10.6		2G; HC
554650.9*	−1.1		$5_{1,4}-5_{2,3}$ A	360.0	8.26e-4	231			0.95	
		−0.6					102	2.7		2G; CR
		−2.6					135	6.8		2G; HC
554947.4*	0.4	−1.6	$6_{1,5}-6_{2,4}$ A	373.9	8.41e-4	245	207	5.4	1.19	
555291.1*	−1.9	−2.9	$7_{1,6}-7_{2,5}$ A	390.1	8.48e-4	210	193	6.2	1.21	blend $H_2C^{18}O$
555417.7	−0.3		$8_{3,5}-8_{1,7}$ E	131.3	1.71e-6	49				v blend CH_3OH & U-line
555418.5	0.5		$10_{3,7}-10_{1,9}$ E	175.4	2.66e-6	49				v blend CH_3OH & U-line
555681.0*	−2.0		$8_{1,7}-8_{2,6}$ A	408.7	8.52e-4					v blend SO_2, $H_2C^{18}O$, & CH_3OCH_3
556115.8*	−1.2		$9_{1,8}-9_{2,7}$ A	429.5	8.53e-4	202			1.15	
		0.8					119	2.9		2G; CR
		4.2					121	6.2		2G; HC
556594.4*	−0.6		$10_{1,9}-10_{2,8}$ A	452.7	8.52e-4	223			1.41	blend CH_3OH

Table 20. continued.

ν_{ul} [MHz]	$\Delta\nu_p$ [MHz]	$\Delta\nu_g$ [MHz]	Transition J_{K_a,K_c}	E_u [K]	A_{ul} [s^{-1}]	T_A^*(peak) [mK]	Ampl. [mK]	Width [km s^{-1}]	$\int T_A^* d\upsilon$ [K km s^{-1}]	Note
556603.7	−1.3		$25_{1,25}-24_{2,22}$ A	760.8	2.66e-4					v blend CH_3OH
557115.2*	−0.8	−3.8	$11_{1,10}-11_{2,9}$ A	478.2	8.50e-4	257	250	9.1	2.27	
557147.0*	−4.0		$11_{9,3}-10_{8,2}$ A	836.5	1.40e-3	86	74	7.2	0.26	blend CH_3OH
557147.0*	−4.0		$11_{9,2}-10_{8,3}$ A	836.5	1.40e-3	86	74	7.2	0.26	blend CH_3OH
557676.6*	−0.4		$12_{1,11}-12_{2,10}$ A	506.0	8.46e-4	189			1.01	
		0.6					107	3.5		2G; CR
		−3.4					88	6.9		2G; HC
558004.6*		−2.4	$4_{3,2}-3_{2,2}$ E	440.6	1.95e-4		55	6.4		v blend SO; from 3G SO
558276.8*	−0.2	−1.2	$13_{1,12}-13_{2,11}$ A	536.1	8.42e-4	137	134	5.2	0.71	
558344.5	0.5		$11_{2,9}-10_{1,9}$ E	175.5	5.16e-4	801			4.09	blend SO_2
		0.5					533	3.1		from 3G SO_2
		−2.5					244	10.5		from 3G SO_2
558606.4	0.4		$26_{2,25}-26_{1,26}$ E	843.0	7.47e-4	49				(too) weak
558890.2*	−2.8		$8_{6,2}-9_{5,5}$ A	551.5	8.90e-5	42			0.04	
558890.2*	−2.8		$8_{6,3}-9_{5,4}$ A	551.5	8.90e-5	42			0.04	
558904.6*	−0.4		$16_{5,11}-17_{4,14}$ E	744.1	1.27e-4	64			0.18	
558914.0*	−3.0		$14_{1,13}-14_{2,12}$ A	568.5	8.37e-4	105			0.46	
559586.1*	−2.9	−3.9	$15_{1,14}-15_{2,13}$ A	603.2	8.31e-4	128	116	5.3	0.61	
560291.0*	−9.0	−1.0	$16_{1,15}-16_{2,14}$ A	640.2	8.24e-4		177	9.0		v blend SO_2; from 2G SO_2
561026.4*	0.4		$17_{1,16}-17_{2,15}$ A	679.5	8.17e-4	103	90	4.8	0.46	
561269.1			$19_{2,18}-19_{1,19}$ A	478.2	7.75e-4					blend SO_2
561402.9			$18_{7,12}-19_{6,4}$ E	646.3	2.25e-4					blend SO_2
561789.7*	0.7	−2.3	$18_{1,17}-18_{2,16}$ A	721.2	8.09e-4	64	59	5.9	0.33	
564221.6			$21_{1,20}-21_{2,19}$ A	606.0	7.81e-4					v blend SiO
564759.8	−1.2	−2.2	$17_{2,16}-16_{3,13}$ A	392.5	3.52e-4	170	164	5.6	0.93	
567942.6	−3.4	−2.4	$20_{1,19}-19_{2,18}$ A	505.4	5.28e-4	163	163	6.1	1.02	
568566.1	−0.9		$3_{2,2}-2_{1,2}$ E	39.8	1.00e-3	965			5.32	
		0.1					761	3.9		2G; CR
		−2.9					233	9.0		2G; HC
568783.6	−0.4		$17_{0,17}-16_{1,16}$ A	354.5	1.10e-3	367			1.91	
		0.6					107	2.2		2G; CR
		−0.4					255	6.5		2G; HC
569324.5	−4.5	−3.5	$20_{2,19}-20_{1,20}$ A	524.4	7.95e-4	124	125	6.1	0.78	
570261.5	−1.5		$12_{5,8}-13_{4,9}$ A	318.9	2.31e-4	310			0.95	blend CH_3OH
		−2.5					123	2.8		2G; CR
		−3.5					199	7.2		2G; HC
570264.0	1.0	−3.5	$12_{5,7}-13_{4,10}$ A	318.9	2.31e-4	310	289	5.9	0.95	blend CH_3OH
570619.0	−1.0		$8_{4,4}-9_{3,6}$ E	179.5	2.02e-4	327			1.86	blend $^{13}CH_3OH$
		−1.0					216	2.4		2G; CR
		−4.0					143	8.5		2G; HC
572676.2	−1.8	−1.8	$14_{1,13}-13_{2,12}$ E	264.8	1.70e-5	95	76	3.3	0.26	weak
572898.8	−1.2		$15_{1,15}-14_{0,14}$ E	283.61	8.61e-4	493			2.99	
		0.8					242	3.6		2G; CR
		−1.2					236	8.6		2G; HC
573471.1	−1.9		$3_{3,1}-4_{2,3}$ E	76.6	7.30e-5	297	282	4.1	1.31	
573912.7	−2.3		$17_{2,15}-16_{3,14}$ A	392.9	3.84e-4	197			1.08	
		−2.3					86	2.5		2G; CR
		−4.3					125	6.7		2G; HC
574868.5	−2.5		$12_{1,12}-11_{1,11}$ A	193.9	8.53e-4	575			2.97	
		−2.5					325	3.1		2G; CR
		−3.5					260	7.0		2G; HC
575547.2*	−3.8	−3.8	$8_{0,8}-7_{1,7}$ E	383.9	4.15e-4	132	120	3.7	0.47	
Total No.	82									

Table 21. $^{13}CH_3OH$ parameters[a].

ν_{ul} [MHz]	$\Delta\nu_p$ [MHz]	$\Delta\nu_g$ [MHz]	Transition $J_{Ka,Kc}$	E_u [K]	A_{ul} [s^{-1}]	T_A^*(peak) [mK]	Ampl. [mK]	Width [km s^{-1}]	$\int T_A^* d\upsilon$ [K km s^{-1}]	Note
488153.5	−1.5	−0.5	$4_{1,4}-3_{0,3}$ A	37.0	7.46e-4	204	205	4.9	1.04	
488302.6	0.6	−0.4	$4_{2,3}-4_{2,3}$ A	60.5	5.50e-4	154	151	2.3	0.34	
490299.4	0.4		$5_{2,4}-5_{1,5}$ A	71.8	5.75e-4	168			0.59	
491170.0	0.0	1.0	$5_{3,3}-4_{2,2}$ A	84.0	6.52e-4	155	155	4.4	0.73	
491201.3	0.3	0.3	$5_{3,2}-4_{2,3}$ A	84.0	6.53e-4	156	145	4.2	0.64	
491310.1			$11_{1,10}-10_{2,8}$	170.6	2.15e-4	73			0.34	weak
544140.5*			$17_{1,17}-17_{2,16}$ A	670.5	7.71e-4	63			0.12	
544206.7	−1.3	−0.3	$8_{1,7}-7_{0,7}$	102.6	4.41e-4	93	76	4.9	0.37	
547457.8	−1.2	−2.2	$11_{2,9}-10_{1,9}$	171.9	4.90e-4	90	82	3.9	0.32	
549297.1*			$10_{1,10}-10_{2,9}$ A	449.5	8.29e-4					blend SO_2 & CH_3OH
552835.1*			$6_{1,5}-6_{2,4}$ A	372.9	8.32e-4	48			0.10	weak
555700.1			$15_{1,15}-14_{0,14}$ E	277.0	7.72e-4					blend SO_2 & CH_3OH
561138.5	−0.5		$12_{1,12}-11_{1,11}$ A	189.7	7.93e-4					v blend SO_2
564223.7	−4.3		$12_{0,12}-11_{0,11}$	189.4	8.10e-4					v blend SiO
565245.2	−1.8	−0.8	$12_{1,12}-11_{1,11}$ E	182.1	8.10e-4	89	72	4.2	0.30	
565527.8	−0.2	−1.2	$12_{0,12}-11_{0,11}$ A	176.6	8.17e-4	133	135	3.5	0.51	
565737.4	1.4	1.4	$12_{8,4}-11_{8,3}$ A	499.3	4.53e-4	68	65	2.0	0.07	too weak?
565737.4	1.4	1.4	$12_{8,5}-11_{8,4}$ A	499.3	4.53e-4	68	65	2.0	0.07	too weak?
565895.0			$12_{2,11}-11_{2,10}$ A	214.4	8.01e-4	85			0.34	?
565914.4	4.4	3.4	$12_{6,7}-11_{6,6}$	356.4	6.11e-4	108	103	3.2	0.32	
565946.2	−1.8	0.2	$12_{6,6}-11_{6,5}$ A	371.3	6.13e-4	68	51	4.7	0.23	
566411.9	−0.1		$12_{3,9}-11_{3,8}$	224.7	7.70e-4	110			0.48	blend U-line?
566662.8	−0.2	−1.2	$3_{2,2}-2_{1,2}$ E	39.6	9.96e-4	115	108	3.2	0.35	
566840.7	1.7		$12_{2,10}-11_{2,9}$	199.1	7.92e-4	69			0.30	
570624.2	−2.8		$12_{1,11}-11_{1,10}$ A	192.7	8.35e-4	140				v blend CH_3OH
Total No.	25									

[a] Notation as in Table 9. * Vibrationally excited transition, $v_t = 1$.

Table 22. $(CH_3)_2O$ parameters[a].

ν_{ul} [MHz]	$\Delta\nu_p$ [MHz]	$\Delta\nu_g$ [MHz]	Transition $J_{Ka,Kc}$	E_u [K]	A_{ul} [s^{-1}]	T_A^*(peak) [mK]	Ampl. [mK]	Width [km s^{-1}]	$\int T_A^* d\upsilon$ [K km s^{-1}]	Note
490795.3	−4.7		$15_{4,11}-14_{3,12}$ AE	131.9	3.56e-4	194			2.05	blend 3 groups
490795.3			$15_{4,11}-14_{3,12}$ EA	131.9	3.56e-4					
490797.5			$12_{5,8}-11_{4,7}$ EA	106.2	2.26e-4					
490798.3			$15_{4,11}-14_{3,12}$ EE	131.9	3.56e-4					
490801.3			$15_{4,11}-14_{3,12}$ AA	131.9	3.56e-4					
490804.3			$12_{5,8}-11_{4,7}$ AE	106.2	4.84e-4					
490804.7			$12_{5,8}-11_{4,7}$ EE	106.2	3.01e-4					
490810.3			$12_{5,8}-11_{4,7}$ AA	106.2	4.84e-4					
490811.4			$12_{5,7}-11_{4,7}$ EA	106.2	2.58e-4					
490812.1			$12_{5,7}-11_{4,7}$ EE	106.2	1.82e-4					
490864.4			$12_{5,8}-11_{4,8}$ EA	106.2	2.58e-4					
490869.8			$12_{5,8}-11_{4,8}$ EE	106.2	1.82e-4				0.88	blend 2 groups
490871.5			$12_{5,7}-11_{4,8}$ AE	106.2	4.84e-4					
490877.2			$12_{5,7}-11_{4,8}$ EE	106.2	3.01e-4					
490877.6			$12_{5,7}-11_{4,8}$ AA	106.2	4.84e-4					
490878.3			$12_{5,7}-11_{4,8}$ EA	106.2	2.26e-4					
542257.7	−1.3	−3.3	$19_{4,16}-18_{3,15}$ AE	195.8	4.30e-4	112	111	4.8	0.48	entire group
542257.7	−1.3	−3.3	$19_{4,16}-18_{3,15}$ EA							
542260.1	1.1	−0.9	$19_{4,16}-18_{3,15}$ EE							
542262.4	3.4	1.4	$19_{4,16}-18_{3,15}$ AA							

[a] Notation as in Table 9.

Table 22. continued.

ν_{ul} [MHz]	$\Delta\nu_p$ [MHz]	$\Delta\nu_g$ [MHz]	Transition J_{K_a,K_c}	E_u [K]	A_{ul} [s^{-1}]	T_A^*(peak) [mK]	Ampl. [mK]	Width [km s^{-1}]	$\int T_A^* d\upsilon$ [K km s^{-1}]	Note
543753.9	−5.1		$18_{3,15}-17_{2,16}$ AE	169.8	1.94e-4	45			0.20	entire group
543753.9	−5.1		$18_{3,15}-17_{2,16}$ EA							
543756.9	−2.1		$18_{3,15}-17_{2,16}$ EE							
543759.8	0.8		$18_{3,15}-17_{2,16}$ AA							
546827.8	−4.2	−3.2	$15_{5,11}-14_{4,10}$ EA	144.4	5.50e-4	116	119	3.5	0.60	entire group
546829.2	−2.8	−1.8	$15_{5,11}-14_{4,10}$ AE							
546831.5	−0.5	0.5	$15_{5,11}-14_{4,10}$ EE							
546834.5	2.5	3.5	$15_{5,11}-14_{4,10}$ AA							
547284.8	−2.2	−3.2	$15_{5,10}-14_{4,11}$ AE	144.4	5.90e-4	187	170	3.1	0.56	entire group
547286.2	−0.8	−1.8	$15_{5,10}-14_{4,11}$ EA		5.59e-4					
547287.8	0.8	−0.2	$15_{5,10}-14_{4,11}$ EE		5.82e-4					
547290.1	3.1	2.1	$15_{5,10}-14_{4,11}$ AA		5.90e-4					
549504.7	−3.3		$30_{1,29}-29_{2,28}$ EA	420.3	1.16e-4	82			0.39	entire group
549504.7	−3.3		$30_{1,29}-29_{2,28}$ AE							
549504.9	−3.1		$30_{1,29}-29_{2,28}$ EE							
549505.2	−2.8		$30_{1,29}-29_{2,28}$ AA							
549543.8			$12_{66}-11_{56}$ EA	121.6	7.76e-4					2 groups bl SO_2
549546.5			$12_{67}-11_{56}$ AE							
549547.4			$12_{66}-11_{56}$ EE							
549547.7			$12_{66}-11_{57}$ AE							
549550.4			$12_{67}-11_{57}$ EA							
549550.6			$12_{67}-11_{56}$ AA							
549550.8			$12_{67}-11_{57}$ EE							
549551.7	0.7		$12_{66}-11_{57}$ AA							
551270.8	−6.2	−6.2	$9_{7,3}-8_{6,2}$ EA	109.8	1.09e-4	383	312	4.3		blend CH_3CN; 2G CH_3CN
551273.6	−3.4	−3.4	$9_{7,3}-8_{6,2}$ EE							
551275.1	−1.9	−1.9	$9_{7,2}-8_{6,3}$ AE							
551275.1	−1.9	−1.9	$9_{7,3}-8_{6,2}$ AE							
551276.5	−0.5	−0.5	$9_{7,3}-8_{6,2}$ AA							
551276.5	−0.5	−0.5	$9_{7,2}-8_{6,3}$ AA							
551277.9	0.9	0.9	$9_{7,2}-8_{6,3}$ EE							
551279.4	2.4	2.4	$9_{7,2}-8_{6,3}$ EA							
552258.9	−3.1		$18_{4,14}-17_{3,15}$ EA	178.6	4.35e-4	112			0.67	entire group
552258.9	−3.1		$18_{4,14}-17_{3,15}$ AE							
552261.4	−0.6		$18_{4,14}-17_{3,15}$ EE							
552264.0	2.0		$18_{4,14}-17_{3,15}$ AA							
554619.8	−5.2		$25_{10,15}-25_{9,16}$ AA	436.3	7.47e-4	64			0.13	entire group
554619.8	−5.2		$25_{10,16}-25_{9,17}$ AA							
554621.0	-4.0		$25_{10,16}-25_{9,17}$ EE							
554621.5	−3.5		$25_{10,15}-25_{9,16}$ EE							
554622.1	−2.9		$25_{10,16}-25_{9,17}$ EA							
554622.6	−2.4		$25_{10,15}-25_{9,16}$ AE							
554622.6	−2.4		$25_{10,16}-25_{9,17}$ AE							
554623.2	−1.7		$25_{10,15}-25_{9,16}$ EA							
554811.5	−2.5		$24_{10,14}-24_{9,15}$ AA	413.5	7.36e-4	60		2.2	0.12	entire group
554811.5	−2.5		$24_{10,15}-24_{9,16}$ AA							
554812.7	−1.3		$24_{10,15}-24_{9,16}$ EE							
554813.4	−0.6		$24_{10,14}-24_{9,15}$ EE							
554813.9	−0.1		$24_{10,15}-24_{9,16}$ EA							
554814.6	0.6		$24_{10,14}-24_{9,15}$ AE							
554814.6	0.6		$24_{10,15}-24_{9,16}$ AE							
554815.3	1.3		$24_{10,14}-24_{9,15}$ EA							
554888.3	−2.7		$20_{4,17}-19_{3,16}$ EA	214.1	4.50e-4	118			0.32	entire group
554888.3	−2.7		$20_{4,17}-19_{3,16}$ AE							
554890.4	−0.6		$20_{4,17}-19_{3,16}$ EE							
554892.5	1.5		$20_{4,17}-19_{3,16}$ AA							

Table 22. continued.

ν_{ul} [MHz]	$\Delta\nu_p$ [MHz]	$\Delta\nu_g$ [MHz]	Transition $J_{Ka,Kc}$	E_u [K]	A_{ul} [s^{-1}]	T_A^*(peak) [mK]	Ampl. [mK]	Width [km s^{-1}]	$\int T_A^* d\upsilon$ [K km s^{-1}]	Note
554979.1	−4.9		$23_{10,13}-23_{9,14}$ AA	391.7	7.23e-4	90			0.21	entire group
554979.1	−4.9		$23_{10,14}-23_{9,15}$ AA							
554980.4	−3.6		$23_{10,14}-23_{9,15}$ EE							
554981.2	−2.8		$23_{10,13}-23_{9,14}$ EE							
554981.7	−2.3		$23_{10,14}-23_{9,15}$ EA							
554982.5	−1.5		$23_{10,13}-23_{9,14}$ AE							
554982.5	−1.5		$23_{10,14}-23_{9,15}$ AE							
554983.3	−0.7		$23_{10,13}-23_{9,14}$ EA							
555124.5			$22_{10,12}-22_{9,13}$ AA	370.7	7.08e-4					entire group
555124.5			$22_{10,13}-22_{9,14}$ AA							bl SO_2
555125.9			$22_{10,13}-22_{9,14}$ EE							
555126.8			$22_{10,12}-22_{9,13}$ EE							
555127.3			$22_{10,13}-22_{9,14}$ EA							
555128.2			$22_{10,12}-22_{9,13}$ AE							
555128.2			$22_{10,13}-22_{9,14}$ AE							
555129.1			$22_{10,12}-22_{9,13}$ EA							
555249.8	−11.2	−9.2	$21_{10,11}-21_{9,12}$ AA	350.7	6.92e-4	129	104	8.2	0.82	entire group
555249.8	−11.2	−9.2	$21_{10,12}-21_{9,13}$ AA							
555251.3	−9.7	−7.7	$21_{10,12}-21_{9,13}$ EE							
555252.3	−8.7	−6.7	$21_{10,11}-21_{9,12}$ EE							
555252.7	−8.3	−6.3	$21_{10,12}-21_{9,13}$ EA							
555253.8	−7.2	−5.2	$21_{10,12}-21_{9,13}$ AE							
555253.8	−7.2	−5.2	$21_{10,11}-21_{9,12}$ AE							
555254.9	−6.1	−4.1	$21_{10,11}-21_{9,12}$ EA							
555356.8	−6.2	−6.2	$20_{10,10}-20_{9,11}$ AA	331.6	6.73e-4	75	71	4.9	0.37	entire group
555356.8	−6.2	−6.2	$20_{10,11}-20_{9,12}$ AA							
555358.3	−4.7	−4.7	$20_{10,11}-20_{9,12}$ EE							
555359.5	−3.5	−3.5	$20_{10,10}-20_{9,11}$ EE							
555359.9	−3.1	−3.1	$20_{10,11}-20_{9,12}$ EA							
555361.1	−1.9	−1.9	$20_{10,10}-20_{9,11}$ AE							
555361.1	−1.9	−1.9	$20_{10,11}-20_{9,12}$ AE							
555362.3	−0.7	−0.7	$20_{10,10}-20_{9,11}$ EA							
555447.3	−3.7	−5.7	$19_{10,9}-19_{9,10}$ AA	313.4	6.52e-4	104		5.1	0.39	entire group
555447.3	−3.7	−5.7	$19_{10,10}-19_{9,11}$ AA							
555448.9	−2.1	−4.1	$19_{10,10}-19_{9,11}$ EE							
555450.2	−0.8	−2.8	$19_{10,9}-19_{9,10}$ EE							
555450.6	−0.4	−2.4	$19_{10,10}-19_{9,11}$ EA							
555451.9	0.9	−1.1	$19_{10,9}-19_{9,10}$ AE							
555451.9	0.9	−1.1	$19_{10,10}-19_{9,11}$ AE							
555453.1	2.1	0.1	$19_{10,9}-19_{9,10}$ EA							
555522.9	−4.1	−6.1	$18_{10,8}-18_{9,9}$ AA	296.1	6.28e-4	110			0.51	entire group
555522.9	−4.1	−6.1	$18_{10,9}-18_{9,10}$ AA							
555524.6	−2.6	−4.6	$18_{10,9}-18_{9,10}$ EE							
555526.0	−1.0	−3.0	$18_{10,8}-18_{9,9}$ EE							
555526.4	−0.6	−2.6	$18_{10,9}-18_{9,10}$ EA							
555527.8	0.8	1.2	$18_{10,8}-18_{9,9}$ AE							
555527.8	0.8	1.2	$18_{10,9}-18_{9,10}$ AE							
555529.2	2.2	0.2	$18_{10,8}-18_{9,9}$ EA							
555585.3	−5.7	−5.7	$17_{10,7}-17_{9,8}$ AA	279.7	5.99e-4	83		4.2	0.35	entire group
555585.3	−5.7	−5.7	$17_{10,8}-17_{9,9}$ AA							
555587.1	−3.9	−3.9	$17_{10,8}-7_{9,9}$ EE							
555588.6	−2.4	−2.4	$17_{10,7}-17_{9,8}$ EE							
555589.0	−2.0	−2.0	$17_{10,8}-17_{9,9}$ EA							
555590.4	−0.6	−0.6	$17_{10,7}-17_{9,8}$ AE							
555590.4	−0.6	−0.6	$17_{10,8}-17_{9,9}$ AE							
555591.9	0.9	0.9	$17_{10,7}-17_{9,8}$ EA							

Table 22. continued.

ν_{ul} [MHz]	$\Delta\nu_p$ [MHz]	$\Delta\nu_g$ [MHz]	Transition J_{K_a,K_c}	E_u [K]	A_{ul} [s^{-1}]	T_A^*(peak) [mK]	Ampl. [mK]	Width [km s^{-1}]	$\int T_A^* d\upsilon$ [K km s^{-1}]	Note
555635.9			$16_{10,6}-16_{9,7}$ AA	264.2	5.66e-4					blend SO_2
555635.9			$16_{10,7}-16_{9,8}$ AA							
555637.9			$16_{10,7}-16_{9,8}$ EE							
555639.4			$16_{10,6}-16_{9,7}$ EE							
555639.8			$16_{10,7}-16_{9,8}$ EA							
555641.4			$16_{10,6}-16_{9,7}$ AE							
555641.4			$16_{10,7}-16_{9,8}$ AE							
555642.9			$16_{10,6}-16_{9,7}$ EA							
555676.3			$15_{10,5}-15_{9,6}$ AA	249.7	5.27e-4					blend SO_2, CH_3OH
555676.3			$15_{10,6}-15_{9,7}$ AA							
555678.3			$15_{10,6}-15_{9,7}$ EE							
555679.9			$15_{10,5}-15_{9,6}$ EE							
555680.3			$15_{10,6}-15_{9,7}$ EA							
555681.9			$15_{10,5}-15_{9,6}$ AE							
555681.9			$15_{10,6}-15_{9,7}$ AE							
555683.6			$15_{10,5}-15_{9,6}$ EA							
555707.6			$14_{10,4}-14_{9,5}$ AA	236.0	4.80e-4					blend SO_2
555707.6			$14_{10,5}-14_{9,6}$ AA							
555709.7			$14_{10,5}-14_{9,6}$ EE							
555711.4			$14_{10,4}-14_{9,5}$ EE							
555711.8			$14_{10,5}-14_{9,6}$ EA							
555713.5			$14_{10,4}-14_{9,5}$ AE							
555713.5			$14_{10,5}-14_{9,6}$ AE							
555715.2			$14_{10,4}-14_{9,5}$ EA							
555731.2	−4.8	−6.8	$13_{10,3}-13_{9,4}$ AA	223.3	4.23e-4	96		6.2	0.61	entire group
555731.2	−4.8	−6.8	$13_{10,4}-13_{9,5}$ AA							
555733.4	−2.6	−4.6	$13_{10,4}-13_{9,5}$ EE							
555735.2	−0.8	−2.8	$13_{10,3}-13_{9,4}$ EE							
555735.5	−0.5	−2.5	$13_{10,4}-13_{9,5}$ EA							
555737.3	1.3	−0.7	$13_{10,3}-13_{9,4}$ AE							
555737.3	1.3	−0.7	$13_{10,4}-13_{9,5}$ AE							
555739.1	3.1	1.1	$13_{10,3}-13_{9,4}$ EA							
555748.2			$12_{10,2}-12_{9,3}$ AA	211.5	3.53e-4					blend 3 groups
555748.2			$12_{10,3}-12_{9,4}$ AA							
555750.5			$12_{10,3}-12_{9,4}$ EE							
555752.3			$12_{10,2}-12_{9,3}$ EE							
555752.7			$12_{10,3}-12_{9,4}$ EA							
555754.6			$12_{10,2}-12_{9,3}$ AE							
555754.6			$12_{10,3}-12_{9,4}$ AE							
555756.4			$12_{10,2}-12_{9,3}$ EA							
555759.7			$11_{10,1}-11_{9,2}$ AA	200.6	2.64e-4					blend 3 groups
555759.7			$11_{10,2}-11_{9,3}$ AA							
555762.1			$11_{10,2}-11_{9,3}$ EE							
555764.0			$11_{10,1}-11_{9,2}$ EE							
555764.4			$11_{10,2}-11_{9,3}$ EA							
555766.3			$11_{10,1}-11_{9,2}$ AE							
555766.3			$11_{10,2}-11_{9,3}$ AE							
555766.8			$10_{10,0}-10_{9,1}$ AA	190.5	1.50e-4					blend 3 groups
555766.8			$10_{10,1}-10_{9,2}$ AA							
555768.2			$11_{10,1}-11_{9,2}$ EA	200.6	2.64e-4					
555769.2			$10_{10,1}-10_{9,2}$ EE	190.5	1.50 e-4					blend 3 groups
555771.2			$10_{10,0}-10_{9,1}$ EE							
555771.6			$10_{10,1}-10_{9,2}$ EA							
555773.5			$10_{10,0}-10_{9,1}$ AE							
555773.5			$10_{10,1}-10_{9,2}$ AE							
555775.5			$10_{10,0}-10_{9,1}$ EA							

Table 22. continued.

ν_{ul} [MHz]	$\Delta\nu_p$ [MHz]	$\Delta\nu_g$ [MHz]	Transition J_{K_a,K_c}	E_u [K]	A_{ul} [s^{-1}]	T_A^*(peak) [mK]	Ampl. [mK]	Width [km s^{-1}]	$\int T_A^* d\upsilon$ [K km s^{-1}]	Note
556179.4	−1.6	−0.6	$31_{0,31}-30_{1,30}$ EA	431.3	1.50e-4	65	60	3.5	0.17	entire group
556179.4	−1.6	−0.6	$31_{0,31}-30_{1,30}$ AE							
556179.4	−1.6	−0.6	$31_{0,31}-30_{1,30}$ EE							
556179.5	−1.5	−0.5	$31_{0,31}-30_{1,30}$ AA							
556212.0			$31_{1,31}-30_{0,30}$ EA							(Too) weak
556212.0			$31_{1,31}-30_{0,30}$ AE							(Too) weak
556212.1			$31_{1,31}-30_{0,30}$ EE							(Too) weak
556212.2			$31_{1,31}-30_{0,30}$ AA							(Too) weak
560648.9			$29_{3,27}-28_{2,26}$ AA	407.3	8.54e-4					v blend SO_2
560648.9			$29_{3,27}-28_{2,26}$ EE							
560649.0			$29_{3,27}-28_{2,26}$ EA							
560649.0			$29_{3,27}-28_{2,26}$ AE							
565262.1	−3.9	−3.9	$16_{5,12}-15_{4,11}$ EA	159.0	6.18e-4	154	120	5.7	0.69	entire group
565262.8	−3.2		$16_{5,12}-15_{4,11}$ AE							
565265.2	−0.8		$16_{5,12}-15_{4,11}$ EE							
565267.9	1.9		$16_{5,12}-15_{4,11}$ AA							
566046.6	−3.4	−4.4	$16_{5,11}-15_{4,12}$ AE	159.0	6.29e-4	204	198	3.4	0.71	entire group
566047.3	−2.7	−3.7	$16_{5,11}-15_{4,12}$ EA							
566049.3	−0.7	−1.7	$16_{5,11}-15_{4,12}$ EE							
566051.7	1.7	0.7	$16_{5,11}-15_{4,12}$ AA							
566606.7	−2.3	−2.3	$21_{4,18}-20_{3,17}$ AE	233.3	4.71e-4	90	73	3.9	0.28	entire group
566606.7	−2.3	−2.3	$21_{4,18}-20_{3,17}$ EA							
566608.5	−0.5	−0.5	$21_{4,18}-20_{3,17}$ EE							
566610.4	1.4	1.4	$21_{4,18}-20_{3,17}$ AA							
568430.6	−7.4		$13_{6,7}-12_{5,7}$ EA	133.4	8.10e-4	331	330	5.1	1.79	entire group
568432.6	−5.4		$13_{6,8}-12_{5,7}$ AE							
568433.9	−4.1		$13_{6,7}-12_{5,7}$ EE		7.85e-4					
568435.3	−2.7		$13_{6,7}-12_{5,8}$ AE		8.19e-4					
568436.3	−1.7		$13_{6,8}-12_{5,7}$ AA							
568437.2	−0.8		$13_{6,8}-12_{5,8}$ EA		8.10e-4					
568437.7	−0.3		$13_{6,8}-12_{5,8}$ EE		7.85e-4					
568439.2	1.2		$13_{6,7}-12_{5,8}$ AA		8.19e-4					
568690.1	−2.9		$31_{2,30}-30_{1,29}$ AE	447.6	1.30e-4	92			0.29	entire group
568690.1			$31_{2,30}-30_{1,29}$ EA							
568690.3	−2.7		$31_{2,30}-30_{1,29}$ EE							
568690.4	−2.6		$31_{2,30}-30_{1,29}$ AA							
570219.1	−5.9		$10_{7,4}-9_{6,3}$ EA	118.9	1.12e-4	351	342	4.3	1.55	entire group
570221.9	−2.9		$10_{7,4}-9_{6,3}$ EE							
570223.3	−1.7		$10_{7,3}-9_{6,4}$ AE							
570223.3	−1.7		$10_{7,4}-9_{6,3}$ AE							
570224.7	−0.3		$10_{7,4}-9_{6,3}$ AA							
570224.7	−0.3		$10_{7,3}-9_{6,4}$ AA							
570226.1	1.1		$10_{7,3}-9_{6,4}$ EE							
570227.5	2.5		$10_{7,3}-9_{6,4}$ EA							
574090.9	−7.1	−6.1	$19_{4,15}-18_{3,16}$ EA	196.0	4.59e-4	92	89	2.8	0.29	entire group
574090.9	−7.1	−6.1	$19_{4,15}-18_{3,16}$ AE							
574093.3	−4.7	−3.7	$19_{4,15}-18_{3,16}$ EE							
574095.7	−2.3	−1.3	$19_{4,15}-18_{3,16}$ AA							
Total No.	236									

Table 23. H_2CO and isotopologue parameters[a].

Species	ν_{ul} [MHz]	Δv_p [MHz]	Δv_g [MHz]	Transition $J_{Ka,Kc}$	E_u [K]	A_{ul} [s^{-1}]	T_A^*(peak) [mK]	Ampl. [mK]	Width [km s^{-1}]	$\int T_A^* dv$ [K km s^{-1}]	Note
H_2CO	491968.4	2.4	1.4	$7_{1,7}-6_{1,6}$	106.3	3.44e-3	2040	1954	5.2	11.30	
	561899.3	1.3		$8_{1,8}-7_{1,7}$	133.3	5.20e-3	1705			16.3	
			1.3					1167	4.9		2G; CR
			−0.7					504	19.0		2G; LVF
	576708.3	−0.7		$8_{0,8}-7_{0,7}$	125.1	5.70e-3	1116			11.30	blend NS
			0.3					742	4.8		2G; CR
			−6.7					392	18.7		2G; LVF
$H_2^{13}CO$	548475.2	0.2	0.2	$8_{1,8}-7_{1,7}$	130.4	4.84e-3	155	135	4.3	0.62	
HDCO	491937.0	2.0	3.0	$8_{1,8}-7_{1,7}$	114.4	3.48e-3	370	360	6.1	2.41	blend U-line?
	552740.9	−0.1	0.9	$9_{1,9}-8_{1,8}$	141.0	4.99e-3	101	88	3.0	0.27	
	565857.5	2.5		$9_{0,9}-8_{0,8}$	137.3	5.40e-3	60			0.19	weak
Total No.	7										

[a] Notation as in Table 9.

Table 24. H_2CS parameters[a].

ν_{ul} [MHz]	Δv_p [MHz]	Δv_g [MHz]	Transition $J_{Ka,Kc}$	E_u [K]	A_{ul} [s^{-1}]	T_A^*(peak) [mK]	Ampl. [mK]	Width [km s^{-1}]	$\int T_A^* dv$ [K km s^{-1}]	Note
487663.4	0.4	0.4	$14_{1,13}-13_{1,12}$	188.8	1.76e-3	172	161	3.7	0.62	
547308.2	−3.8	−2.8	$16_{0,16}-15_{0,15}$	223.7	2.51e-3	77	63	3	0.19	
549402.4	0.4	0.4	$16_{3,14}-15_{3,13}$	342.6	2.45e-3	62	55	1.8	0.15	
549447.5	−1.5		$16_{3,13}-15_{3,12}$	342.6	2.45e-3	98				blend U-line
557123.2	2.2		$16_{1,15}-15_{1,14}$	240.6	2.64e-3					blend CH_3OH; in H_2O wing
574140.0	−2.0	−2.0	$17_{1,17}-16_{1,16}$	261.4	2.90e-3	130	125	2.9	0.38	
Total No.	6									

[a] Notation as in Table 9.

Table 25. CS and ^{13}CS parameters[a].

Species	ν_{ul} [MHz]	Δv_p [MHz]	Δv_g [MHz]	Transition J	E_u [K]	A_{ul} [s^{-1}]	T_A^*(peak) [mK]	Ampl. [mK]	Width [km s^{-1}]	$\int T_A^* dv$ [K km s^{-1}]	Note
CS	489751.1	3.1		10−9	129.3	0.00250	2814			23.4	
			−0.9					424	9.0		HC, 3G fit
			2.1					1730	4.0		ER/CR, 3G fit
			1.1					633	18.0		LVF, 3G fit
^{13}CS	554726.0		−2.0	12−11	173.1	0.00366		88	4.8		v blend, 2G $^{34}SO_2$
Total No.	2										

[a] Notation as in Table 9.

Table 26. NO parameters[a].

ν_{ul} [MHz]	Δv_p [MHz]	Transition $J(F)$	E_u [K]	A_{ul} [s^{-1}]	T_A^*(peak) [mK]	Ampl. [mK]	Width [km s^{-1}]	$\int T_A^* dv$ [K km s^{-1}]	Note
551187.3	−0.7	$^2\Pi_{1/2}$ 5.5(5.5)−4.5(4.5) e	84.2	2.16e-5	540				entire group;
						265	5.4		5G from CH_3CN,
						284	18.6		NO & CH_3OH
551187.5		$^2\Pi_{1/2}$ 5.5(6.5)−4.5(5.5) e	84.1	2.23e-5					
551188.8		$^2\Pi_{1/2}$ 5.5(4.5)−4.5(3.5) e	84.2	2.14e-5					
551531.5	0.5	$^2\Pi_{1/2}$ 5.5(6.5)−4.5(5.5) f	84.3	2.24e-5	644			9.331	entire group;
									blend CH_3CN
551534.0	3.0	$^2\Pi_{1/2}$ 5.5(4.5)−4.5(3.5) f	84.2	2.15e-5					blend CH_3CN, NO
551534.1	3.1	$^2\Pi_{1/2}$ 5.5(5.5)−4.5(4.5) f	84.3	2.16e-5					blend CH_3CN, NO
567064.2	−11.8	$^2\Pi_{3/2}$ 5.5(6.5)−4.5(5.5) e	231.7	2.27e-5	122	97	19.1	1.805	entire group;
567069.6		$^2\Pi_{3/2}$ 5.5(5.5)−4.5(4.5) e	231.7	2.63e-5					blend H_2S
567073.4		$^2\Pi_{3/2}$ 5.5(4.5)−4.5(3.5) e	231.7	1.82e-5					blend H_2S
567077.9		$^2\Pi_{3/2}$ 5.5(6.5)−4.5(5.5) f	231.7	2.27e-5					blend H_2S
567082.7		$^2\Pi_{3/2}$ 5.5(5.5)−4.5(4.5) f	231.7	2.19e-5					blend H_2S
567086.6		$^2\Pi_{3/2}$ 5.5(4.5)−4.5(3.5) f	231.7	2.18e-5					blend H_2S
Total No.	12								

[a] Notation as in Table 9.

Table 27. HNC parameters[a].

ν_{ul} [MHz]	Δv_p [MHz]	Δv_g [MHz]	Transition J	E_u [K]	A_{ul} [s^{-1}]	T_A^*(peak) [mK]	Ampl. [mK]	Width [km s^{-1}]	$\int T_A^* dv$ [K km s^{-1}]	Note
543897.6	1.6		6−5	91.4	8.04e-3	913			10.70	v blend U-line
		1.6					600	3.8		ER; from 4G U-line
		−4.4					171	9.3		HC; from 4G U-line
		−1.4					224	26.8		Plateau; from 4G U-line
Total No.	1									

[a] Notation as in Table 9.

Table 28. CN parameters[a].

ν_{ul} [MHz]	Δv_p [MHz]	Δv_g [MHz]	Transition $N(J, F)$	E_u [K]	A_{ul} [s^{-1}]	T_A^*(peak) [mK]	Ampl. [mK]	Width [km s^{-1}]	$\int T_A^* dv$ [K km s^{-1}]	Note
566729.9	1.9	0.9	5(4.5, 5.5)–4(3.5, 4.5)	54.4	1.98e-3	690			3.345	entire group;
							570	3.5		2G; PDR/ER
							122	10.0		2G; HC
566730.7			5(4.5, 3.5)–4(3.5, 2.5)	54.4	1.86e-3					blend CN
566730.8			5(4.5, 4.5)–4(3.5, 3.5)	54.4	1.88e-3					blend CN
566946.8	1.8		5(5.5, 5.5)–4(4.5, 4.5)	54.4	1.96e-3	965			5.15	entire group;
										blend CN
		1.8	5(5.5, 5.5)–4(4.5, 4.5)	54.4	1.96e-3		736	3.8		3G CN; PDR/ER
		0.8	5(5.5, 5.5)–4(4.5, 4.5)	54.4	1.96e-3		214	10.8		v blends; HC
566946.9			5(5.5, 6.5)–4(4.5, 5.5)	54.4	2.03e-3					blend CN
566947.2			5(5.5, 4.5)–4(4.5, 3.5)	54.4	1.95e-3					blend CN
566962.0	1.0	0.0	5(5.5,4.5)–4(4.5,4.5)	54.4	8.00e-5		100	2		entire group;
										3G CN
566963.7			5(5.5,5.5)–4(4.5,5.5)	54.4	6.7e-5					
Total No.	8									

[a] Notation as in Table 9.

Table 29. N_2H^+ parameters[a].

ν_{ul} [MHz]	Δv_p [MHz]	Δv_g [MHz]	Transition J	E_u [K]	A_{ul} [s^{-1}]	T_A^*(peak) [mK]	Ampl. [mK]	Width [km s^{-1}]	$\int T_A^* dv$ [K km s^{-1}]	Note
558966.6	4.6	1.6	6−5	93.9	1.08e-2	315	300	4.8	1.46	
Total No.	1									

[a] Notation as in Table 9.

Table 30. HCS^+ parameters[a].

ν_{ul} [MHz]	$\Delta\nu_p$ [MHz]	$\Delta\nu_g$ [MHz]	Transition J	E_u [K]	A_{ul} [s^{-1}]	T_A^*(peak) [mK]	Ampl. [mK]	Width [km s^{-1}]	$\int T_A^* d\upsilon$ [K km s^{-1}]	Note
554576.6			13−12	186.3	3.66e-3		57	3.4		v blend ^{33}SO
										2G ^{33}SO
Total No.	1									

[a] Notation as in Table 9.

Table 31. NS parameters[a].

ν_{ul} [MHz]	$\Delta\nu_p$ [MHz]	$\Delta\nu_g$ [MHz]	Transition J	E_u [K]	A_{ul} [s^{-1}]	T_A^*(peak) [mK]	Ampl. [mK]	Width [km s^{-1}]	$\int T_A^* d\upsilon$ [K km s^{-1}]	Note
576720.2			$^2\Pi_{1/2}$ 12.5−11.5	187.36						v blend H_2CO
Total No.	1									

[a] Notation as in Table 9.

Table 32. CO and C parameters[a].

Species	ν_{ul} [MHz]	$\Delta\nu_p$ [MHz]	$\Delta\nu_g$ [MHz]	Transition J	E_u [K]	A_{ul} [s^{-1}]	T_A^*(peak) [mK]	Ampl. [mK]	Width [km s^{-1}]	$\int T_A^* d\upsilon$ [K km s^{-1}]	Note
CO	576267.9	−0.1		5−4	83.0	1.22e-5	62200			785.50	
^{13}CO	550926.3	0.3		5−4	79.3	1.10e-5	24300			174.30	
			0.3					21600	4.8		3G; N
			−0.7					2180	18.0		3G; LVF
			−0.7					470	48.7		3G;HVF
$C^{17}O$	561712.8	1.8	1.8	5−4	80.9	1.14e-5	1169			6.03	blend
											^{34}SO, SO_2
			1.8					1070	4.2		3G; N
			3.8					116	18.0		3G; LVF
$C^{18}O$	548831.0	2.0		5−4	79.0	1.06e-5	4219			24.30	
			1.0					3810	4.2		3G; N
			0.0					367	18.0		3G; LVF
C	492160.7			1−0	23.6	7.99e-8	7800	7794	4.5	38.7	
Total No.	5										

[a] Notation as in Table 9.

Table 33. Water parameters[a].

Species	ν_{ul} [MHz]	$\Delta\nu_p$ [MHz]	$\Delta\nu_g$ [MHz]	Transition J_{K_a,K_c}	E_u [K]	A_{ul} [s^{-1}]	T_A^*(peak) [mK]	Ampl. [mK]	Width [km s^{-1}]	$\int T_A^* d\upsilon$ [K km s^{-1}]	Note
$o-H_2O$	556936.0	−7.0		$1_{1,0}-1_{0,1}$	61.0	3.46e-3	7600			320.30	
$p-H_2O$	488491.1	−0.9	−5.9	$6_{2,4}-7_{1,7}$	867.3	1.22e-5	196	181	12.0	2.24	
$o-H_2^{17}O$	552021.0	2.0		$1_{1,0}-1_{0,1}$	60.7	3.37e-3	464			9.44	blend SO_2
											&CH_3OH
			4.0					76	5.0		3G; CR
			1.0					214	18.0		3G; LVF
			10.0					179	30.1		3G; HVF
$o-H_2^{18}O$	489054.3	−6.7	−7.7	$4_{2,3}-3_{3,0}$	429	8.84e-6	83	58	5.7	0.33	?
	547676.4	3.4		$1_{1,0}-1_{0,1}$	60.5	3.29e-3	715			15.90	blend $^{34}SO_2$
											& CH_3OH
			4.4					145	5.0		3G; CR
			4.4					275	18.0		3G; LVF
			11.4					298	33.4		3G; HVF
HDO	490596.7	−0.3		$2_{0,2}-1_{1,1}$	66.4	5.25e-4	841			10.70	
			0.7					459	4.6		3G; CR
			6.7					273	18.0		3G; LVF
			−11.3					216	13.4		3G; LVF
Total No.	6										

[a] Notation as in Table 9.

Table 34. U-line parameters[a].

ν_{ul} [MHz]	T_A^*(peak) [mK]	Ampl. [mK]	Width [km s^{-1}]	$\int T_A^* \, d\upsilon$ [K km s^{-1}]	Note
487 209	91			0.673	SO^+ ?
488 598	94	73	3.4	0.256	CH_3OCHO?
488 633	83	76	4.3	0.313	CH_3CHO?
491 496	104			1.438	CH_3OCHO?
491 892	157			0.64	tripple peaked
541 981	109	87	4.5	0.38	CH_3OCHO?
542 945	140	122	6.7	0.813	
543 873		72	3.9		v blend HNC; from 4G HNC
546 138	50			0.368	ND?
549 449					blend with H_2CS
552 308	64	50	13	0.663	
553 667		62	3.4		blend ^{33}SO, 3G fit with ^{33}SO, CH_3OCHO?
553 716		80	2.4		blend ^{33}SO, 3G fit with ^{33}SO
559 239					v blend SO; CH_3OCHO?
559 861					v blend SO_2, CH_3OCHO?
559 913					v blend SO_2
561 971	57			0.187	
562 960	106	107	5.4	0.593	
563 033	94	79	5.1	0.395	
564 105	111	75	6.2	0.495	
566 066	117	108	2.7	0.306	
567 485	143	133	2	0.278	
569 138	148	135	3.1	0.41	HNCO?
570 303	68	85	2.6	0.158	
572 596	90	84	2.4	0.202	
572 678	95	74	3.1	0.268	
574 184	80	81	2	0.155	
576 446					v blend CO wing
Total No.	28				

[a] Notation as in Table 9.

Table 35. T-line parameters[a].

ν_{ul} [MHz]	T_A^*(peak) [mK]	Ampl. [mK]	Width [km s^{-1}]	$\int T_A^* \, d\upsilon$ [K km s^{-1}]	Note
486 845	80	83	3.3	0.275	SO^+ ?
487 507	70	77	2.7	0.213	CH_3CHO?
488 477	49	47	3.2	0.147	
489 193	107	114	1.7	0.412	
489 709					SiS?; v blend CS
541 926	104	93	2.7	0.292	
544 016	51			0.396	SiS?
546 176	50			0.060	ND?
546 662	67			0.141	
546 805	79	68	2.3	0.213	
547 080					v blend ^{34}SO
547 162					v blend ^{34}SO
547 262	69			0.115	HNCO?
549 142	53			0.217	HNCO?
549 199	43			0.199	HNCO? or H_2CS?
549 719	68	62	3.6	0.278	CH_3OCHO? or SO_2?
550 132	64			0.375	SO_2?
552 846	62			0.131	
555 312	52	46	2.5	0.117	
555 914	63			0.194	
555 933	49			0.124	
556 267	40			0.193	
556 633	52	51	1.9	0.1	
559 816	45			0.060	weak, HDO?
560 753	43			0.212	
562 118	70	60	3.6	0.219	
563 481	96			0.278	weak, HNCO?
564 418	61	36	9.3	0.336	SH^-?
570 335	79	81	1.6	0.112	
570 790	76	69	2.1	0.141	
570 814	72	71	1.7	0.124	
571 151	49			0.138	HNCO?
571 217	59			0.168	HNCO?
571 477	58			0.118	$H_2C^{18}O$?
575 397	69	62	1.8	0.104	
577 160	144	93	6.0	0.503	
Total No.	36				

[a] Notation as in Table 9.